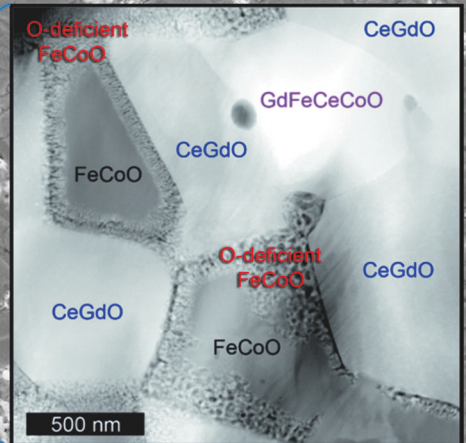
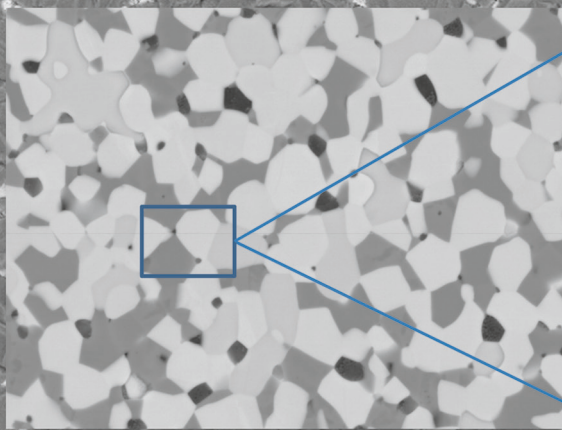


# Dual Phase Oxygen Transport Membrane for Efficient Oxyfuel Combustion

Madhumidha Ramasamy



Energie & Umwelt/  
Energy & Environment  
Band/ Volume 35 1  
ISBN 978-3-95806-196-5





Forschungszentrum Jülich GmbH  
Institute of Energy and Climate Research  
Materials Synthesis and Processing (IEK-1)

# Dual Phase Oxygen Transport Membrane for Efficient Oxyfuel Combustion

Madhumidha Ramasamy

Schriften des Forschungszentrums Jülich  
Reihe Energie & Umwelt / Energy & Environment

Band / Volume 351

---

ISSN 1866-1793

ISBN 978-3-95806-196-5

Bibliographic information published by the Deutsche Nationalbibliothek.  
The Deutsche Nationalbibliothek lists this publication in the Deutsche  
Nationalbibliografie; detailed bibliographic data are available in the  
Internet at <http://dnb.d-nb.de>.

Publisher and  
Distributor: Forschungszentrum Jülich GmbH  
Zentralbibliothek  
52425 Jülich  
Tel: +49 2461 61-5368  
Fax: +49 2461 61-6103  
Email: [zb-publikation@fz-juelich.de](mailto:zb-publikation@fz-juelich.de)  
[www.fz-juelich.de/zb](http://www.fz-juelich.de/zb)

Cover Design: Grafische Medien, Forschungszentrum Jülich GmbH

Printer: Grafische Medien, Forschungszentrum Jülich GmbH

Copyright: Forschungszentrum Jülich 2016

Schriften des Forschungszentrums Jülich  
Reihe Energie & Umwelt / Energy & Environment, Band / Volume 35 1

D 294 (Diss., Bochum, Univ., 2016)

ISSN 1866-1793  
ISBN 978-3-95806-196-5

The complete volume is freely available on the Internet on the Jülicher Open Access Server (JuSER)  
at [www.fz-juelich.de/zb/openaccess](http://www.fz-juelich.de/zb/openaccess).



This is an Open Access publication distributed under the terms of the [Creative Commons Attribution License 4.0](https://creativecommons.org/licenses/by/4.0/),  
which permits unrestricted use, distribution, and reproduction in any medium, provided the original work is properly cited.

## Abstract

Oxygen transport membranes (OTMs) are attracting great interest for the separation of oxygen from air in an energy efficient way. A variety of solid oxide ceramic materials that possess mixed ionic and electronic conductivity (MIEC) are being investigated for efficient oxygen separation (Betz '10, Skinner '03). Unfortunately these materials do not exhibit high degradation stability under harsh ambient conditions such as flue gas containing CO<sub>2</sub>, SO<sub>x</sub>, H<sub>2</sub>O and dust, pressure gradients and high temperatures that are typical in fossil fuel power plants. For this reason, dual phase composite membranes are developed to combine the best characteristics of different compounds to achieve high oxygen permeability and sufficient chemical and mechanical stability at elevated temperatures.

In this thesis, the dual phase membrane Ce<sub>0.8</sub>Gd<sub>0.2</sub>O<sub>2-δ</sub> - FeCo<sub>2</sub>O<sub>4</sub> (CGO-FCO) was developed after systematic investigation of various combinations of ionic and electronic conductors. The phase distribution of the composite was investigated in detail using electron microscopes and this analysis revealed the phase interaction leading to grain boundary rock salt phase and formation of perovskite secondary phase. A systematic study explored the onset of phase interactions to form perovskite phase and the role of this unintended phase as pure electronic conductor was identified. Additionally optimization of conventional sintering process to eliminate spinel phase decomposition into rock salt was identified. An elaborate study on the absolute minimum electronic conductor requirement for efficient percolation network was carried out and its influence on oxygen flux value was measured. Oxygen permeation measurements in the temperature range of 600 °C - 1000°C under partial pressure gradient provided by air and argon as feed and sweep gases are used to identify limiting transport processes.

The dual phase membranes are much more prone to surface exchange limitations because of the limited length of the active triple phase boundaries. A porous catalytic layer made of a single phase MIEC material, i.e. LSCF, showed evidence of these limitations even when using 1 mm thick samples. The dual phase composites were also subjected to thermo-chemical stability in flue gas conditions and mechanical stability under high pressure applications. Microstructure variation based on different powder synthesis routes of the composite impacting oxygen permeation has been investigated. On the other hand, microstructure variation via alternate

densification/ sintering techniques such as hot pressing and SPS/FAST were also explored. The finalized dual phase composition was developed into thin film supported membrane layers. An oxygen flux of  $1.08 \text{ ml cm}^{-2} \text{ min}^{-1}$  was achieved on an asymmetric membrane at  $1015 \text{ }^\circ\text{C}$  successfully. However, impregnation of catalysts into the porous support can significantly improve the oxygen flux at lower temperatures, overcoming the surface limitations at the interface between the support and dense membrane.

## Kurzfassung

Sauerstofftransportmembranen sind von großem Interesse für die energieeffiziente Abtrennung von Sauerstoff aus Luft. Hierfür werden verschiedene oxidische Keramiken mit gemischter Ionen- und Elektronenleitung (Mixed Ionic Electronic Conductors, MIEC) untersucht. Leider besitzen diese Materialien keine ausreichende Degradationsstabilität in aggressiven Umgebungsbedingungen wie sie z.B. in Kraftwerken vorkommen, d.h. Abgase mit hohen Anteilen an  $\text{CO}_2$ ,  $\text{SO}_x$ ,  $\text{H}_2\text{O}$  und Staub sowie Druckdifferenzen und hohen Temperaturen. Aus diesem Grund werden zweiphasige Komposit-Membranen entwickelt, die beste Eigenschaften verschiedener Materialien kombinieren, um eine hohe Permeabilität sowie ausreichende chemische und mechanische Stabilität bei hohen Temperaturen zu erzielen.

In dieser Arbeit wurde auf Basis einer systematischen Untersuchung verschiedener ionisch und elektronisch leitenden Keramiken eine Komposit-Membran aus  $\text{Ce}_{0,8}\text{Gd}_{0,2}\text{O}_{2-\delta} - \text{FeCo}_2\text{O}_4$  (CGO-FCO) entwickelt. Die Phasenverteilung des Komposits wurde mit Hilfe elektronenmikroskopischer Methoden detailliert untersucht, wobei sich herausstellte, dass die Wechselwirkung der Phasen zu einer Korngrenzphase mit Kochsalzstruktur und der Bildung einer neuen Phase mit Perowskitstruktur führt. Eine systematische Studie erforschte den Beginn der Perowskitphasenbildung und die Rolle dieser Phase, die als reiner Elektronenleiter wirkt. Des Weiteren führte eine Optimierung des Sinterprozesses dazu, dass die teilweise Zersetzung des Spinells in die Kochsalzphase vermieden bzw. rückgängig gemacht werden kann. Es wurde eine ausführliche Untersuchung zur Bestimmung des Minimums des benötigten Phasenanteils des Spinells zur Erreichung einer ausreichenden Perkolation durchgeführt und dessen Einfluss auf den Sauerstofffluss gemessen. Mit Hilfe von Messungen der Sauerstoffpermeation zwischen 600 und 1000 °C unter einem Sauerstoffpartialdruck-Gradienten (Luft als Feed – Argon als Sweep) wurden limitierende Transportprozesse identifiziert.

Die Komposit-Membranen sind deutlich anfälliger für Limitationen durch Oberflächenaustauschprozesse wegen der begrenzten Länge der katalytisch wirksamen Dreiphasengrenzen. Eine poröse katalytisch aktive Schicht aus dem einphasigen MIEC-Material  $\text{La}_{0,58}\text{Sr}_{0,4}\text{Co}_{0,2}\text{Fe}_{0,8}\text{O}_{3-\delta}$  (LSCF) zeigt die Aufhebung solcher Einflüsse schon bei 1 mm dicken Membranen. Die Komposite wurden ebenfalls bezüglich ihrer thermo-chemischen Stabilität in Abgasbedingungen untersucht. Unterschiede in der Mikrostruktur, die durch unterschiedliche

Syntheserouten hervorgerufen werden, beeinflussen die Sauerstoffpermeation zusätzlich. Andererseits wurden auch Mikrostrukturvariationen durch alternative Verdichtungs- bzw. Sintertechnologien wie z.B. Heißpressen, feldunterstütztes Sintern, untersucht. Mit der optimierten Komposit-Verbindung wurde eine dünne gestützte Membranschicht entwickelt. Ein Sauerstofffluss von  $1.08 \text{ ml cm}^{-2} \text{ min}^{-1}$  wurde mit dieser asymmetrischen Membran bei  $1015 \text{ }^\circ\text{C}$  erreicht. Eine Imprägnierung des porösen Trägers mit Katalysatoren zur Überwindung von Limitationen durch Oberflächenaustausch bietet das Potenzial, diesen Fluss insbesondere bei niedrigeren Temperaturen signifikant zu steigern.

# Contents

Abstract.....	I
Kurzfassung .....	III
Abbreviations .....	VII
Symbols .....	VIII
1. Introduction and Objective .....	1
2. Fundamentals .....	5
2.1. Oxygen Transport Membranes .....	5
2.1.1. <i>Bulk Diffusion</i> .....	6
2.1.2. <i>Surface Exchange</i> .....	7
2.2. Membrane Structure.....	10
2.3. Material Selection .....	11
2.3.1. <i>Mixed Ionic and Electronic Conductors</i> .....	11
2.3.2. <i>Ionic Conductors</i> .....	14
2.3.3. <i>Electronic Conductors</i> .....	15
3. Experimental Methods .....	21
3.1. Membrane Fabrication .....	21
3.2. Membrane Characterization.....	29
3.3. Membrane Performance.....	34
4. Results and Discussion .....	41
4.1. Material Selection .....	41
4.1.1. <i>Ce<sub>0.8</sub>Gd<sub>0.2</sub>O<sub>2-δ</sub> - M(Co<sub>2</sub>O<sub>4</sub>), M=Fe, Mn</i> .....	42
4.1.2. <i>Ce<sub>0.8</sub>Gd<sub>0.2</sub>O<sub>2-δ</sub> - CoO</i> .....	45
4.1.3. <i>Ce<sub>0.8</sub>Gd<sub>0.2</sub>O<sub>2-δ</sub> - FeCr<sub>2</sub>O<sub>4</sub></i> .....	47
4.1.4. <i>Ce<sub>0.8</sub>Gd<sub>0.2</sub>O<sub>2-δ</sub> - SrTi<sub>0.65</sub>Fe<sub>0.35</sub>O<sub>3</sub></i> .....	48
4.1.5. <i>Ce<sub>0.8</sub>Gd<sub>0.2</sub>O<sub>2-δ</sub> - La<sub>2</sub>Ni<sub>0.5</sub>Co<sub>0.5</sub>O<sub>3</sub></i> .....	51
4.1.6. <i>Ce<sub>0.8</sub>Gd<sub>0.2</sub>O<sub>2-δ</sub> - La<sub>2</sub>NiO<sub>4</sub></i> .....	52

4.1.7. <i>Conclusion on Section 4.1</i> .....	55
4.2. $\text{Ce}_{0.8}\text{Gd}_{0.2}\text{O}_{2-\delta}$ - $\text{FeCo}_2\text{O}_4$ Dual Phase Composite .....	56
4.2.1. <i>CGO-FCO Phase Evolution</i> .....	56
4.2.2. <i>CGO-FCO Performance</i> .....	67
4.2.3. <i>CGO-FCO Stability</i> .....	76
4.3. Processing and Microstructure Optimization .....	86
4.3.1. <i>Alternative Powder Synthesis</i> .....	86
4.3.2. <i>Alternative Sintering techniques</i> .....	91
4.3.3. <i>Asymmetric Membrane by Tape Casting</i> .....	100
5. Summary and Outlook .....	112
6. References .....	115
7. Figures & Tables .....	126
8. Acknowledgements .....	134

## Abbreviations

OTM	Oxygen Transport Membrane
MIEC	Mixed Ionic and Electronic Conductivity
C <sub>2</sub>	Hydrocarbon
TPB	Triple Phase Boundary
SP	Spray Pyrolysis
CCS	Carbon Capture and Storage
POM	Partial Oxidation of Methane
OCM	Oxidative Coupling of Methane
ORNL	Oak Ridge National Laboratory
XRD	X-ray diffraction
SEM	Scanning Electron Microscopy
EDS	Energy Dispersive X-ray Spectroscopy
STEM-HAADF	Scanning Transmission Electron Microscopy High Angle Annular Dark Field
EELS	Electron Energy Loss Spectroscopy
ToF-SIMS	Time of Flight - Secondary Ion Mass Spectroscopy
TG	Thermo-Gravimetry
DTA	Differential Thermal Analysis

## Materials

CGO	Ce <sub>0.8</sub> Gd <sub>0.2</sub> O <sub>2-δ</sub>
FCO	FeCo <sub>2</sub> O <sub>4</sub>
LSCF	La <sub>0.6</sub> Sr <sub>0.4</sub> Co <sub>0.2</sub> Fe <sub>0.8</sub> O <sub>3-δ</sub>
BSCF	Ba <sub>0.5</sub> Sr <sub>0.5</sub> Co <sub>0.8</sub> Fe <sub>0.2</sub> O <sub>3-δ</sub>
8YSZ	(8Y <sub>2</sub> O <sub>3</sub> -ZrO <sub>2</sub> )
MCO	MnCo <sub>2</sub> O <sub>4</sub>
LNO	La <sub>2</sub> NiO <sub>4</sub>
LNC	La <sub>2</sub> Ni <sub>0.5</sub> Co <sub>0.5</sub> O <sub>3</sub>
FCrO	FeCr <sub>2</sub> O <sub>4</sub>
STF35	SrTi <sub>0.65</sub> Fe <sub>0.25</sub> O <sub>3</sub>

CGPO	$\text{Ce}_{0.8}\text{Gd}_{0.1}\text{Pr}_{0.1}\text{O}_{2-6}$
GCFCO	$\text{Gd}_{0.85}\text{Ce}_{0.15}\text{Fe}_{0.75}\text{Co}_{0.25}\text{O}_3$

## Symbols

R	Gas constant ( $8.314 \text{ J}\cdot\text{mol}^{-1}\cdot\text{K}^{-1}$ )
j	Flux ( $\text{ml}\cdot\text{cm}^{-2}\cdot\text{min}^{-1}$ )
L	Thickness(cm)
T	Temperature( K or °C)
$\eta_k$	Electrochemical Potential ( $\text{J}\cdot\text{C}^{-1}\cdot\text{mol}^{-1}$ )
$\mu_k$	Chemical Potential ( $\text{J}\cdot\text{mol}^{-1}$ )
$\phi$	Electrical Potential ( $\text{J}\cdot\text{C}^{-1}$ )
$\sigma$	Conductivity ( $\text{S}\cdot\text{cm}^{-1}$ )
$p'$	Partial Pressure (bar)
$k_s$	Surface Exchange Coefficient ( $\text{cm}\cdot\text{s}^{-1}$ )
$D_s$	Diffusion Coefficient ( $\text{cm}^2\cdot\text{s}^{-1}$ )
$L_c$	Characteristic Thickness (cm)
c	Concentration ( $\text{mol}\cdot\text{cm}^3$ )
TEC	Thermal Expansion Coefficient ( $^{\circ}\text{C}^{-1}$ )
m	Mass (g)
$\rho$	Density ( $\text{g}\cdot\text{cm}^3$ )
$E_a$	Activation Energy ( $\text{kJ}\cdot\text{mol}^{-1}$ )
F	Flow Rate ( $\text{ml}\cdot\text{min}^{-1}$ )
A	Area ( $\text{cm}^2$ )
p	Pressure (Mpa)
P	Permeance ( $\text{mol}\cdot\text{cm}^2\cdot\text{s}^{-1}$ )
R	He Leak Test Value ( $\text{mbar}\cdot\text{l}\cdot\text{cm}^{-2}\cdot\text{s}^{-1}$ )

# 1. Introduction and Objective

Renewable energy's contribution to the energy demand of the globe is highly researched over the past few decades. Nevertheless, at present fossil fuel power plants play a significant role in meeting the energy needs of the growing population throughout the world. Consequently, fossil energy carriers account for approximately one third of total emissions of the greenhouse gas  $\text{CO}_2$  (Edenhofer '14). In the last decade, reduction of  $\text{CO}_2$  emissions by the development of  $\text{CO}_2$  mitigation scenarios utilizing carbon capture and storage (CCS) technology for large point sources has gained interest. One very promising concept is the oxyfuel technology, which realizes the combustion of fossil fuels with oxygen enriched re-circulated flue gas, thus requiring enormous quantities of oxygen. This oxyfuel process has the potential to minimize the efficiency losses and reduce  $\text{CO}_2$  emissions. Oxygen Transport Membranes (OTM) can deliver this oxygen efficiently if the required heat for the operation is generated by the process itself as is the case in power plants (Figure 1) in place of traditional air-fired combustion process. Such OTMs are also applicable in industrial sectors such as iron, steel, cement and glass plants that are major contributors of greenhouse gas emissions and where combustion is the primary process source for heat (Czyperek '09, Sunarso '08).

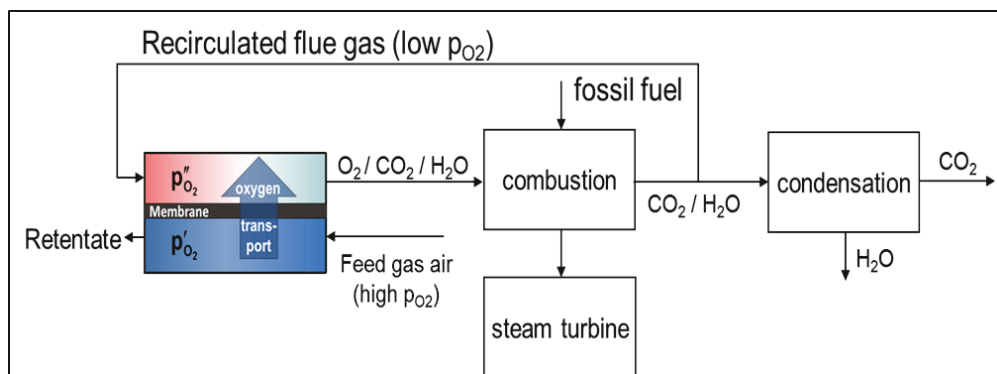


**Figure 1 Schematic diagram of the oxyfuel combustion process in a power plant.**

In addition to producing high purity oxygen, OTMs can also be integrated in catalytic membrane reactors where oxygen is directly consumed by a chemical reaction e.g. for carrying out different petro-chemical processes (Cao '13, Lobera '11). In this context, the research focuses on the

## 1 Introduction and Objective

partial oxidation of methane (POM) to syngas and oxidative coupling of methane (OCM) to higher hydrocarbons (abbreviated as “C<sub>2</sub>”) such as ethylene and ethane. These promising processes are used for direct conversion of natural or bio gas into more useful C<sub>2</sub> products (Burggraaf '96, Sanchez '96). In case of POM reaction for syngas production, the main advantage of OTM is that air can be used instead of oxygen, which reduces the cost by eliminating the need for an additional oxygen separation unit.



Also, the gradual introduction of oxygen reduces contact with the partially oxidized products, thereby enhancing the yield of the desired products (Dong '11).



The reaction efficiency of OCM is greatly improved by OTM which delivers the oxygen into the reaction compartment in the form of dissociated and ionized oxygen. The interaction of ionized oxygen with methane on the membrane surface follows a different reaction mechanism compared to passing oxygen gas from external source. Thus the by-reactions are minimized, and increased selectivity of C<sub>2</sub> products can be achieved.

OTMs were commonly made of mixed ionic electronic conductors (MIEC), which consist of single phase membrane materials (Sunarso '08). State of the art OTMs made from La<sub>0.6</sub>Sr<sub>0.4</sub>Co<sub>0.2</sub>Fe<sub>0.8</sub>O<sub>3-δ</sub> (LSCF) and Ba<sub>0.5</sub>Sr<sub>0.5</sub>Co<sub>0.8</sub>Fe<sub>0.2</sub>O<sub>3-δ</sub> (BSCF) have shown exceptional permeability for oxygen. But these OTM materials are prone to phase instability and carbonate formation on exposure to pure CO<sub>2</sub> under chemical potential gradient at elevated temperatures (Baumann '10, Baumann '11, Serra '13). Considering the application of these OTMs predominantly in power plants and industrial sectors where operating conditions include exposure to flue gases containing CO<sub>2</sub>, SO<sub>x</sub>, H<sub>2</sub>O and dust components (Betz '10), stability of these single phase OTM materials is questionable.

In general, the bulk transport is based on defects in the crystal lattice, i.e. oxygen vacancies and electron holes. This leads to a trade-off between permeability requiring a high defect concentration, and stability requiring a low defect concentration. Therefore, materials with limited permeability have to be used in many applications to provide a long term stable operation (Baumann '13, Schafbauer '12). To overcome this limitation, OTMs developed from a dual phase

composite have gained great research interest in the past two decades. These composites are combination of two separate phases, each phase providing electronic or ionic conductivity respectively. Such dual phase composites are expected to provide reasonable oxygen permeation and clearly improved chemical stability under flue gas condition (van Hassel '04, Zhu '11). Several research articles have reported about development of single phase MIEC perovskites and dual phase composites. In most cases, they have only been tested so far for their stability in CO<sub>2</sub> atmospheres (Huixia '11, Luo '11, Luo '12, Xue '13, Zhu '12), but flue gas also contains SO<sub>2</sub> and H<sub>2</sub>O (Balaguer '13). Hence stability testing of membranes in CO<sub>2</sub>, SO<sub>2</sub> and H<sub>2</sub>O containing gas mixture would be a reasonable replication of its operating conditions in industries.

Additionally, in order to obtain high permeation rates, dual phase composites are developed into thin supported membrane layers of different shapes, mainly planar or as capillaries (Baumann '13, Li '09, Sadykov '10). In case of thin film membranes, surface exchange kinetics become rate limiting because of the relatively fast diffusion through the bulk membrane. Consequently, the solid-gas electrochemical interfaces become more and more important, making catalytically active layers, such as porous electrodes, the key element in the future development of long term stable, high performance membranes (Zhu '11, Zhu '08).

### **Objective**

The objective of this work is to develop a new and innovative dual phase membrane system for the purpose of separating oxygen from air. In the functional layer, an oxygen ion conducting phase with a suitable electron conducting oxide phase will be combined. Several material combinations will be screened based on the homogenous phase distribution and oxygen separation performance discussed in detail in the material selection section (4.1). The shortlisted composite material will be subjected to comprehensive characterization of the microstructure and phase analysis, as phase interactions are inevitable when two materials are mixed and subjected to heat treatment at high temperatures. Such investigations help to understand the influence on oxygen transport processes in the membrane due to phase interactions if any and secondary phase formations. Subsequently, the composite will also be analyzed for its performance based on the electrical conductivity and oxygen flux measurements. Parallel experiments will be made to test the chemical stability of the material under conditions closely replicating industrial flue gas environment. Such chemical stability experiments are first of their type to be tested for dual

## 1 Introduction and Objective

phase composites by exposing the membranes to mixture of CO<sub>2</sub>, SO<sub>2</sub> and H<sub>2</sub>O containing gas compounds at the operating temperature of 850 °C. These stability experiments will be carried out at Oak Ridge National Laboratory (ORNL), USA as part of bilateral collaborative project between Forschungszentrum Juelich (IEK-1) and ORNL, USA. The optimized composite material will then be developed into asymmetric membranes by sequential tape casting process. This thin membrane with a suitable support structure undergoes process optimization until a stable, asymmetric membrane system can be fabricated with a good thermal stability and acceptable oxygen flow. The work also includes investigation of porous catalytic layer on the dense membrane side and catalyst impregnation in porous support structure to overcome the surface exchange limitations that are expected in an asymmetric membrane. Finally, **an oxygen flux of 1 ml cm<sup>-2</sup> min<sup>-1</sup> at the operating temperature of 850 °C** from optimized asymmetric membrane architecture will be the milestone to be achieved.

## 2. Fundamentals

### 2.1. Oxygen Transport Membranes

Mixed Ionic and Electronic Conducting (MIEC) oxygen transport membranes are able to separate oxygen from air at high temperature in contrast to the conventional cryogenic separation method (Czyperek '09). In principle oxygen transport through a dense membrane involves lattice diffusion of oxides in the bulk membrane and surface exchange reactions at the surfaces on both sides of the membrane. Both steps are not viable without any driving force, i.e. no oxygen partial pressure gradient. In this case, the hopping is statistically distributed (Burggraaf '96). When a partial pressure gradient is applied, the hopping is directed from the high pressure to the low-pressure side, resulting in oxygen ion diffusion as shown in Figure 2.

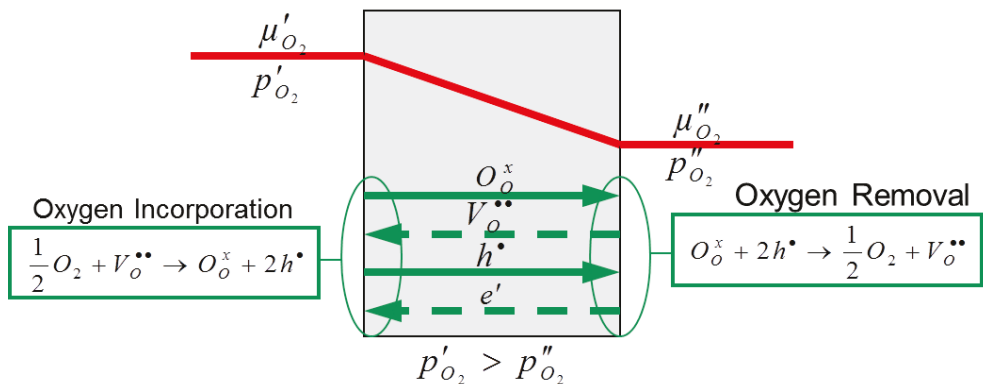


**Figure 2 Oxygen ion transport through a dense ion-electronic conducting membrane.**

At the side with high oxygen partial pressure, the vacancies are occupied by oxygen ions, which are generated by ionization and dissociation of molecular oxygen in the gas phase. At the side with low partial pressure, the oxygen is released into the gas phase (Burggraaf '96, van Hassel '04). There are several oxygen transport models defining the transport mechanism in categorized steps. A typical OTM is a supported asymmetric membrane structure in which complexity of the transport is given by a series of resistances corresponding to the rate limiting steps as shown in Figure 3.

## 2 Fundamentals

These resistances comprise of bulk diffusion (Zone III), surface exchange reactions (Zone II and IV) and concentration polarization in the gas phase (Zone I) as well as in the pores of the support (Zone V and VI). This concentration polarization is defined as oxygen depletion or accumulation in the support and activation layer pores and gas phases, lowering oxygen partial pressure. Each of these steps shows different level of dependence on the oxygen partial pressure at the zone boundaries (Baumann '11, Niehoff '14, Schulze-Küppers '13).

However, the resistance between the gas phase and the membrane is negligible (Liu '06) hence; the transport mechanisms of the bulk transfer (zone III) and the surface exchange (zones II and IV) are explained in detail below.

### 2.1.1. Bulk Diffusion

Bulk diffusion corresponds to a neighboring oxygen ion hopping into a vacancy through the crystal lattice accompanied by continuous flux of electrons in the opposite direction maintaining the electro neutrality without any external circuit.

According to Nernst- Planck equation,

$$j_k = \frac{\sigma_k}{z_k^2 F^2} \nabla \eta_k \quad (4)$$

$$\text{where } \nabla \eta_k = \nabla \mu_k + z_k F \nabla \phi \quad (5)$$

the mobility/flux  $j_k$  of a MIEC material with conductivity  $\sigma_k$  depends mainly on the chemical potential gradient  $\nabla \mu_k$  since electrical potential gradient  $\nabla \phi$  is assumed to be zero in the electrochemical potential gradient factor  $\nabla \eta_k$ .  $\nabla \mu_k$  is defined as

$$\nabla \mu_k = RT \frac{\partial \ln \frac{p'_{O_2}}{p''_{O_2}}}{\partial x} \quad (6)$$

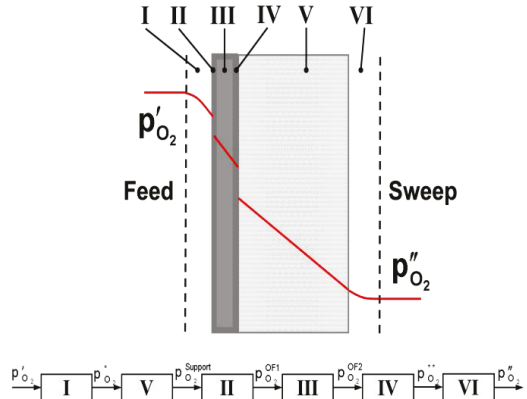


**Figure 3 Resistance model of asymmetric membrane and its distributed concentration profile(Niehoff '14)**

where  $R$  is gas constant and  $T$  is temperature and  $p'_{O_2}$  and  $p''_{O_2}$  are the oxygen partial pressure on the oxygen-rich and oxygen-lean side, respectively. In a steady state condition, the flux of oxygen vacancies is in balance with the counter flux of electrons and holes, as long as no external current is imposed. Thus, the chemical potential gradient  $\nabla\mu_k$ , a function of temperature and partial pressure gradient is the only factor influencing the flux of oxygen vacancies. Therefore, this oxygen diffusion  $J_{O_2}$  through a solid crystal can be described by the Wagner equation:

$$J_{O_2} = \frac{RT}{16F^2} \frac{1}{\sigma_{amb}} \frac{1}{L} \ln \frac{p'_{O_2}}{p''_{O_2}} \quad (7)$$

where  $R$  is the gas constant,  $T$  is temperature,  $F$  is the Faraday constant,  $\sigma_{amb}$  is ambipolar conductivity,  $L$  is the membrane thickness, and  $p'_{O_2}$  and  $p''_{O_2}$  are the oxygen partial pressure on the oxygen-rich and oxygen-lean side, respectively (Betz '10, Bouwmeester '96, Dong '11). The only material parameter in the Wagner equation is ambipolar conductivity, which is composed of the ionic  $\sigma_i$  (oxygen vacancies) and electronic conductivity  $\sigma_e$  (electrons and holes) of the material chosen subsequently influencing the bulk diffusion of the membrane given by equation 8:

$$\sigma_{amb} = \frac{\sigma_i \cdot \sigma_e}{\sigma_i + \sigma_e} \quad (8)$$

### 2.1.2. Surface Exchange

According to Wagner's steady state solid diffusion equation (Equation 7), oxygen flux is inversely proportional to the bulk membrane thickness. Thus, decreasing the membrane thickness increases the oxygen flux through the membrane. This is true until a certain thickness, beyond which marks the transition where the predominant bulk diffusion is limited by the surface exchange kinetics of the membrane at the gas/solid interfaces. In other words, the oxygen transport is due to equal contribution of bulk diffusion and surface exchange reaction. This value is known as the characteristic thickness  $L_c$ . Considering the influence of  $L_c$  on diffusion and interfacial exchange, Wagner's equation has to be modified as (Bouwmeester '96):

$$J_{O_2} = \frac{RT}{(4F^2)} \cdot \frac{1}{L+2L_c} \cdot \frac{\sigma_i \cdot \sigma_e}{\sigma_i + \sigma_e} \cdot \ln \frac{p'_{O_2}}{p''_{O_2}} \quad (9)$$

## 2 Fundamentals

Assuming that the partial pressure gradient is very small,  $j_{O_{2ex}}$  is the balanced exchange rate on both sides of the membrane surface and  $k_s$  is the surface exchange coefficient that can be determined from  $^{18}\text{O}$ - $^{16}\text{O}$  isotopic exchange experiments. Under these conditions,  $L_c$  is defined as

$$L_c = \frac{RT}{(4F^2)} \cdot \frac{\overline{\sigma_i \sigma_e}}{\sigma_i + \sigma_e} \cdot \frac{1}{j_{O_{2ex}}}, \quad (10)$$

$$\text{where } j_{O_{2ex}} = \frac{1}{4} k_s c_O \quad (11)$$

Since electronic conduction is predominant for most MIEC membranes, the Nernst-Einstein equation for ionic conductivity is written as:

$$\sigma_{ion} = \frac{c_O D_s z_O^2 F^2}{RT} \quad \text{where } D_s \text{ is the oxygen diffusion coefficient.} \quad (12)$$

Substituting Equation 11 and 12 into Equation 10 leads to:

$$L_c = \frac{D_s}{k_s} \quad (13)$$

where  $L < L_c$  indicates no further increase in oxygen flux with decreasing membrane thickness as surface exchange kinetics dominate the oxygen transport (Bouwmeester '96, Xing '12). Thickness dependence behavior of a MIEC material (BSCF) impacting the oxygen permeation is depicted in Figure 4.

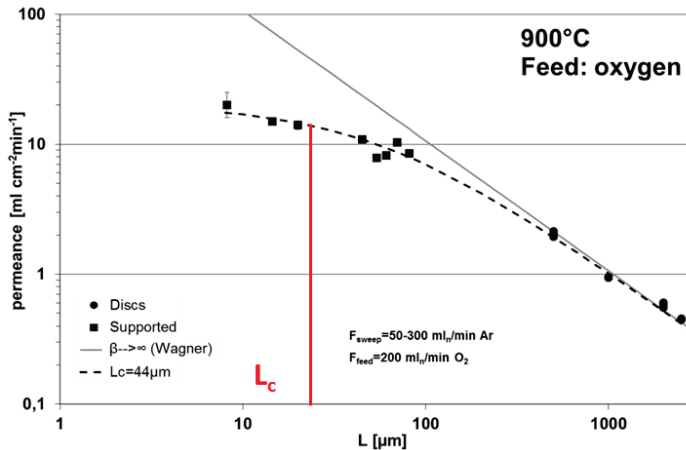
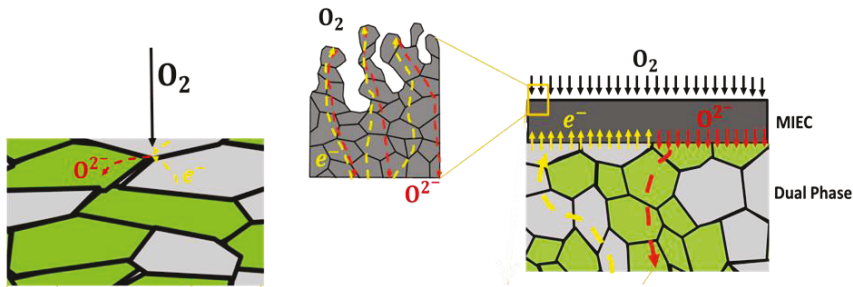


Figure 4 Thickness dependence of the permeance of BSCF membranes is plotted along with fitted line of the calculated flux using Wagner's equation for the corresponding membrane thicknesses. The calculated value of  $L_c$  using the modified Wagner's equation is marked to indicate the predicted transition of oxygen transport limitation (Baumann '15).

The plot shows the permeance measurements obtained using BSCF material made into bulk discs and supported asymmetric membranes of varying thickness. The plot also includes a fitted line of calculated values using the Wagner's equation (Equation 7), data corresponding to oxygen permeance of BSCF membranes with reducing thickness. Since the calculated value does not take into account the influence of  $L_c$ , the deviation of the plot in comparison to the experimental values plot is clearly observed. The calculated  $L_c$  is marked to indicate the transition below which surface exchange limitations are predominant. Thus, MIEC membranes' oxygen transport is greatly influenced by the surface exchange reaction on the surface of the membrane at the high and low  $p_{O_2}$  sides.

In an ideal dual phase membrane, a prerequisite is a continuous path for both ionic and electronic conduction. But in reality, interconnectivity between particles will not be ideal and only part of the surface is effective towards oxygen exchange (Bouwmeester '96, Burggraaf '96). Thus, in comparison to an OTM made of single phase MIEC material, a dual phase membrane is more prone to surface exchange limitations due to possible inhomogeneous distribution of phases. Triple Phase Boundary (TPB) i.e. the interface of oxygen containing gas phase, oxygen vacancy containing ionic conductor, and electron hole containing electronic conductor to form the percolative network is one of the factors influencing surface exchange reactions as shown in Figure 5.



**Figure 5 Schematic diagram of ions and electrons transport via Triple Phase Boundary (TPB)**

This reaction at the surface is confined to the TPB given by the Equation 14:



## 2 Fundamentals

Where  $V_O^{\bullet\bullet}$ ,  $h^{\bullet}$  and  $O_O^x$  are oxygen vacancy, electron hole, and lattice oxygen ion, respectively while the half oxygen is the gas phase (Kröger '56). Thus, the oxygen transport performance of these membranes can be improved by extending the TPB (Zhu '11, Zhu '08). The lengths of TPB can be prolonged by applying a coat of mixed ionic-electronic conducting porous activation layer on the surfaces of the membranes (Adler '04, Baumann '11).

### 2.2. Membrane Structure

As already mentioned, at  $L > L_c$  oxygen permeation of a membrane improves significantly with decreasing membrane thickness in bulk diffusion. Thus, development of several micrometer thick dense layer of membrane is a promising approach since the permeate path of the membrane and flow resistance is significantly reduced. However, to have a mechanically stable thin dense OTM with high flux output, the thin film should be supported by a strong mechanical structure classified as asymmetric membrane structure. Typical architecture of asymmetric membranes as shown in Figure 6 consists at least of a macro-porous support to ensure mechanical stability, dense thin membrane layer and porous catalytic layers on both sides of the membrane addressing the surface activation limitation.

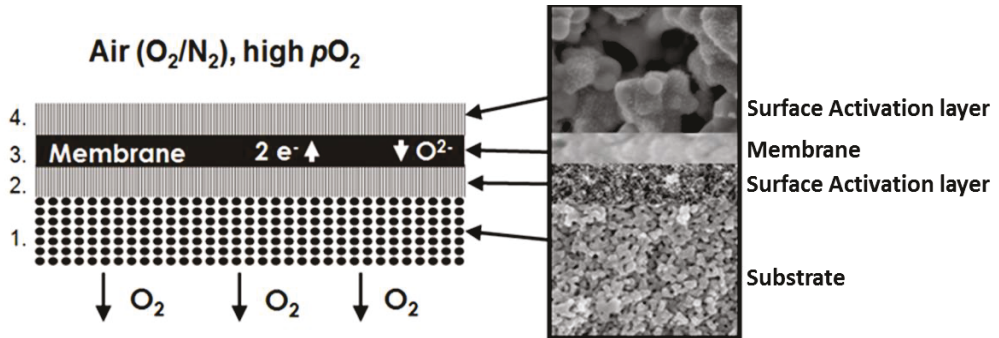


Figure 6 Cross section of a membrane assembly comprising of porous support, dense membrane layer, and porous surface activation layer.

This porous mechanical support required for the stability of the thin film membrane has a strong impact on the gas transport to the membrane layer as well. Furthermore, such a mechanical support should meet requirements like similar thermal expansion coefficient to the dense membrane layer, sufficient chemical stability at processing temperature and sufficient chemical stability during the long term operating conditions (Ohnishi '08). In the Literature, use of  $MgO$ ,

CeO<sub>2</sub>, YSZ and so on as low cost ceramic oxide porous supports that simplify the fabrication process are proposed (Lipińska-Chwałek '14, Pirou '16, Yin '06). However due to thermal expansion mismatch, high tensile stress is induced in the membrane layer at operating temperature which reduces the oxygen flux as well. Nevertheless, use of the membrane material itself as porous support and catalytic layer is a logical approach to overcome the thermal expansion mismatch (Baumann '11, Serra '13).

According to the resistance model (Figure 3), in such a supported asymmetric membrane, concentration polarization in the pores plays an important role in oxygen transport. For example, if the support pores are small, convection does not occur and the gas transport is realized by diffusion only when a sweep gas is used. Thus porosity of the support and catalytic layer need to be optimized balancing both aspects, i.e. high permeability requiring high porosity, and sufficient mechanical stability requiring limited porosity (Baumann '13, Cao '14, Joo '14). One other important factor is tortuosity (diffusion length in a porous media) through the pores which is highly influenced by the pore shape and volume in the support. In comparison to an ideal membrane assembly (Figure 6), actual asymmetric membrane does not include a surface activation layer between the dense membrane and porous support due to difficulty in the fabrication process by tape casting. Hence to overcome the surface limitation, catalytic infiltration of nanometer grains is introduced between the macro-pores in the support and the dense membrane layer. With the use of same material for the porous support and catalyst activation, tortuosity factor needs additional consideration when analyzing the oxygen transport mechanism in a dual phase membrane. Research groups have reported use of MIEC perovskite, composites and metallic particles impregnated in the porous structure as additional catalysts eliminating surface exchange limitations and improving the oxygen flux of the membranes (Pirou '16, Solis '14).

## 2.3. Material Selection

### 2.3.1. Mixed Ionic and Electronic Conductors

It is usual to limit the use of the name MIEC to materials in which both  $\sigma_{\text{ion}}$  and  $\sigma_e$  do not differ by more than 2 orders of magnitude and show not too low values ( $\sigma_{\text{ion}}, \sigma_e \geq 10^{-5} \text{ S cm}^{-1}$ ). MIECs are well-known candidates for high temperature electrochemical devices, such as electrodes or

## 2 Fundamentals

electrocatalysts, and ceramic membranes for oxygen separation or partial oxidation of light hydrocarbons. The mixed ionic–electronic conductivity allows one to induce migration of charged species (electrons in one direction, ions in the other one) inside the material without any electrical connection to the sample surfaces (Vernoux '13). Perovskites are a well-known group of mixed conductors often used for oxygen separation membranes.

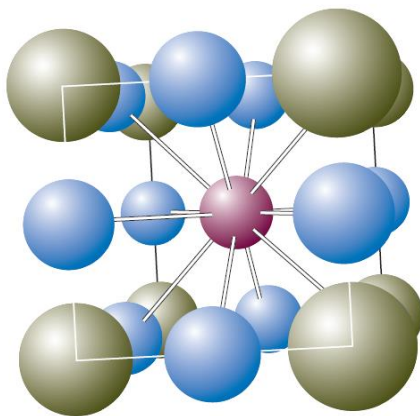


**Figure 7 Perovskite crystal structure where red sphere represent the A-cation, green spheres represent the B-cations and small blue spheres are oxygen ions. Reprinted from (Skinner '03) with permission of Elseviers.**

Some prominent materials of the perovskite group are: 1) Ferrite type perovskites which exhibit good mixed conductivity but due to structural constraints and defect chemistry, electronic transport is limited. 2) Cobaltite type perovskite (Ln, Sr)  $\text{CoO}_3-\delta$  materials possess high mixed conductivity and fast exchange kinetics but very high thermal and chemical expansion (Betz '10, Feltz '91, Gauquelin '09). However poor chemical stability in harsh environments of these perovskites has forced the research community to explore alternate materials.

MIEC membranes are alternatively developed by the combination of electronic conducting material and oxygen ionic conducting material, called as dual-phase membranes. Although the dual-phase membrane is an old concept, it shows unique advantages. At first, the electronic conducting phase used in dual phase membrane was noble metal, but the amount of noble metal necessary to obtain an efficient percolating network meant higher cost of noble metals as a

disadvantage. Thus, it was replaced by the pure electronic conducting oxides such as perovskites, spinels and also by perovskite MIEC materials as shown in Figure 8.

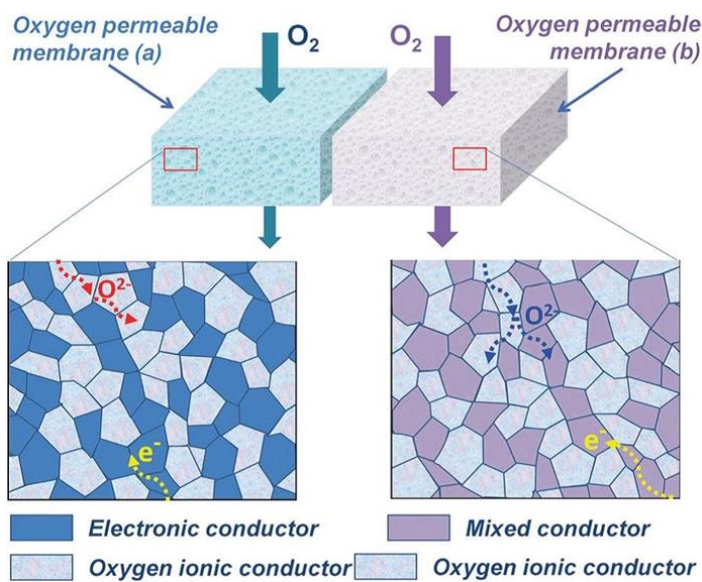


**Figure 8** Schematic picture of oxygen ionic/pure electronic conductor dual-phase membrane (left) and oxygen ionic/mixed conductor dual-phase membrane (right). Reproduced from (Dong '11) with permission of The Royal Society of Chemistry.

Compared with the single phase MIEC membranes, the oxygen ionic conduction in dual-phase membranes mainly depends on fluorite structure oxides, which are very stable under reaction environments and with lower thermal expansion rates (Dong '11). The second phase which can be pure electronic conducting or MIEC oxide depends mainly on the thermal expansion match, with the ionic conducting phase. In addition, the ability of the second phase to provide an efficient percolating network (i.e. high oxygen ion transport balanced by flux of electrons in the opposite direction) is an important factor. The main challenges for dual phase membranes lie in the chemical compatibility and the uniform mixing of the two phases (Vernoux '13, Zhu '12). Most of the research in this area therefore focuses on the development of suitable electronic and ionic conducting phases and new membrane preparation techniques.

### 2.3.2. Ionic Conductors

Materials for which the ionic conductivity,  $\sigma_{\text{ion}}$ , is more than 2 orders of magnitude larger than the electronic conductivity,  $\sigma_e$ , are characterized as purely ionic conductors. Fluorite-type oxides are the most common ionic conducting materials used in applications such as SOFC and heterogeneous catalysis. The crystal structure of fluorite is  $\text{AO}_2$ , where A is a tetravalent cation (Figure 9). The most widely used and intensively studied compositions are solid solutions of the type  $\text{AO}_2\text{-A}'\text{O}$  or  $\text{AO}_2\text{-A}''\text{O}_3$ , with A' and A'' being lower than A valent cations as shown in Figure 9, e.g., A = Zr, Ce, Th; A' = Ca, Sr, Ba; A'' = Sc, Y, or lanthanides (Vernoux '13). Even though pure thoria and ceria have fluorite structure which is stable from room temperature up to their melting points, zirconia has a number of polymorphs stable in different temperature ranges.

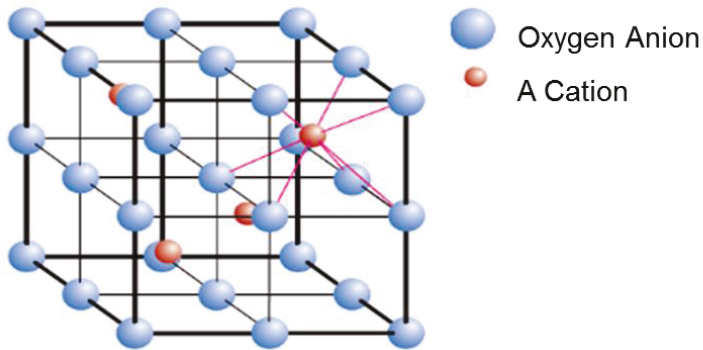


**Figure 9 Fluorite type Crystal Structure. Reprinted from (Skinner '03) with permission of Elseviers.**

The ionic conductivity of these oxides, particularly of  $\text{ZrO}_2$ ,  $\text{ThO}_2$  and  $\text{CeO}_2$ , is greatly enhanced when doped with lanthanides or alkaline earth metal compounds and is due to the creation of excess oxygen vacancies.  $\text{Bi}_2\text{O}_3$  doped metal oxides are another significant class of ionic conductors with high conductivity in comparison to doped  $\text{ZrO}_2$ ,  $\text{ThO}_2$  and  $\text{CeO}_2$  (P. J. Gellings '97). But most bismuth oxide materials have extremely poor strength and tend to reduce in low partial pressure atmosphere making them unsuitable for the intended power plant and industrial applications (Kharton '04, McGrath '01). Figure 10 compares the ionic conductivity of  $(\text{ZrO}_2)_{0.92}(\text{Y}_2\text{O}_3)_{0.08}$  (YSZ);  $\text{Ce}_{0.8}\text{Gd}_{0.2}\text{O}_{1.9}$  (CGO);  $\text{La}_{0.9}\text{Sr}_{0.1}\text{Ga}_{0.8}\text{Mg}_{0.2}\text{O}_2$  (LSGM);  $\text{La}_2\text{Mo}_2\text{O}_{9.64}$  (LAMOx); Si-apatite,  $\text{La}_{10}(\text{SiO}_4)_6\text{O}_3$ ; and Ge-apatite,  $\text{La}_{10}(\text{GeO}_4)_6\text{O}_3$ . Among these materials,

doped ceria (CGO) is one of the fast oxide ion conductors, in spite of being an electronic conductor at high temperatures in reducing atmosphere. CGO has significant advantages over conventional YSZ such as higher ionic conduction at low temperature ( $T < 600\text{ }^\circ\text{C}$ ) and better chemical compatibility with high flux perovskite materials. The degree to which CGO is a mixed ionic and electronic conductor (MIEC) depends on the doping level, temperature and oxygen activity (Dalslet '06).

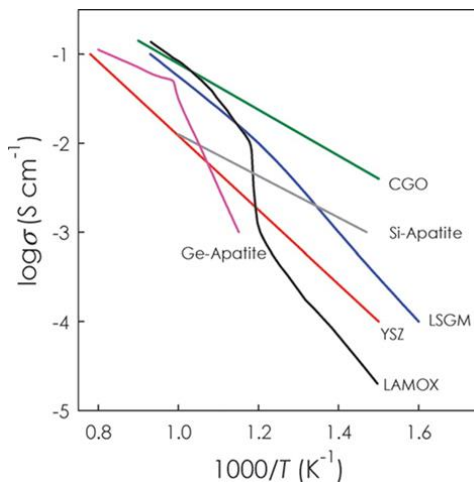


**Figure 10 Ionic conductivity of several anionic conductors as a function of inverse temperature. Reprinted from (Vernoux '13) with permission of American Chemical Society.**

In case of CGO, vacancies are created by the partial substitution of  $\text{Ce}^{4+}$  with  $\text{Gd}^{3+}$  creating vacancy contributing to ionic charge carriers and also when oxide ions interact with the gas phase oxygen at the surfaces (Mogensen '00, Steele '00, Wang '00). Thus CGO is the most commonly opted ionic conductor for OTMs.

### 2.3.3. Electronic Conductors

#### Spinel

In ceramic science and technology, the first idea brought to mind by the word “spinel” is a refractory material with high resistance to neutron irradiation. In this sense, spinel sounds similar to an electrical insulator. But some spinel structures also demonstrate high and controlled  $n$ -type

## 2 Fundamentals

electronic conductivity (Kawazoe '99, N F Mott '95). Mixed transition metal oxides with spinel structure represent an important family of materials showing good electronic conductivity. Oxide spinels are mostly described by the general formula  $AB_2O_4$ , where A and B are tetrahedral and octahedral cation sites in a cubic close packing of oxygen (Figure 11). The cation octahedral and tetrahedral site preferences as well as the equilibrium of temperature and partial pressure in the surrounding gas phase have a strong influence on the cation arrangement.

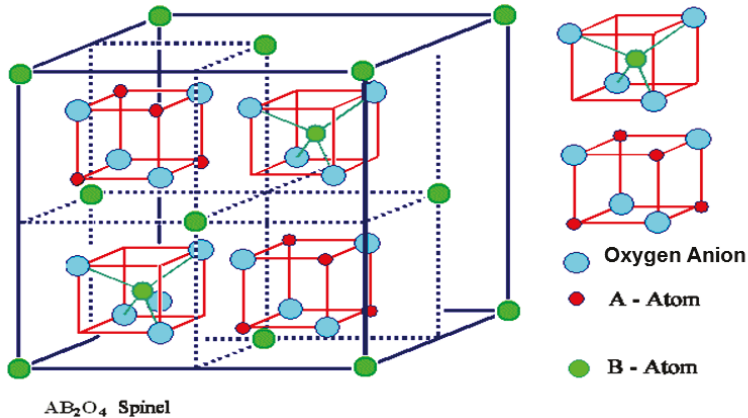


**Figure 11 Spinel crystal structure ( $AB_2O_4$ ) (Reprinted from Defects in Crystals © Prof. Dr. Helmut Föll, University of Kiel, (tf.uni-kiel.de))**

This equilibrium permits diffusion between a solid metallic oxide and oxygen present. However change in the partial pressure of oxygen, leads to deviation from the ideal composition depending upon the valence properties of the cations. By loss of oxygen from the ideal crystal, an oxide is formed with an excess of metal atoms. The excess electrons are trapped in the neighborhood of an interstitial cation or of a vacant anion site. According to the band theory of solids, such supernumerary metal atoms constitute filled impurity levels in the energy scheme of the crystal lattice, the distribution of electrons between the impurity levels and the conduction band being governed by a Boltzmann distribution. The conductivity of oxides at high temperatures thus depends upon the oxygen pressure in a manner which reflects the mechanism of conduction (Bevan '48, Verwey '47). For simple oxides such as ferric oxide, the dependence of conductivity upon diffusion of cations through the crystal lattice is observed only at temperatures above 720 °C, but some double oxides, e.g., cobaltite spinels, such as  $FeCo_2O_3$ ,

$\text{MnCo}_2\text{O}_3$  described as amphoteric conductors by Schottky, have impurity conduction under all conditions (Dali '99, Ferreira '03, Pelton '79). Inserting iron into  $\text{Co}_3\text{O}_4$  causes a substantial disorder modifying the properties and activity of the spinel. This double oxide spinel has electrical conductivity via the hopping of both electrons and holes present in the octahedral sites that are attributed to the contribution of both iron and cobalt cations respectively. The hole hopping conduction is predominant at low temperature, whereas electron hopping with a relatively higher mobility, dominates at high temperature. The insertion of iron into the normal spinel of cobalt oxide improves the thermal stability and substantially increases the stability under reducing atmospheres (Bahlawane '09, Cartaxo '07, Sharma '08).

### **Perovskites**

The main role of perovskite materials in dual-phase membranes is to provide high electronic conductivity, therefore, the amount of alkaline earth metals and unstable transition metals in this material can be greatly reduced, resulting in a high thermal and chemical stability for the dual-phase membrane (Dong '11). Manganite type perovskite ( $\text{Ln,A}$ )-  $\text{MnO}_{3\pm\delta}$  ( $\text{Ln} = \text{La-Yb}$  or  $\text{Y}$ ;  $\text{A} = \text{Ca, Sr, Ba, Pb}$ ) exhibit predominant electronic conductivity in combination with low oxygen ion diffusivity; Their transport properties and electrochemical activity are strongly dependent on the oxygen non-stoichiometry (Al Daroukh '03). In addition to this perovskite, MIEC perovskites such as LSCF, doped  $\text{SrTiO}_3$  can also be combined with pure ionic conductors to form the dual phase membranes.

### **$\text{K}_2\text{NiF}_4$ Materials**

There has been increasing interest in alternative types of mixed conductors. Of most interest has been the development of the perovskite related oxides of the  $\text{K}_2\text{NiF}_4$  ( $\text{A}_2\text{BO}_{4+\delta}$ ) structure shown in Figure 12. In this structure there are layers of  $\text{ABO}_3$  separated by  $\text{AO}$  layers. It is this layered structure that is of interest as it allows great flexibility in the oxygen stoichiometry of these materials (Rice '93). Indeed, it is possible to incorporate excess oxygen in the interstitial species and this provides an attractive alternative to the vacancy-based conduction mechanism present in the perovskite and fluorite oxides, where the dopant-vacancy interactions can limit the observed conductivity (Shaula '13). This high concentration of oxygen interstitials offer the possibility of rapid oxygen transport through the ceramic material but high anisotropy is a growing concern as it would limit the charge carrier movement based on the orientation hence significant efforts

## 2 Fundamentals

have been directed towards the understanding of the mechanism and anisotropy of conduction in the  $K_2NiF_4$ -type oxides. Other important compositional families are  $LnBaCo_2O_{5+\delta}$  ( $Ln = Pr, Gd-Ho, Y$ ),  $LnBaCo_4O_{7+\delta}$  ( $Ln = Dy-Yb, Y$ ), nickelates and cuprates family with prominent mixed conductivity (Skinner '03).

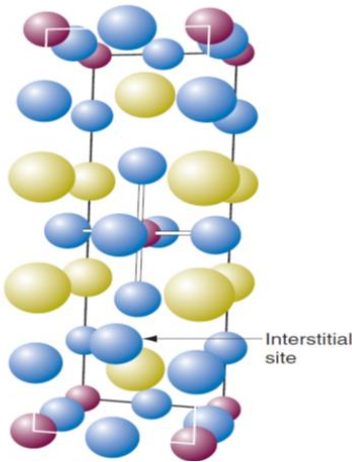


**Figure 12 Representation of  $A_2BO_{4+\delta}$  structure, where the red spheres represent B-cations, the blue spheres represent oxygen ions, and the yellow spheres represent A-cations. An interstitial oxygen ion is also shown. Reprinted from (Skinner '03) with permission of Elseviers.**

Summarizing all the materials that were discussed in the last three sub-sections of material selection, the conductivity values of several materials are compared in Figure 13. The ionic conductivity and electronic conductivity of materials belonging to different groups between temperatures 900 °C - 1000 °C are plotted together. Strategically, an electronic or MIEC material with electronic conductivity between the range of 5 to 10 S/cm would be sufficient as the ionic conductivity of most common ionic conductors is almost one order of magnitude lower in this temperature range.

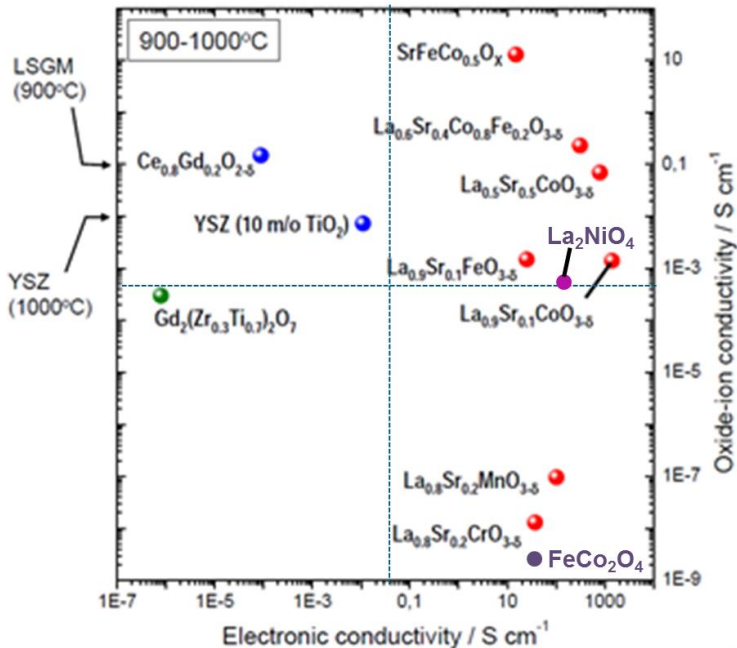


Figure 13 Ionic and electronic conductivity of several materials for the temperature range of 900-1000 °C are plotted (Schrüder '08).

#### Pre-selection Material review

Thorough literature review was carried out on the possible class of material combinations to identify a promising dual phase composite membrane of research interest. Table 1 summarizes the various dual phase membranes and their performance that have been researched in the past. The material combinations were screened particularly focusing on the results close to the intended operating temperature (850 °C) of the dual phase membrane. Based on this database, composites for this research work were selected that are elaborated in the material investigation section 4.1 that led to the focus of one specific dual phase composite extensively investigated in this PhD thesis. More details regarding this phase composition will be described later. The oxygen flux of the chosen dual phase composite will be compared to the above list for evaluation of its performance and sufficient chemical stability at the operating temperature in the next chapter.

**Table 1 Literature summary of the dual phase membranes and their oxygen permeation values corresponding to limiting process parameters**

Compound	Thickness (mm)	Temperature (C)	O <sub>2</sub> Flux (mLcm <sup>-2</sup> min <sup>-1</sup> )	CO <sub>2</sub> Stability in h	Reference
Ce <sub>0.9</sub> Gd <sub>0.1</sub> O <sub>2-δ</sub> - Fe <sub>2</sub> O <sub>3</sub>	0.5	900	0.06	200	(Luo '11)
Ce <sub>0.9</sub> Gd <sub>0.1</sub> O <sub>2-δ</sub> - NiFe <sub>2</sub> O <sub>4</sub>	0.5	900	0.11		(Huixia '11)
Ce <sub>0.8</sub> Gd <sub>0.2</sub> O <sub>2-δ</sub> - NiFe <sub>2</sub> O <sub>4</sub>	0.68	1000	0.17	76	(Balaguer '13)
Ce <sub>0.8</sub> Gd <sub>0.2</sub> O <sub>2-δ</sub> - Ba <sub>0.5</sub> Sr <sub>0.5</sub> Co <sub>0.8</sub> Fe <sub>0.2</sub> O <sub>3-δ</sub>	0.5	900	0.26	700	(Xue '13)
Ce <sub>0.8</sub> Gd <sub>0.2</sub> O <sub>2-δ</sub> - La <sub>0.4</sub> Ba <sub>0.6</sub> Fe <sub>0.8</sub> Zn <sub>0.2</sub> O <sub>3-δ</sub>	0.9	950	0.84		(Sun '13)
Ce <sub>0.9</sub> Gd <sub>0.1</sub> O <sub>2-δ</sub> - La <sub>0.6</sub> Sr <sub>0.4</sub> Co <sub>0.2</sub> Fe <sub>0.8</sub> O <sub>3-δ</sub>	1	850	0.1		(Joo '13)
Ce <sub>0.8</sub> Gd <sub>0.2</sub> O <sub>1.9-</sub> La <sub>0.7</sub> Sr <sub>0.3</sub> MnO <sub>3</sub>	0.6	950	0.05		(Kharton '01)
Ce <sub>0.9</sub> Pr <sub>0.1</sub> O <sub>2-δ</sub> - Mn <sub>1.5</sub> Co <sub>1.5</sub> O <sub>4-δ</sub>	0.5	900	0.1	250	(Luo '12)
Ce <sub>0.9</sub> Pr <sub>0.1</sub> O <sub>2-δ</sub> - Pr <sub>0.6</sub> Sr <sub>0.4</sub> FeO <sub>3-δ</sub>	0.6	950	0.27	150	(Luo '12)
Ce <sub>0.8</sub> Sm <sub>0.2</sub> O <sub>1.9-</sub> Sm <sub>0.5</sub> Sr <sub>0.5</sub> CoO <sub>3-δ</sub>	0.6	850	0.2		(Li '11)
Ce <sub>0.8</sub> Sm <sub>0.2</sub> O <sub>1.9-</sub> La <sub>0.9</sub> Sr <sub>0.1</sub> FeO <sub>3</sub>	0.6	900	0.1	450	(Wang '13)
Ce <sub>0.85</sub> Sm <sub>0.15</sub> O <sub>1.925-</sub> Ce <sub>0.85</sub> Sm <sub>0.15</sub> O <sub>1.925</sub> /Sm <sub>0.6</sub> Sr <sub>0.4</sub> Al <sub>0.3</sub> Fe <sub>0.7</sub> O <sub>3-δ</sub>	0.8	950	0.43		(Li '13)
Ce <sub>0.8</sub> Sm <sub>0.2</sub> O <sub>1.9-</sub> Sm <sub>0.6</sub> Ca <sub>0.4</sub> CoO <sub>3</sub>	0.5	900	0.14	100	(Li '13)
Ce <sub>0.8</sub> Sm <sub>0.2</sub> O <sub>1.9-</sub> Sm <sub>0.8</sub> Mn <sub>0.5</sub> Co <sub>0.5</sub> O <sub>3</sub>	0.5	850	0.25	500	(Zhu '12)
Yr <sub>0.2</sub> Zr <sub>0.8</sub> O <sub>2-δ</sub> - La <sub>0.8</sub> Sr <sub>0.2</sub> Cr <sub>0.5</sub> Fe <sub>0.5</sub> O <sub>3-δ</sub>	1	900	0.05	500	(Fang '13)

### 3. Experimental Methods

#### 3.1. Membrane Fabrication

##### Pechini synthesis

Starting powders of the dual phase composite were synthesized by the modified one pot method (aka) Pechini process. The Pechini route presents some advantages such as obtaining carbonate-free, chemically homogeneous final oxide compounds with a high relative density and small particle size that reduces the sintering temperature required for gas tight pellets. It is a sol-gel technique that involves the production of an amorphous-like gel containing a metal complex from their nitrates. Citric acid is used as chelating agent that prevents partial segregation of metal components (Cousin '90, Pechini '67). Ethylene glycol is added to the reaction batch to promote the polymerization with chelating agent and produce an organometallic polymer (Tietz '01).

The Pechini synthesis method is shown in the flow chart (Figure 14) where A, B and C denote the nitrates of the individual compounds required to form the desired dual phase composite. For e.g. Table 2 indicates the amount of nitrates of Ce, Gd, Fe and Co dissolved in deionized water to prepare an aqueous solution for Pechini synthesis of CGO-FCO powder. This aqueous solution is continuously stirred while citric acid and ethylene glycol are added to obtain a homogeneous solution.

**Table 2 Nitrates of individual compounds mixed with citric acid and ethylene glycol to obtain 50 g of  $Ce_{0.8}Gd_{0.2}O_{2.8}$  -  $FeCo_2O_4$  (CGO-FCO) composite in 60:40 wt% proportion by Pechini process.**

$Ce(NO_3)_3 \cdot 6H_2O$ (Alfa Aesar, 99.5%)	$Gd(NO_3)_3 \cdot 6H_2O$ (Alfa Aesar, 99.99%)	$Fe(NO_3)_3 \cdot 9H_2O$ (Merck, 99.999%)	$Co(NO_3)_3 \cdot 6H_2O$ (Merck, 99%)	Citric acid (Merck, 99.5%)	Ethylene glycol (Merck)
59.91 g	15.57 g	33.99 g	48.97 g	178.57 g	105.49 g

The homogenous solution undergoes a sequence of polymerization, gelation, drying and pre-calcination steps to form a charred powder of the composite. Finally, thermal decomposition of the complex to form the structural phases is carried out by calcination of the synthesized powder at 700 °C for 15 h. This is followed by milling of powder in a planetary ball mill for 48 h at 175

### 3 Experimental Methods

rpm to eliminate any agglomerates and achieve fine homogenous particle distribution of the composite. Thus,  $Ce_{0.8}Gd_{0.2}O_{2-\delta}$  -  $FeCo_2O_4$  (CGO-FCO) composite powder is synthesized by Pechini process.

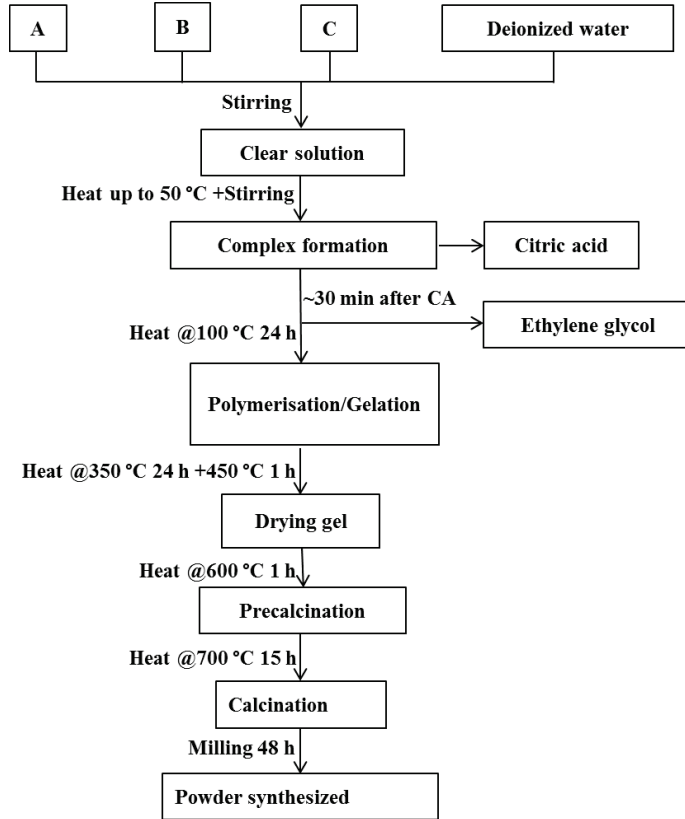


**Figure 14** Flow chart of powder synthesis by Pechini process

#### **Solid state reaction + reactive sintering (“SSR”)**

The solid state reaction is the most common synthesis process to produce conventional ceramic powders. The method involves ball mill mixing of the precursor oxides on a micrometer level, carbonates, hydroxides or salts dispersed in solvent, which reduces and homogenizes the particle size (Cousin '90). After the milling, the powder is separated from the zirconia balls and dried. Then, the dried powder is subjected to reactive sintering at temperatures of at least two thirds of its melting point for a period of time to obtain the dense composite with intended phase.

In this work, 100 g of 85:15 wt% CGO-FCO was synthesized by conventional solid state reaction. 85 g of commercially available  $\text{Ce}_{0.8}\text{Gd}_{0.2}\text{O}_{1.9}$  (CGO) (Treibacher Industrie AG, 99%), 10.12 g of  $\text{Co}_3\text{O}_4$  (Merck, 99%) and 5.06 g of  $\text{Fe}_2\text{O}_4$  (Merck, 99%) were mixed and milled in a planetary ball mill for 24 h at 175 rpm to obtain CGO-FCO.

### Spray Pyrolysis (SP)

Spray pyrolysis or spray drying is a process in which a thin film of powder is deposited by spraying an aqueous nitrate solutions on a heated surface, where the constituents react to form the desired chemical compound (Mooney '82). The spray dried powder is then subjected to calcination at different temperatures to form the crystalline phase solid powder. The process is particularly useful for the deposition of oxides. Flow chart of the spray drying method is shown in Figure 15.

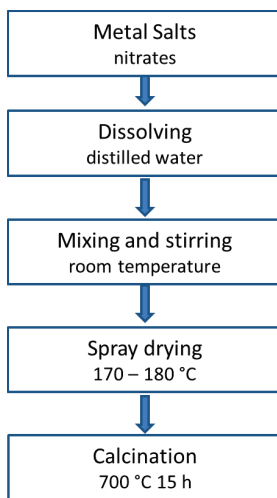


**Figure 15** Flow chart of spray drying process (Kountouros '95).

CGO-FCO powder is synthesized by preparing an aqueous solution of  $\text{Ce}(\text{NO}_3)_3 \cdot 6\text{H}_2\text{O}$ ,  $\text{Gd}(\text{NO}_3)_3 \cdot 6\text{H}_2\text{O}$  (Alfa Aesar, Germany),  $\text{Fe}(\text{NO}_3)_3 \cdot 9\text{H}_2\text{O}$  and  $\text{Co}(\text{NO}_3)_3 \cdot 6\text{H}_2\text{O}$  (Merck, Germany) dissolved in distilled water. The mixture was stirred to form a homogenous solution, which was then passed through the spraying nozzle in to the drying chamber. Spray drying was performed using GEA Niro A/S with inlet and outlet temperatures of about 300 °C and 180 °C respectively.

### 3 Experimental Methods

The ejected fine droplets are solidified in hot air from the air disperser. The spray dried powder is then calcined at 700 °C for 15 h to obtain the desired CGO-FCO composite.

#### **Uniaxial Pressing**

Bulk membranes are uniaxial pressed in the form of discs and bars using model PW10 (Fa. Paul Otto Weber GmbH, Remshalden). For oxygen flux measurements, discs are pressed out of 24 mm diameter dies from 1.25 g powder. Bars for electrical conductivity measurements are pressed from 3 g of powder in a die of dimension 5 x 0.5 x 0.5 cm<sup>3</sup>. Both discs and bars are uniaxial pressed at 80 MPa for 90 seconds to obtain green dense pellets. The pellets are subjected to conventional sintering process at 1200 °C for 10 h with heating and cooling rate of ±3 k/min. The sintered dense disc samples are usually 18 mm diameter and 1 mm thickness. The sintered samples are polished to 1 mm thickness with a P4000 SiC emery paper surface finish. The samples are also subjected to grinding to obtain a 14.6 mm diameter sample to fit in the permeation set up for oxygen flux measurements.

#### **Hot pressing**

Hot pressing is a high-pressure, low-strain-rate powder metallurgy process for forming of a powder or powder compact at a temperature high enough to induce sintering and creep processes. This is achieved by the simultaneous application of heat and pressure. The loose powder or the pre-compacted part is in most of the cases filled in to a graphite mold that allows induction or resistance heating up to temperatures of typically 2,400 °C (4,350 °F). Pressures of up to 50 MPa (7,300 psi) can be applied (German '05, Taylor '33).

Hot pressing experiments were carried out in Vacuum hot press HPW 100/150 (FCT Systeme GmbH, Rauenstein, Germany) with the use of graphite die at 50 MPa, up to 1200°C for 1 hr under Ar atmosphere. Graphite dies with 13 mm and 18 mm diameters were used for pre-pressed and pre-sintered samples.

#### **Field-assisted sintering technique/Spark plasma sintering (FAST/SPS)**

FAST/SPS is a low voltage, direct current (DC) activated, pressure-assisted sintering and synthesis technique. Optionally, the DC current can be pulsed. This method can indeed be used to synthesize new compounds and/or to densify materials in one step (Schwarz '13). FAST/SPS is similar to hot pressing (HP), but the way the heat is produced and transmitted to the sintering

material is different. If the green body is electrically conductive, energy is dissipated directly within the sample and the electrically conductive parts of the pressing tool. Otherwise, an electrically conductive tool must be used and the heat produced by Joule heating is transmitted by conduction to the powder (Guillon '14).

CGO-FCO Pre-pressed pellet of 13 mm diameter was subjected to FAST using SPS furnace type HP D5 (FCT Systeme GmbH, Rauenstein, Germany) at 900° C. The other parameters include use of 13 mm diameter graphite die in Vacuum+ Argon atmosphere, 5 min dwell time and 100 K/min ramp rate with 50 MPa pressure.

#### **Pulsed Laser Deposition (PLD)**

Pulsed laser deposition is a physical vapor deposition technique where a high-power pulsed laser beam is focused inside a vacuum chamber to strike a target of the material that is to be deposited. This material is vaporized from the target (in a plasma plume) which deposits it as a thin film on a substrate (such as a silicon wafer facing the target). This process can occur in ultra high vacuum or in the presence of a background gas, such as oxygen which is commonly used when depositing oxides to fully oxygenate the deposited films ('94, Ferguson '09, Ohnishi '08).

Dr. Alexander Opitz research group (Institute of Chemical Technologies and Analytics Research Division Electrochemistry, TU Wien, Head Prof. Jürgen Fleig ) assisted by PLD coating FCO thin layers on CGO substrates. The FCO target is ablated by a Lambda COMPexPro 201 KrF excimer laser (248 nm; 5 Hz repeat rate). The substrate temperature is around 650 °C (controlled by a pyrometer); background pressure of pure oxygen in the chamber is  $4 \times 10^{-2}$  mbar, and deposition time of ca. 25 min to obtain a film thickness of about 100 nm.

#### **Screen printing**

Screen printing is a simple coating technique used in several different applications. In this thesis work, it has been used to coat porous catalytic layer over the dense membrane to overcome surface exchange limitations in oxygen transport. Screen printing involves squeezing a viscous paste through a sieve over the dense membrane layer. The thickness of the layer is controlled by the mesh size of the sieve. Manual screen printing device was used in this work, Terpeneol (FLUKA) or BCA (2-(2-Butoxyethoxy) ethyl acetate as the solvent, ethylcellulose or Mowital

### 3 Experimental Methods

SB 20H as the binder and NUOSPERSE FX 9086 (Fa. Elementis Specialties Inc., Cologne) as the dispersant were mixed with LSCF powder in a three roll mill EXAKT 80E. The milling process removes agglomerates and homogenizes the paste for the printing process.

A porous catalytic layer of LSCF screen printed over the dense dual phase membrane surface. The screen printed LSCF layer ( $\sim 20 \mu\text{m}$ ) was dried at  $80 \text{ }^\circ\text{C}$  and co-fired with the membrane at  $1080 \text{ }^\circ\text{C}$  for 3 h to obtain a porous LSCF catalytic layer of  $\sim 10 \mu\text{m}$ .

#### **Tape casting**

Tape casting is a method used for the fabrication of thin ceramic sheets. The process involves a moving doctor blade that limits the thickness of ceramic slurry with a resin binder being coated over a belt. After drying, This thin film is strong enough to be stripped off, cut or punched out into desired shape and fired (Howatt '47, R. E. Mistler '00). The basic schematic of the tape casting process is shown in Figure 16.

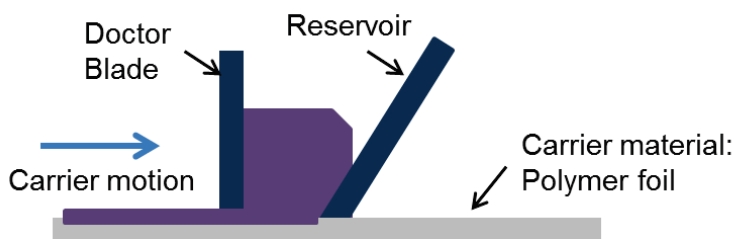


**Figure 16 The schematic of a typical tape casting process**

The ceramic slurry is highly specialized with several additives to provide the necessary formulation and handling. For this process tailored raw materials are necessary which ensure a stable dispersion in the slurry. Most important parameter for a successful slurry development is particle size and specific surface area of the ceramic powders. To get the desired surface area of around  $1\text{-}5 \text{ m}^2/\text{g}$  and to avoid sedimentation of the powder particles, the particle size should be in the range of  $1\text{-}2 \mu\text{m}$  (dependent on the materials density) with a compact grain morphology (given based on IEK-1 in-house experience from development of BSCF and LSCF asymmetric membranes by tape casting). The additives include solvents 34 m% Ethanol and 66 m% Methyl ethyl ketone (MEK) that homogenize the solvent concentration throughout the tape during drying. Next additive is the dispersant (NUOSPERSE FX 9086 or TEGO DISPERS 655 (Fa.

Elementis Specialties Inc., Cologne)) that acts as the wetting agent. Polyvinylbutyral (PVB-98) (Fa. Solutia Inc.) is the binder that provides the polymer matrix network to hold the entire chemical system together. Plasticizer is another additive included in the slurry system to provide the needed flexibility of the tape. Solusolv S-2075 (Fa. Solutia Inc.) and PEG400 are the two types of plasticizers used for this purpose. Finally rice starch (Remy FG – Firma Remy) as pore former is added only to support slurry for obtaining the necessary porosity in the support layer.

In this work, tape casting process is selected for scaling of the dual phase composite membrane fabrication. Tape cast slurry is prepared by mixing the powder with the additives mentioned above along with 1:0.5 ratio of powder to zirconia milling balls (size = 5 mm) in tumble mixer. The optimized slurry recipe for both membrane and support are shown in Table 3, the complete process of slurry optimization is explained in detail in the section 4.3.3. The step by step details of slurry preparation and tape casting process are described in the flow chart shown in Figure 17. The tape casting is carried out using Fa. Johann Fischer, Aschaffenburg, with movable casting stand and fixed polymer film. The movable casting stand is set at a constant speed of 250 mm/min. The slurry is flowed into the movable casting stand which contains the doctor blade that limits the thickness of the cast. The cast layers are dried and punched out into desired shapes and sizes for sintering.

**Table 3 Optimized recipe for 100 g of CGO-FCO powder into tape casting slurry for both membrane and support layers.**

Tape	Powder (g)	Solvent (g)	Dispersant (g)	Binder (g)	Plasticizer 1 (g)	Plasticizer 2 (g)	Pore former (g)
Membrane	100	45.7	3	7	6	7	
Support	100	45.7	3	7	6	7	30

### 3 Experimental Methods

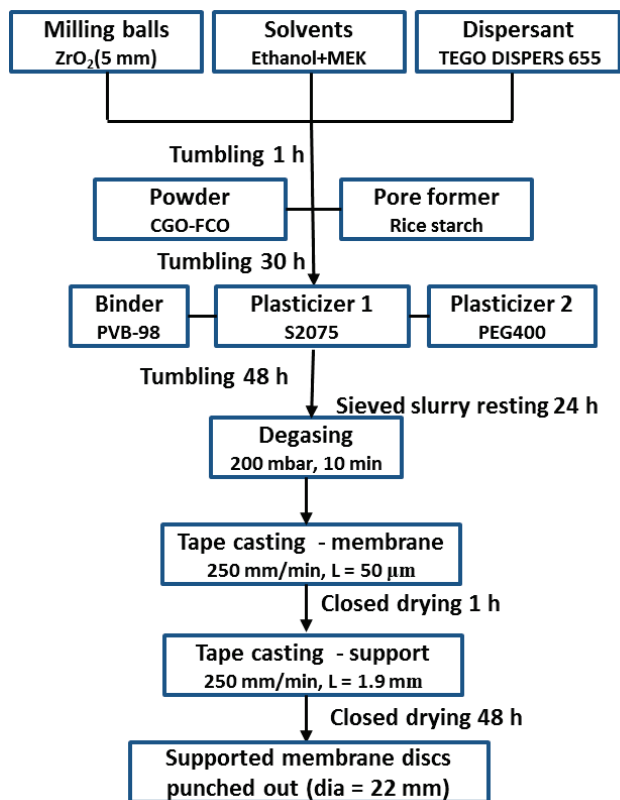


Figure 17 Flow chart of step by step procedure to make the tape casting slurry for CGO-FCO membrane and porous support.

## 3.2. Membrane Characterization

### Particle Size Distribution (PSD)

The particle size distribution of the powder was determined by particle analyser HORIBA LA-950. The LA-950 uses a static laser light scattering that interacts with the particles to provide the light scattering patterns which are characterized into the particle size of the batch. The equipment can measure over a range of 0.01  $\mu\text{m}$  -3000  $\mu\text{m}$ .

### BET

Brunauer–Emmett–Teller (BET) theory aims to explain the physical absorption of gas molecules on a solid surface and serve as basis for the measurement of the specific surface area of a material.(Brunauer '38) The measurements were carried out using AREAMETER-Jung Instruments GmbH based on the BET single-point method by low-temperature N<sub>2</sub> adsorption (equilibrium method) on the basis of DIN 66132.

### ICP-OES

The stoichiometry of the materials was quantified by inductively coupled plasma optical emission spectroscopy (ICP-OES). ICP-OES measurements were carried using the Thermo Scientific iCAP7600 spectrometer with optical scale and CID semi-conductor detector, axial and radial reflection, and wavelengths between 166 nm and 847 nm. This chemical composition analysis was carried out at Zentralinstitut für Engineering, Elektronik und Analytik (ZEA-3). 100 mg of powder was dissolved in 30 mL HCl (5 %) and filled to 50 mL volume. This solution was injected through the plasma, and the subsequent emission of light with certain frequency is proportional to the concentration of elements in the sample measured by an emission spectrometer. Thus, the weight percent of each element in the analyzed sample is obtained from these measurements.

### Dilatometer

Dilatometer is used to determine the Thermal Expansion Coefficient (TEC) of a material. In case of dual phase membrane selection, TEC match between the two phases plays an important role in choosing the suitable combinations. The measure of dimensional change  $\Delta L$  from the reference length  $L_0$  of the sample as a function of temperature is used to determine the thermal expansion coefficient (TEC) given by:

### 3 Experimental Methods

$$\text{TEC} = \frac{\Delta L}{L_0 \Delta T} \quad (15)$$

From the dilatometer measurement, the slope of  $\frac{\Delta L}{L_0}$  versus the temperature plot gives the TEC value (Maca '08). The sintering behavior of the material can also be determined using the dilatometer, since during sintering the shrinkage of the sample is calculated as the % of the dimensional change  $\Delta L$  with respect to the reference length of the hand pressed pellet as a function of temperature. The uniaxial pressed cylindrical pellet is subjected to the sintering temperature for a dwell time and the corresponding shrinkage data  $\frac{\Delta L}{L_0}$  is obtained in %. The dilatometer experiments were carried out with a Dilatometer 402C and 402E from Netzsch.

#### **Thermo-gravimetry/Differential Thermal Analysis (TG/DTA)**

Chemical and thermal stability of materials can be studied by TG technique, which is commonly used to investigate decomposition, dehydration, oxidation/reduction reactions, the purity and the presence of humidity in a sample accompanied by a mass change (Haines '98). The TG device registers the mass changes undergone by the sample as a function of temperature, time and atmosphere. The TG is combined with DTA, which records exothermic (downwards peak) or endothermic (upwards peak) processes that enclose transformations in the material when compared with an inert reference material. DTA is mainly used for studying phase transitions, chemical reactions, adsorption, crystallization and melting.

In this work, the TG/DTA analysis was carried out with the calorimeter STA449 F1 Jupiter coupled to the mass spectrometer QMS 403C Aëolos from the company Netzsch. The powders were analyzed in air atmosphere in the temperature range from room temperature to 1200 °C, with heating and cooling rates of 5 °C/min.

#### **Gravimetric (Buoyancy) Method of Density Determination**

The relationships between the mass, the volume and the density of solid bodies immersed in liquid as described by Archimedes form a basis for the determination of the density of substances. The apparent weight of a body in a liquid, i.e., the weight as reduced by the buoyancy force is measured. This value is used in combination with the weight in air to calculate the density (Density Determination Manual\_Sartorius).

$$\rho_s = \rho_{th} \left\{ \frac{m_{air}}{m_{air} - m_{eth}} \right\} \quad (16)$$

Where  $\rho_s$  is the relative density of the sample measured,  $\rho_{th}$  is the theoretical density of the composite calculated based on the volume of the composite.  $m_{air}$  and  $m_{eth}$  are the measured mass of the sample in air and ethanol in room temperature, used to calculate the density using equation 16.

### X-ray Diffraction (XRD)

X-ray diffraction (XRD) is a non-destructive technique that allows the identification of the crystalline phases and orientation of crystalline materials, their lattice parameters ( $10^{-4}$  Å), strain, crystallite size and thermal expansion, which define the fingerprint of the substance. XRD measurements are based on the physical principle that a monochromatic X-ray beam with a wavelength  $\lambda$  comes in contact with the crystalline material at a particular angle. The diffraction is produced only when the distance traveled by the reflected X-rays from successive planes differs by a complete number of wavelengths (Compton '23).

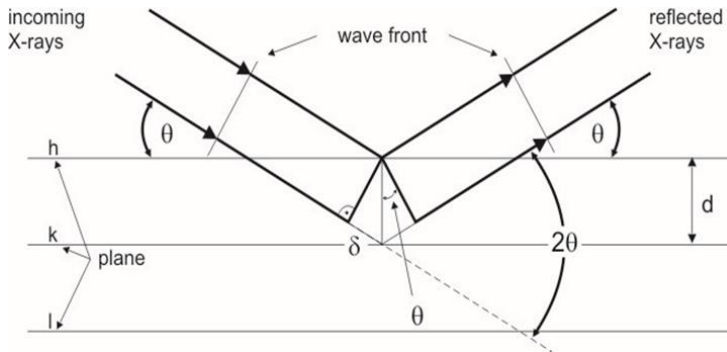


**Figure 18 Scheme of the diffraction geometry on a crystalline materia l (ChemUCDavisWeblink , Uni\_GottingenPhysikWeblink).**

As shown in Figure 18, the diffracted angle from the family of crystallographic planes ( $h k l$ ) has a value of  $2\theta$ , which is employed to determine the distance between layers of atoms in a sample using the Bragg's law:

$$n\lambda = 2d_{hkl} \sin \theta \quad (17)$$

where  $d$  is the  $h k l$  inter-planar spacing (nm),  $\theta$  is the angle of incidence of X-rays (rad),  $\lambda$  is the wavelength of X-rays (m); and  $n$  is an integer representing the reflection order. By combining the

### 3 Experimental Methods

Bragg condition with the plane spacing for a system, it is feasible to directly obtain the positions of atoms in the unit cell. For example, in a cubic system the diffraction peaks satisfy the following equation:

$$\frac{\sin \theta}{h^2+k^2+l^2} = \frac{\lambda^2}{4a^2} \quad (18)$$

where  $a$  is the cell parameter and  $h$ ,  $k$ , and  $l$  are the Miller indices defining the plane (Bragg '12, Miao '99, Sir '21). The phases of the composites as synthesized powders and sintered pellets were analysed by X-ray diffraction (XRD). The X-ray analyses were carried out with the diffractometer D4 ENDEAVOR from the company Bruker. A standard measurement programme was used; the parameters of this programme were the range of diffraction angle  $2\theta$  from  $10^\circ$  to  $80^\circ$ , increments of  $0.02^\circ$  for  $2\theta$  and 0.75 second of measurement time per step. The data were analysed with the programme package X'Pert HighScore (PANalytical B.V., version 3.0.5).

In this work, the lattice parameters and phase quantification of the membranes were determined using the Rietveld method. The XRD patterns can be described as the combination of a smooth curve consisting of Gaussian peaks (sometimes overlapping or superimposed) on top of a smooth background and the Rietveld refinement consists of a complex curve fitting program to separate out the peaks and identify the corresponding phase with more accuracy (Rietveld '69).

X-ray diffraction analysis of FCO thin films PLD coated on CGO substrates were carried out on a PANalytical Empyrean diffractometer with  $\text{CuK}\alpha$  radiation (@ TU Wien). XRD measurements were conducted with  $2^\circ$  incident angle and diffraction pattern was recorded at  $15^\circ \leq 2\theta \leq 90^\circ$ . Data analysis was performed with the software Highscore Plus in combination with ICDD powder diffraction database (PDF4+) (Kabekkodu '10).

#### **Scanning electron microscopy (SEM)**

In a typical SEM, focused beam of electrons interact with atoms of the sample to provide compositional and surface topographical details in the form of images. An SEM allows for high-resolution imaging of surfaces by using high-energy electrons (1.5-20 KeV) generated by a heated tungsten filament. The SEM has a magnification up to  $10^6 \times$  and great depth of field. For that purpose, an incident beam of monochromatic electrons causes a secondary emission across the sample surface, which is collected to form an image of the surface. The quality and contrast obtained in the image depends mainly on the conductivity and surface topography of the sample

(McMullan '95). By detecting different emissions of the sample, it is possible to obtain diverse contrast images, *i.e.*, backscattered electrons (BSE), Auger electrons (AES) and Energy dispersive x-ray spectroscopy (EDS). BSE causes different contrast subjected to the atomic number,  $Z$ , of the elements, so changes in composition can be distinguished; EDS is a qualitative and quantitative chemical microanalysis technique to characterize the elemental composition of the volume analyzed. It is performed in conjunction with an SEM, but uses the X-rays that are emitted from the sample due to the electron beam. The combination of SEM with EDS allows the analysis of the sample morphology and the composition of the different phases that are present. The minimum detection limits are about 0.1 weight percent, depending on the element and matrix (Williams '05). Conducting materials that allow the transport of the incident beam electrons do not need any handling of the sample. However, for poor conductors or insulators, a conducting layer that does not modify the topography needs to be added. This is achieved by coating the sample in vacuum with gold or platinum (for EDS) using a sputter coater. The SEM pictures were taken with a Zeiss Ultra 55 and a Zeiss Supra 50 VP<sup>1</sup> (Carl Zeiss NTS GmbH, German). The electronic conductivity of the samples was enhanced by sputter deposition of a thin platinum layer prior to the analysis. HITACHI S4800 SEM at ORNL was also used for the analysis of the stability tested samples.

### **Transmission Electron Microscopy (TEM)**

Transmission Electron Microscopy (TEM) utilizes energetic electrons to provide morphological, compositional and crystallographic information on samples. The beam of electrons is transmitted through an ultra-thin specimen ( $< 200$  nm), interacting with it as the beam passes through. The electrons that are not absorbed by the sample are detected forming a two dimensional image, which is magnified and focused onto an imaging device (Ruska '87). Two different TEM sources were used for the investigation of the dual phase membranes as listed below; Scanning transmission electron microscopy high angle annular dark field (STEM-HAADF) imaging and electron energy loss spectroscopy (EELS) was performed by using  $C_s$  probe corrected FEI-Titan 80–300 operating at 300 kV. Electron-transparent specimens were prepared from as-sintered pellets using the traditional approach which includes ultrasonic drilling, mechanical polishing and  $Ar^+$  ion milling at 5 keV. The scanning transmission electron microscopy (STEM) images

---

### 3 Experimental Methods

were acquired using Zeiss Libra 200FE equipped with a cold FEG source operated at 200 KV, HAADF detector from Fischione and X-Flash EDS detector from Bruker. ESPRIT software was used to analyze and build the EDS elemental maps. TEM lamellas were prepared by means of a FIB (Focused-Ion Beam).

#### **Time of Flight - Secondary Ion Mass Spectroscopy (ToF-SIMS)**

Secondary Ion Mass Spectroscopy is a surface analysis technique where the thin film is sputtered with a focused primary ion beam. The emitted secondary ions are accelerated into a mass spectrometer and their time of flight ( $t$ ) from the sample surface to the detector over a distance ( $L$ ) is given by

$$t = L \left( \frac{m}{2zV_{ac}} \right)^{1/2}, \quad (19)$$

where  $m/z$  is mass-to-charge ratio of the ions and  $V_{ac}$  is the accelerating voltage (Benninghoven '94, Williams '85). The SIMS method was used to identify the phase interaction and transformation encountered between the fluorite substrate and spinel thin film during the annealing process to form the third phase, an orthorhombic perovskite. The depth profile mode of analysis in ToF-SIMS is used to determine the distribution of difference chemical compounds as a function of depth from the surface. The depth profile of FCO coated CGO substrate to a penetration depth estimate of about 0.5  $\mu\text{m}$  (assuming 3  $\mu\text{m}$  per hour sputter rate) was carried out using ToF-SIMS 4 (IonTOF, Germany) with Cs ion beam for sputtering (2 KeV) and Bi gun (25KeV) for analysis.

### **3.3. Membrane Performance**

#### **Electrical conductivity**

The ambipolar conductivity can be calculated from the oxygen flux permeation measurements done experimentally. But in order to investigate whether ionic or electronic conductivity is the limiting factor on overall bulk diffusion rate of the dual phase compound, it is necessary to calculate the total conductivity of the compound as well. According to equation 20:

$$\sigma_{tot} = \sigma_i + \sigma_e \quad (20)$$

Electrical/total conductivity is the sum of ionic and electronic conductivity of a compound. In case of single phase MIEC or dual phase composite materials containing both ionic and

electronic conductivity, the calculated ambipolar conductivity and measured total conductivity can be assumed to represent the ionic and electronic conductivity of the materials. These values help understand the conductivity limitations on oxygen flux of OTMs irrespective of parameters such as  $T$ ,  $p_{O_2}$  and  $L$  (Czyperek '09, Sunarso '08). Electrical conductivity measurements are conducted by standard Four-point DC technique. Compared to two-point measurements, this configuration eliminates the influence of the contact resistance and wiring.

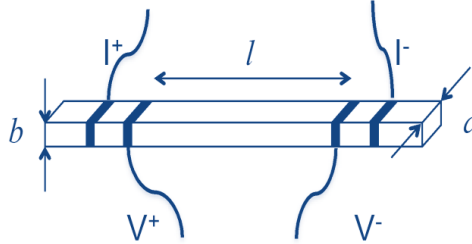


**Figure 19 Four point configuration for DC conductivity measurements (Ramírez '13).**

Rectangular bar sample configuration is used in DC-conductivity measurement. The sample preparation involves, uniaxial pressing of powders at 80 MPa for 2 minutes into rectangular probes ( $5 \times 0.5 \times 0.5 \text{ cm}^3$ ) and subsequently sintering at 1200 °C for 5 h in air atmosphere. The rectangular bars are then contacted using silver wire and paste, as shown in Figure 19. The measurements are carried out in a temperature range from 600 to 850 °C by heating and cooling down at 3 °C/min in atmospheric air in a tubular oven. The I-V slope provides the resistance imposed by the sample, from which the electrical conductivity ( $\sigma_{\text{tot}}$ ) is extracted by applying the Ohm's law:

$$\sigma_{\text{tot}} = \frac{l}{a \cdot b} \cdot \frac{1}{R} \quad (21)$$

Where  $l$  is the distance between contacts,  $a$  is the width and  $b$  is the thickness of the sample and  $R$ , the resistance of the material. The conductivity measurements are done by varying the temperature in the range of 600 – 900 °C and the activation energy  $E_a$  was analyzed on the basis of Arrhenius behavior

$$\sigma(T) = (A/T) \exp(-E_a/kT) \quad (22)$$

### 3 Experimental Methods

In case of dual phase compounds such as CGO-FCO which is a combination of an ionic and electronic conducting phase, the measured total conductivity predominantly represents the electronic conductivity of the compound.

#### **He-leak test**

The gas tightness of the membranes was evaluated by He-leak test. He-leak test is based on measuring the amount of helium gas passing through a leak in the sample for a period of time and depends on the pressure difference as well as the size and geometry of the leak path. Helium is added to one side of sample, and a vacuum is drawn on the other side of the sample. The container is pumped as long as a constant pressure  $p$  is set using two vacuum pumps. In this equilibrium, He-flow was measured using a He-leak detector (Qualytest HTL 260, Pfeiffer Vacuum GmbH, Asslar, Germany). He leak rate  $R$  is calculated from the measuring area of the sample  $A$  as follows:

$$R = \frac{1}{A} \cdot \frac{p\Delta v}{\Delta t} \quad (23)$$

where  $p$ ,  $v$  and  $t$  are pressure, volume and time respectively. The He Leak test of the sintered pellets showing values close to  $10^{-03}$ -  $10^{-06}$  mbar  $l/cm^2s$  confirm gas tightness appropriate for permeation test.

#### **Oxygen flux permeation measurement**

Oxygen permeation measurements can be carried out using a 3-end mode or 4-end mode set up. In this work, I have used 4-end mode permeation set up as shown in Figure 20. In this set up, the feed side has an inlet for the feed gas air and an outlet for the oxygen depleted air. Similarly on the sweep side, an inlet for the sweep gas (e.g. Argon) and an outlet for the oxygen enriched sweep gas or permeate gas. The permeate gas is then passed through a mass spectrometer or oxygen analyzer to obtain the oxygen concentration addressing  $N_2$  leakage if any to obtain the oxygen flux of the membrane.

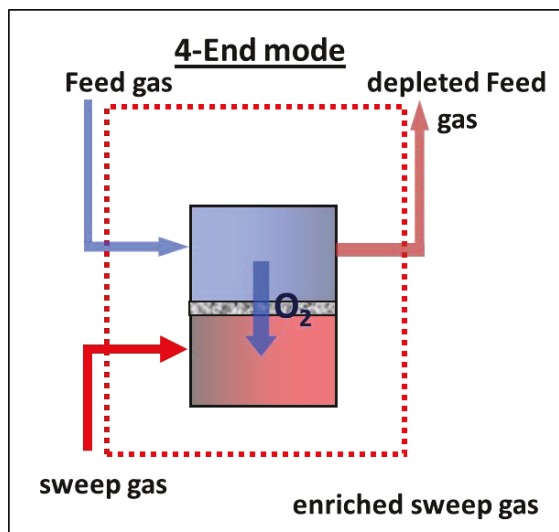


**Figure 20 A schematic of a 4-End mode permeation set up**

Dense membrane disks were subjected to 4-end mode permeation measurements on a cylindrical two chambers quartz reactor schematized in Figure 21. The inner chamber is 16 mm diameter with a flat holed bottom that supports the membrane. The dense membranes of 14.6 mm diameter are sealed with the help of 15 mm gold rings on both sides. Gold being inert and ductile was chosen to seal the membrane when heated at temperature  $>1000$  °C and pressed by a spring sited in the lid. Oxygen was separated from feed gas air using argon as sweep gas. The flow rate of all gas feed streams was controlled using mass flow controllers (MFCs). The standard flow rates ( $F$ ) used were  $50 \text{ mL min}^{-1}$  for feed and  $250 \text{ mL min}^{-1}$  for sweep. The mass spectrometer (Omni Star, Pfeiffer vaccum US) measured the gas content of the permeate. The oxygen concentration  $x(\text{O}_2)$  is calculated addressing the leakage correction of  $\text{N}_2$  concentration in the permeate gas. Hence oxygen flux permeation is calculated from  $\text{O}_2$  concentration in Ar flow for an effective area ( $A$ ) of the membrane by the following equation:

$$J(\text{O}_2) = \frac{\% \text{O}_2(\text{permeate})}{100 - \% \text{O}_2(\text{permeate})} \cdot \frac{F_{\text{Ar}}}{A} \quad (24)$$

### 3 Experimental Methods

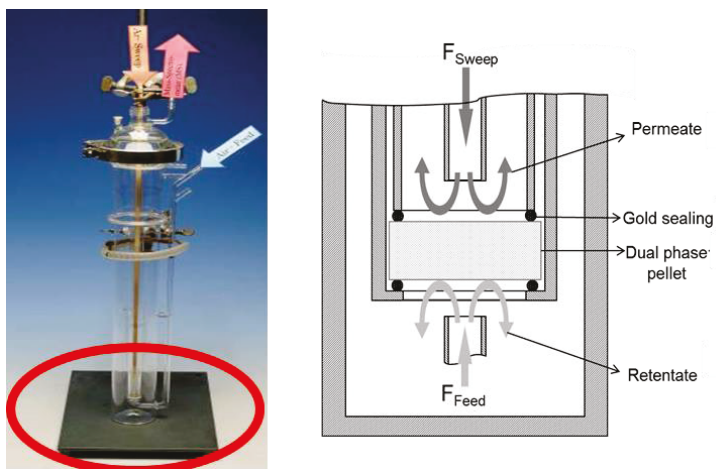


Figure 21 Quartz experimental setup and its schematic 4-end mode permeation measurement.

#### High pressure permeation measurement

High pressure is one of the attribute of the harsh ambience in an industrial application. Thus when high pressure application oxygen permeation measurement was possible at ORNL, utilizing the opportunity, a steel version of 4-End mode permeation setup, designed and made at IEK-1 as shown in Figure 22, was taken to ORNL during the second visit.

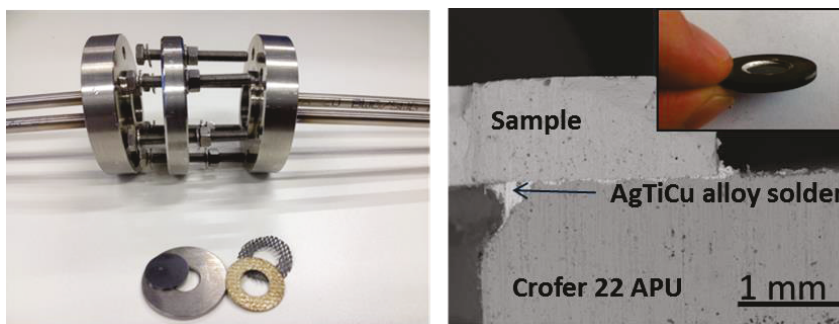


Figure 22 The 4-End mode steel permeation setup (left), CGO-FCO sintered pellet soldered to Crofer 22 APU gasket using AgTiCu based alloy, heat treated at 900 °C, SEM image of the cross section (right)

Apart from the permeation setup design, obtaining gas tight samples sealed to steel gaskets to withstand this high pressure application was a challenge. Addressing the issue, the sintered

sample was sealed along the edges to a Crofer® 22 APU (ThyssenKrupp VDM GmbH, Germany) steel gasket. Crofer® 22 APU is a high-temperature ferritic stainless steel which is thermodynamically very stable at temperatures up to 900 °C and its low thermal expansion coefficient matches with CGO-FCO ( $12\text{-}14 \times 10^{-6} \text{ K}^{-1}$ ) (Data\_Sheet\_VDM\_Crofer\_22\_APU). The Crofer 22 APU steel gasket of outer diameter 25 mm and inner diameter of 10 mm is soldered to the sample along the edges using AgTiCu alloy paste followed by heat treatment at 900 °C as shown in Figure 22. The 4-End mode permeation setup was connected with mass flow controllers (MFCs) and pressure gauges on both sides to control the feed and sweep gas flow and pressure during the permeation measurement. Feed gas of Air was supplied at the flow rate of 250 ml/min with 5 bar pressure application. On the sweep side, Ar was allowed to flow at the rate of 100 ml/min in atmospheric pressure (1 bar), while output flow was directly passed through an oxygen analyzer to monitor O<sub>2</sub>% periodically through the course of the experiment (Figure 23).

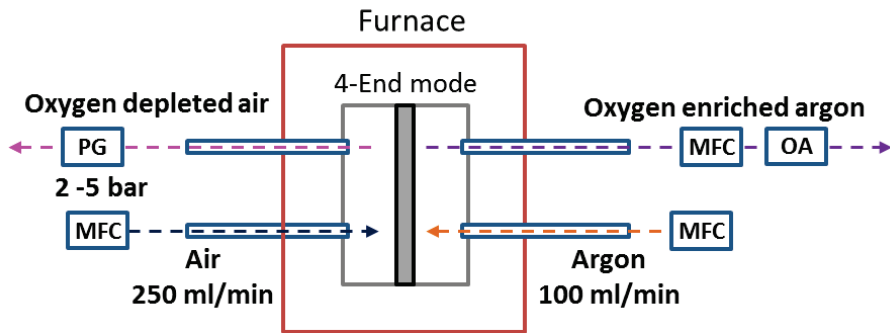


Figure 23 A sketch of the permeation measurement set up. PG – Pressure gauge, MFC – Mass flow controllers, OA – Oxygen analyzer

### Stability Testing

OTMs require long term stability in presence of aggressive atmospheres such as high pressure, flue gas containing CO<sub>2</sub>, SO<sub>2</sub>, H<sub>2</sub>O and dust at operating temperature on application in oxyfuel combustion. Thus stability testing in the presence of gases such as combinations of CO<sub>2</sub>, SO<sub>2</sub>, H<sub>2</sub>O and O<sub>2</sub> were investigated. The samples were ground to the size 10 mm diameter to ensure optimal fitting into the apparatus available at our collaborative project partner, Oak Ridge

### 3 Experimental Methods

National Laboratory. 4 sets of the samples were prepared for carrying out the stability testing in varying combinations of gas mixtures as listed below;

1. Pure CO<sub>2</sub>
2. 250 ppm of SO<sub>2</sub> in CO<sub>2</sub>
3. 250 ppm SO<sub>2</sub> + 5 vol% O<sub>2</sub> in CO<sub>2</sub>
4. 250 ppm SO<sub>2</sub> + 5 vol% O<sub>2</sub> + 2.5 vol% H<sub>2</sub>O (saturated at room temperature) in CO<sub>2</sub>

The samples were annealed in the furnace at 850 °C for 16 h allowing the above mentioned gas mixtures to flow through for the dwell time of the furnace. The samples were characterized post annealing test for their phase stability.

## 4. Results and Discussion

### 4.1. Material Selection

In the pre-selection Material review section, all the past literatures were accumulatively compared evaluating their performance and stability, to identify the most significant ionic conductor (Phase A) and electronic conductor (Phase B) combination. Doped ceria with its high ionic conductivity superior stability was chosen as the ionic conducting phase or Phase A of the dual phase membrane (Fagg '09). In case of Phase B, a choice of either a pure electronic conductor or MIEC material is possible. Hence for Phase B, spinels, perovskites and MIEC perovskites were investigated. Nevertheless, most of these materials possess electronic conductivity predominantly orders of magnitude higher than the ionic conductivity of doped ceria. Thus, a material with reasonable electronic conductivity (equivalent to ionic conductivity of doped ceria) with high stability was the main criteria for selection. Phase A -  $Ce_{0.8}Gd_{0.2}O_{2-\delta}$  (CGO) combined with different Phase B materials investigated in this section are shown in Table 4.

**Table 4 Dual Phase membranes with 60 wt % ionic conducting phase and 40 wt % electronic conducting phase were pechini synthesized and investigated.**

Compound Name	Chemical Composition	PSD in $\mu m$		
		D10	D50	D90
CGO-FCO	$Ce_{0.8}Gd_{0.2}O_{2-\delta} - FeCo_2O_4$	0.54	0.77	1.14
CGO-MCO	$Ce_{0.8}Gd_{0.2}O_{2-\delta} - MnCo_2O_4$	0.59	0.85	1.37
CGPO-FCO	$Ce_{0.8}Gd_{0.1}Pr_{0.1}O_{2-\delta} - FeCo_2O_4$	0.58	0.78	1.04
CGPO-MCO	$Ce_{0.8}Gd_{0.1}Pr_{0.1}O_{2-\delta} - MnCo_2O_4$	0.55	0.80	1.18
CGO-LNO	$Ce_{0.8}Gd_{0.2}O_{2-\delta} - La_2NiO_4$	0.48	0.67	0.92
CGO-LNC	$Ce_{0.8}Gd_{0.2}O_{2-\delta} - La_2Ni_{0.5}Co_{0.5}O_3$	0.53	0.72	0.99
CGO-FCrO	$Ce_{0.8}Gd_{0.2}O_{2-\delta} - FeCr_2O_4$	0.80	1.19	1.9
CGO-CoO	$Ce_{0.8}Gd_{0.2}O_{2-\delta} - CoO$	0.90	1.50	2.52
CGO-STF35	$Ce_{0.8}Gd_{0.2}O_{2-\delta} - SrTi_{0.65}Fe_{0.25}O_3$	0.60	0.91	1.37

#### 4.1.1. $\text{Ce}_{0.8}\text{Gd}_{0.2}\text{O}_{2-\delta}$ - $\text{M}(\text{Co}_2\text{O}_4)$ , $\text{M}=\text{Fe}, \text{Mn}$

Gd doped ceria was chosen as the Gd dopant provides the high ionic conductivity while Pr was also added (not in all samples), as it exhibits electronic conductivity to a certain extent (Fagg '09, Schmale '11). Initial experimentation work started with Fluorite – Spinel combination powders based on in house experience (Kringe '10, Lipińska-Chwałek '15). These compounds were synthesized by Pechini process, pressed and sintered to obtain dense pellets.

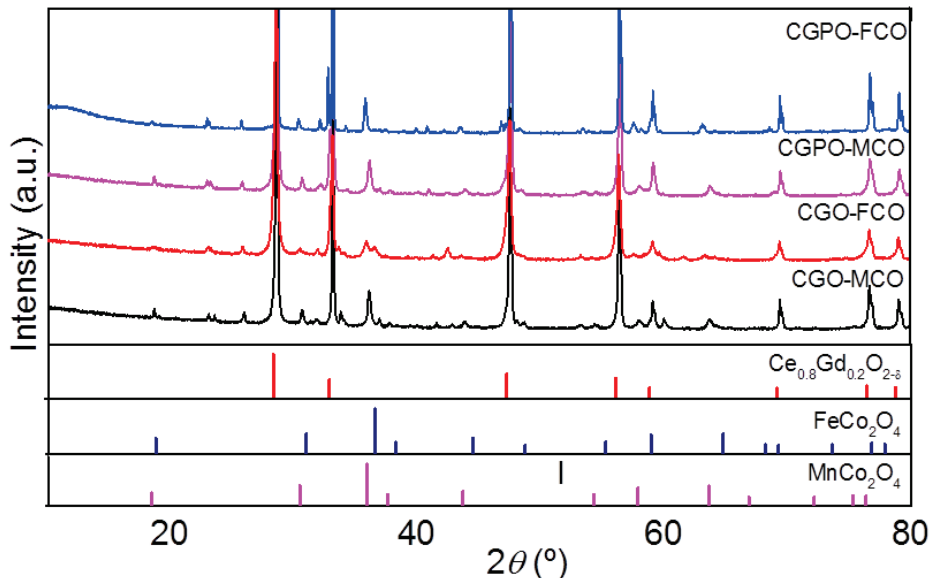


**Figure 24 XRD plots of the sintered dual phase pellets CGO-FCO, CGO-MCO, CGPO-FCO and CGPO-MCO (the compounds are mixed in 60 wt% fluorite to 40 wt% spinel proportion).**

XRD analysis of the sintered dual phase compounds showed presence of additional peaks apart from the spinel and fluorite phases as shown in Figure 24. The crystallographic phases matching the peaks of the XRD plots are listed in Table 5 for each dual phase compound. In case of CGO-FCO and CGPO-FCO compounds, presence of Gd and/Pr rich Fe oxide phase might contain traces of Co and Ce due to slight shift of the intensity peaks identifying the orthorhombic perovskite ( $\text{GdFeO}_3$ ) phase in XRD analysis. Similarly for CGO-MCO and CGPO-MCO, Gd and/Pr rich Co and Mn mixed oxide match the peaks of orthorhombic perovskite obtained through XRD analysis.

**Table 5 Crystallographic phases identified by XRD analysis of the sintered dual phase pellets (mixed in 60 wt% fluorite to 40 wt% spinel proportion). Green and purple cells indicate presence of peaks matching additional phases.**

Compound	Phase 1	Phase 2	Phase 3	Phase 4
CGO-FCO	Cubic ceria	Cubic spinel	Cubic rock salt	Orthorhombic perovskite
CGO-MCO	Cubic ceria	Cubic spinel	Cubic spinel	Orthorhombic perovskite
CGPO-FCO	Cubic ceria	Cubic spinel		Orthorhombic perovskite
CGPO-MCO	Cubic ceria	Cubic spinel		Orthorhombic perovskite

The XRD plots were zoomed between  $2\theta = 20 - 50^\circ$  to get a closer look at the additional peaks (Figure 25). The peaks between  $2\theta = 20 - 30^\circ$  and at  $33^\circ$  indicate the presence of an orthorhombic perovskite phase (Green). While the peak at  $2\theta = 44^\circ$  (Purple) indicate the presence of rock salt phase (spinel decomposition to rock salt) in case of Fe, Co Spinel.

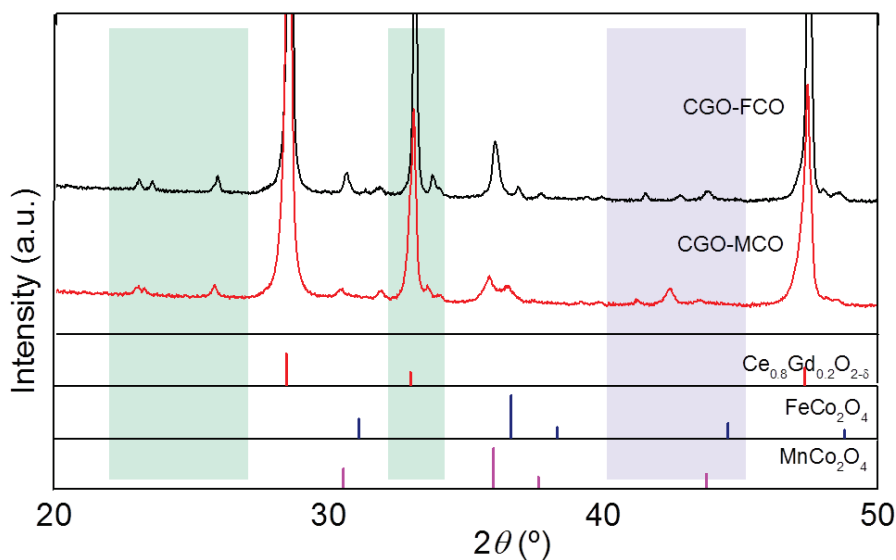


**Figure 25 XRD plots of CGO-FCO and CGO-MCO sintered pellets. Green box – orthorhombic perovskite peaks and purple box – rock salt phase observed in CGO-FCO.**

## 4 Results and Discussion

Cross section of the sintered samples was further investigated by SEM analysis. CGO-FCO compound shows the presence of Gd rich third phase (grey) in addition to Ceria based fluorite phase (white) and (Fe, Mn) Co based spinel phase (dark grey) as shown in Figure 26. Similarly, presence of Gd and/or Pr rich perovskites phase was observed in addition to the fluorite and spinel phases for the other three dual phase compounds as well.

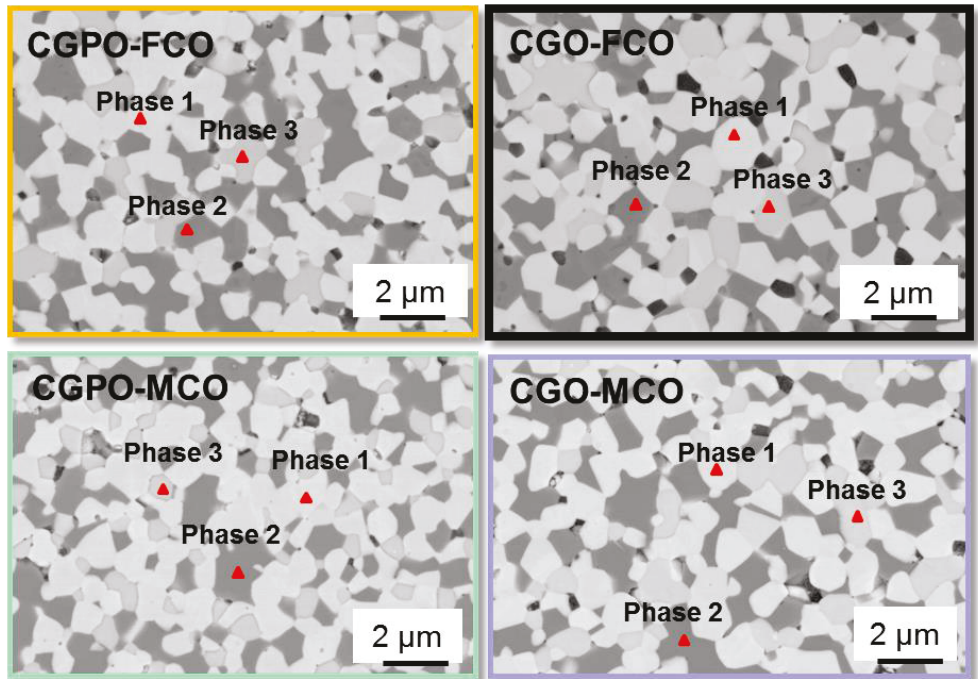


**Figure 26** SEM images of the four dual phase composites mixed in 60 wt% fluorite to 40 wt% spinel proportion after sintering at 1200°C for 10 h. Phase 1 – CGO, Phase 2 – (Fe, Mn) Co, Phase 3 – Perovskite.

The He Leak test of the sintered pellets had values close to  $10^{-05}$ -  $10^{-06}$  mbar l/cm<sup>2</sup>s confirming gas tightness appropriate for permeation test. The permeation results of the four dual phase compounds are shown in Figure 27. LSCF permeation results are also included in the plot as reference O<sub>2</sub> flux, considered more as a reference and target output expected from the dual phase material to be selected for the future experimentation work. At the intended operating temperature of 850 °C, O<sub>2</sub> flux of CGO-FCO, CGO-MCO, CGPO-FCO and CGPO-MCO compounds are relatively similar and almost half of O<sub>2</sub> flux measured in LSCF sample. Dual

phase membranes are more prone to surface exchange limitations in comparison to single phase LSCF MIEC membrane and hence the measured flux is expected to increase with surface activation. Addressing the surface limitations, the short listed dual membrane were surface activated and the results will be discussed in the later part of this chapter. Avoiding Pr and Mn dopants in the composite would enhance the stability of the dual phase membrane. Hence CGO-FCO composite was short listed among these four composites though the performance and microstructure of all four composites were similar.

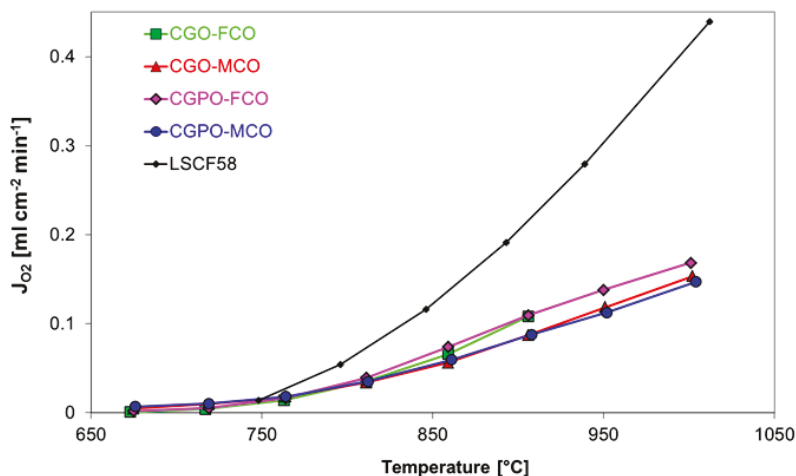


**Figure 27** Permeation test of CGO-FCO, CGO-MCO, CGPO-FCO and CGPO-MCO dual phase pellets (mixed in 60 wt% CGO to 40 wt% spinel proportion) compared to LSCF for reference.

#### 4.1.2. $\text{Ce}_{0.8}\text{Gd}_{0.2}\text{O}_{2-\delta}$ - CoO

Though CGO-FCO seems to be the composite of interest among the materials investigated so far, the spinel decomposition to rock salt phase and formation of perovskite phase by interacting with fluorite phase lead the path to explore alternate electronic conductors. This rock salt phase or monoxide phase has the NaCl type crystal structure. CoO is a high temperature stable phase in a Co-O system with p-type semi-conductivity and cation deficiency making it a good electronic conductor (Chen '03). In reference to electrical conductivity measurements of transition metal group based oxides and spinels, the total conductivity of CoO was high enough to be substituted for  $\text{FeCo}_2\text{O}_4$  spinel phase in the dual phase composite to avoid multiple phase formation (Kiefer

#### 4 Results and Discussion

'08). Hence the idea of combining CGO with CoO was realized experimentally for achieving equally efficient dual phase membrane with single electronic and ionic phases as required.

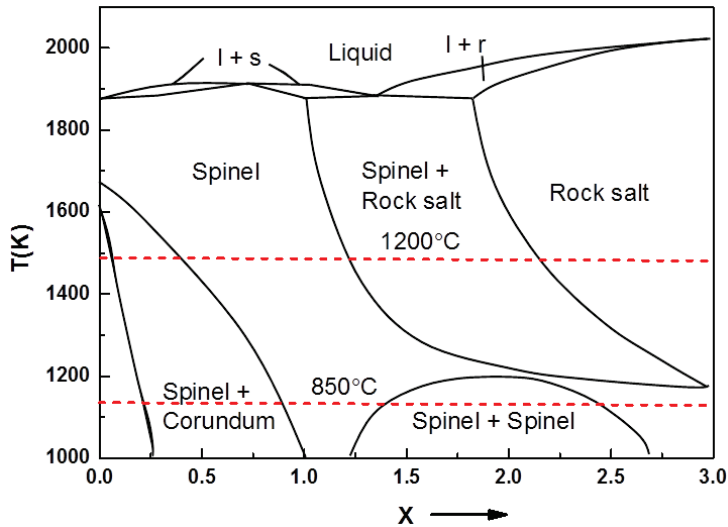


Figure 28 The Fe–Co oxide phase diagram in air at 1000–2100 K.  $x$  is 2 in  $\text{Co}_x \text{Fe}_{3-x} \text{O}_{4\pm\delta}$  for the dual phase compound of our interest (Hansson '05).

CGO-CoO dual phases composite was Pechini synthesized calcined at 700 °C for 15 h and ball milled for 24 h. The XRD analysis of the powder showed presence of CGO and  $\text{Co}_3\text{O}_4$  phases.

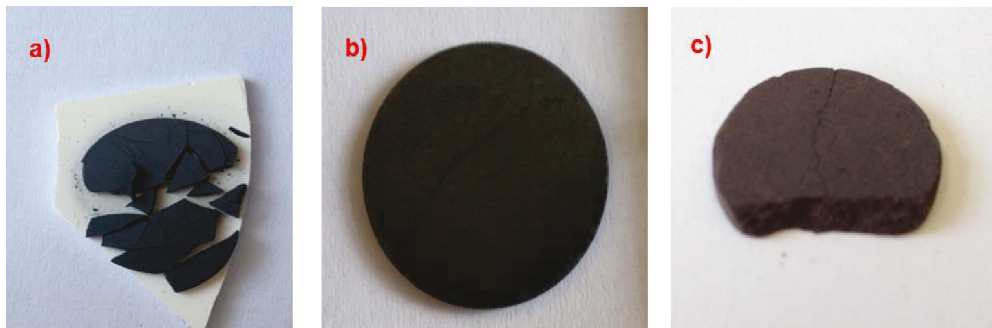


Figure 29 60 wt% CGO - 40 wt% CoO sample a) Sintered @1200 °C with cooling rate 3 K/min, b) Sintered @1200 °C with cooling rate 0.5 K/min, c) Powder calcined @1000 °C in Ar and sintered @1200 °C 1h in Ar

On sintering at 1200 °C CoO was expected to be formed as identified in Figure 28. Sintering attempts were made at 1200 °C for 10 h with both fast (3 K/min) and slow (0.5 K/min) cooling rate, but the samples cracked severely as shown in Figure 29 a & b. XRD analysis showed only traces of CoO in addition to Co<sub>3</sub>O<sub>4</sub> spinel phase after the sintering process. The visible cracks are attributed to volume expansion during rocksalt to spinel and vice versa phase transformation during the sintering process (Bahlawane '09). The major conclusion from these results is the difficulty to arrest the intended CoO phase during sintering process in accordance with Figure 28 and volume expansion that accompanies the phase transformation causing the samples to crack. Another approach was calcining the powder at 1000 °C in Ar atmosphere to arrest rock salt phase and avoid phase transformation due to lack of oxygen availability, this also means sintering the pellet in reducing atmosphere to hold onto to the rock salt phase. This approach failed since the calcined powder was coarse and was not densified after sintering. Also considering the application of the membrane is oxygen separation; this approach would not be a viable option to manufacture even if it had been successful. Based on all the failed approaches listed above, this dual phase combination was also shelved.

#### 4.1.3. Ce<sub>0.8</sub>Gd<sub>0.2</sub>O<sub>2-δ</sub> - FeCr<sub>2</sub>O<sub>4</sub>

In contrast to avoiding Fe to eliminate multiple phase formation in the previous case, Cr was used as a replacement option for Co to avoid the secondary phase observed in case of CGO-FCO composite. Pechini synthesized CGO-FCrO powder was calcined at 700 °C for 15 h (similar to CGO-FCO synthesis procedure). The pressed pellets were sintered at temperatures ranging from 1200 °C to 1400 °C in air and 1200 °C in Ar atmosphere as well, in an attempt to obtain gas tight samples, but were proven to be unsuccessful. XRD analysis also indicated that required spinel phase was not formed in any of the above mentioned sintering conditions (Figure 30). Many peaks matching different unintended perovskite phases were observed (Green shaded region), while some spinel peaks disappeared (purple shaded region). Problem of densification and formation of unintended and undesirable phases has led to discontinuation of future focus on this dual phase composite.

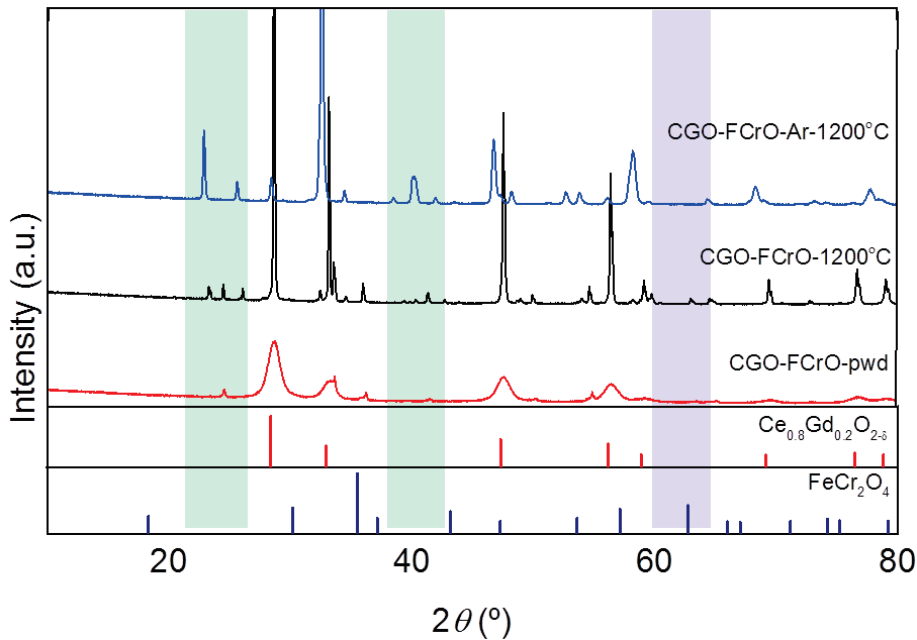
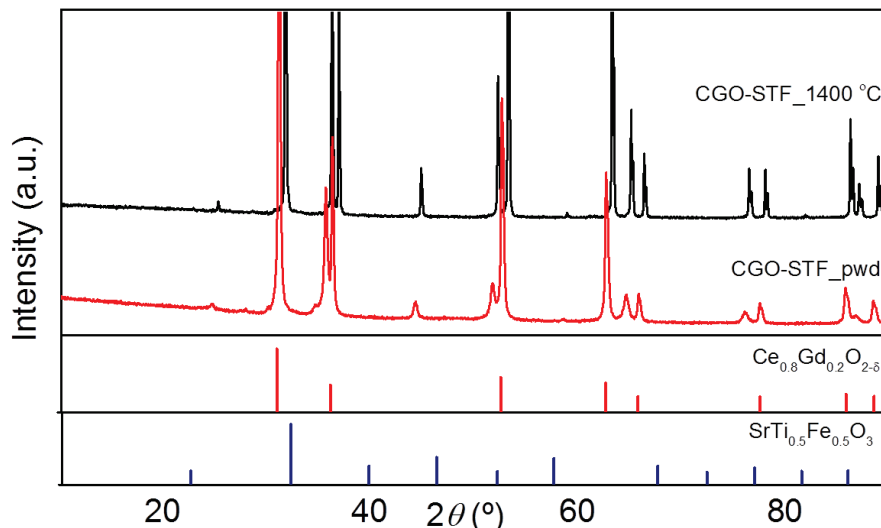


Figure 30 XRD plot of 60 wt% CGO-40 wt% FCrO composite as powder, sintered in air and argon at 1200 °C. Green region – unintered perovskite phase peaks and purple region – spinel peaks disappear.

#### 4.1.4. $\text{Ce}_{0.8}\text{Gd}_{0.2}\text{O}_{2-\delta}$ - $\text{SrTi}_{0.65}\text{Fe}_{0.35}\text{O}_3$

MIEC materials in place of pure electronic conductors could be a significant combination with ionic conductor in a dual phase composite. Based on prominent mixed conductivity of STF along with its good chemical and thermal stability (Schulze-Küppers '15), CGO-STF was considered a potential dual phase composite to exhibit substantial  $\text{O}_2$  flux. The Pechini synthesized powder was calcined at 900 °C for 10 h and ball milled for 48 h.



**Figure 31** XRD plot of 60 wt% CGO – 40 wt% STF as powder and sintered (1400 °C for 5 h) pellet with the intended phases.

The pressed pellets were sintered at 1400 °C for 5 h to obtain gas tight samples. XRD of the powder and sintered pellet confirmed the presence of fluorite and perovskite phase as expected, shown in Figure 31.

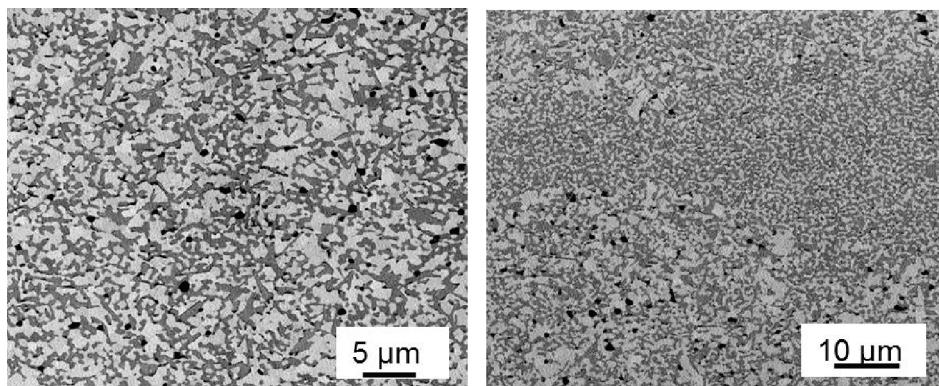


**Figure 32** SEM image of 60 wt% CGO – 40 wt% STF pressed pellet sintered at 1400 °C for 5 h. Left – Varying grain size of phases, Right – inhomogenous distribution of phases.

## 4 Results and Discussion

SEM images also confirmed the presence of only 2 phases distributed through the sample, though the grain size of the phases were not homogeneously distributed as shown in Figure 32.

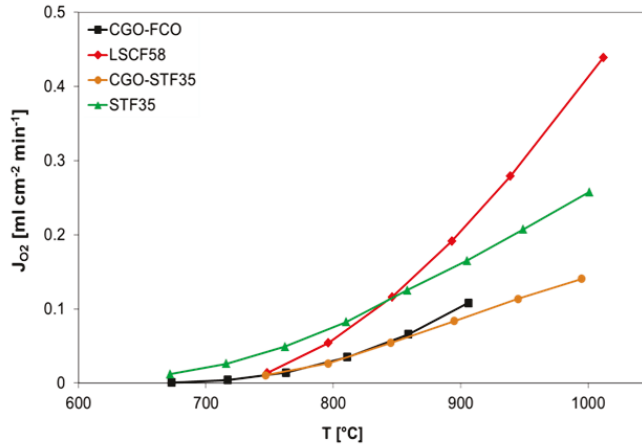


**Figure 33 oxygen flux of 60 wt% CGO – 40 wt% STF compared to 60 wt% CGO – 40 wt% FCO, single phase STF and LSCF.**

The O<sub>2</sub> flux of the CGO-STF seemed to be in par with CGO-FCO (the other dual phase composite of interest) as shown in Figure 33. Interestingly, STF35 as single phase MIEC pellet had higher O<sub>2</sub> flux than the dual phase composite which is not clear, since the ionic conductivity of CGO is higher than STF (Molin '12). Hence permeance and permeability are calculated from their O<sub>2</sub> flux measurements, normalizing the impact of pressure gradient and membrane thickness. The Arrhenius behavior of the permeance clearly depicts the ambipolar conductivity as the driving force of normalized permeation rate, thus equation (7) can be written as:

$$Permeance = \frac{J_{O_2}}{\ln \frac{p^i_{O_2}}{p^o_{O_2}}}; \quad (25)$$

$$Permeability = \frac{J_{O_2}}{\ln \frac{p^i_{O_2}}{p^o_{O_2}}} * L \approx \sigma_i T \quad (26)$$

Permeance and permeability of the composite were calculated using the O<sub>2</sub> flux measurements of the CGO-STF membrane. In the permeability plot Figure 34 is shown to normalize the flux value taking into account the partial pressure and thickness since STF was of thickness 0.15 cm while

CGO-STF was 0.13 cm. Enhancement factor  $\eta$  was calculated from the ratio of permeability of CGO-STF and STF to understand the influence of CGO in case of the dual phase compound.

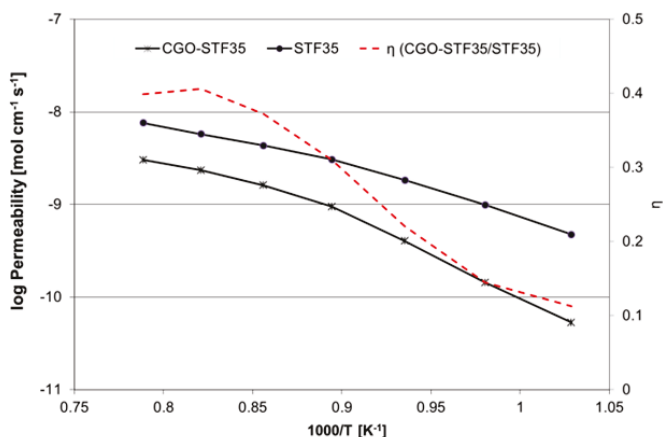


**Figure 34** Permeability plot of STF and 60 wt% CGO – 40 wt% STF along with their enhancement factor

At high temperatures above 850 °C, the reduction of enhancement factor is in accordance with the vol % of CGO present in the composite. And at lower temperatures, enhancement factor further reduces potentially due to surface exchange problems. Single phase STF material is found to be unstable in CO<sub>2</sub>, SO<sub>2</sub> and H<sub>2</sub>O gas mixtures conducted as a parallel experiment. Hence it can be concluded that STF as Phase B in the dual phase membrane for oxyfuel combustion is not a viable option. Nevertheless, STF as single phase MIEC membrane can be applied to membrane reactor applications as it is CO<sub>2</sub> stable.

#### 4.1.5. Ce<sub>0.8</sub>Gd<sub>0.2</sub>O<sub>2-δ</sub> – La<sub>2</sub>Ni<sub>0.5</sub>Co<sub>0.5</sub>O<sub>3</sub>

Strontium free perovskite material with fluorite was another possible dual phase combination worth exploring with chemical stability as an important criterion; Hence dual phase compound of 60 wt% CGO with 40 wt% LNC (La<sub>2</sub>Ni<sub>0.5</sub>Co<sub>0.5</sub>O<sub>3</sub>) perovskite, a pure electronic conductor (Tietz '16) was investigated. The powder was synthesized by Pechini route from their nitrates followed by calcination at 900 °C for 4 h and ball milled for 24 h. The synthesized powder was subjected to XRD analysis as shown in Table 6. Unfortunately expected phases were not formed. NiO and

## 4 Results and Discussion

Gd<sub>2</sub>O<sub>3</sub> were identified from the additional peaks indicating the decomposition intended phases which might eventually affect the oxygen transport. Obtaining these compounds with only desired two phases via Pechini process have proven to be unsuccessful. Hence this combination was not further investigated.

**Table 6 XRD analysis of Pechini processed 60 wt% CGO with 40 wt% LNC dual phase compound as powder**

Compound	Phase 1	Phase 2	Phase 3	Phase 4
CGO-LNC	CeO <sub>2</sub> - Cubic	LaCo <sub>0.5</sub> Ni <sub>0.5</sub> O <sub>3</sub> - Rhombohedral	Gd <sub>2</sub> O <sub>3</sub> - Cubic	NiO - Cubic

Thus, these powders were not further investigated considering the multiple phases in the powder form in addition to reactivity of lanthanum with other compounds.

### 4.1.6. Ce<sub>0.8</sub>Gd<sub>0.2</sub>O<sub>2-δ</sub> – La<sub>2</sub>NiO<sub>4</sub>

Alternative option as a significant electronic or MIEC phase was K<sub>2</sub>NiF<sub>4</sub> structure material. So, dual phase composite CGO with Lanthanum Nickelate (LNO) was investigated. Pechini route synthesized powder calcined at 900 °C did not possess the expected phases due to reactivity of La with Ce and Gd and NiO formation similar to behavior observed in CGO-LNC composite.

**Table 7 XRD analysis of Pechini processed 60 wt% CGO with 40 wt% LNO dual phase compound as powder**

Compound	Phase 1	Phase 2	Phase 3	Phase 4
CGO-LNO	CeO <sub>2</sub> - Cubic	La <sub>3</sub> NiO <sub>7</sub> - orthorhombic	Gd <sub>2</sub> O <sub>3</sub> - Cubic	NiO - Cubic

The possible reason for more than 2 phases formed by Pechini process could be inadequate calcination temperature since Lanthanum Nickelate has a tendency to easily form more than one phase that is only stable at temperature above 1000 °C in air (Bannikov '06, Gauquelin '09, Rice '93).

In an effort to control the reactivity of the compounds observed in Pechini route, CGO-LNO dual phase compound was synthesized by conventional solid state reaction method. Commercially

available individual phase powders 60 wt% CGO and 40 wt% LNO (Treibacher Industrie AG, 99%) were mixed by milling in a planetary ball mill for 48 h. The synthesized powder was pressed and sintered to obtain dense samples. Gas tight CGO-LNO pellet was obtained when sintered at 1400 °C for 5 h. XRD analysis showed presence of only  $Ce_4O_7$  and NiO phases on both sides of the pellet. Figure 35 shows the SEM analysis indicating about 20  $\mu\text{m}$  from surface into sample was leached off the second phase on one side (left) whereas the other side of the surface seems to have second phase (right).

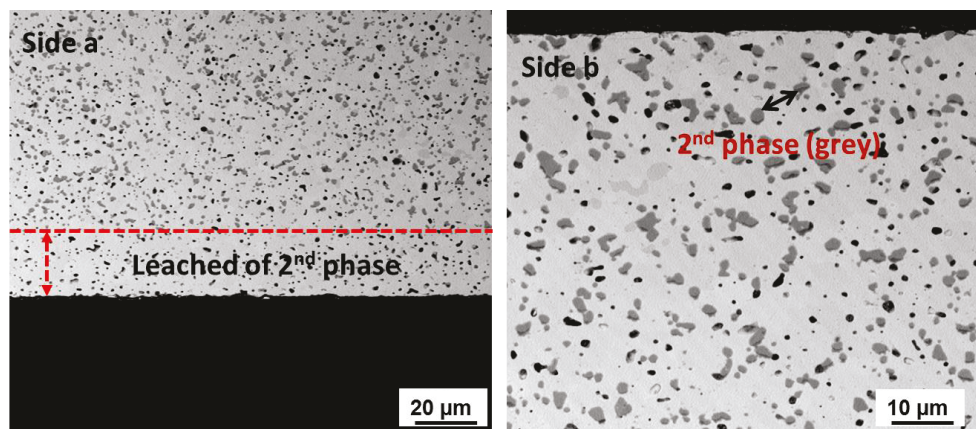


**Figure 35** SEM images of 60 wt% CGO with 40 wt% LNO sample sintered at 1400 °C. Side a – Leached 2<sup>nd</sup> phase (grey), side b – 2<sup>nd</sup> phase (grey) visible.

To better understand potential decomposition of Lanthanum Nickelate phase, a sintering study was carried out from 1200 ° to 1400 °C with every 50 °C increment and the samples were analyzed by XRD as shown in Figure 36. XRD analysis showed that  $Ce_4O_7$  was formed under varying sintering temperature which contributes to the ionic conductivity. But Lanthanum Nickelate tends to form nickel rich Ruddlesden-Popper phase ( $La_3NiO_7$ ) (Gauquelin '09) which transforms to  $La_2NiO_4$  phase with increasing sintering temperature as reported in Table 8. However, with further increase in sintering temperature,  $La_3NiO_7$  and  $La_2NiO_4$  phases (decompose to NiO (green region) around temperatures 1300 °C and higher as shown in Figure 36 and Table 8. Since 1400 °C is necessary for obtaining gas tight pellets, sintering at temperature above 1300 °C is critical.

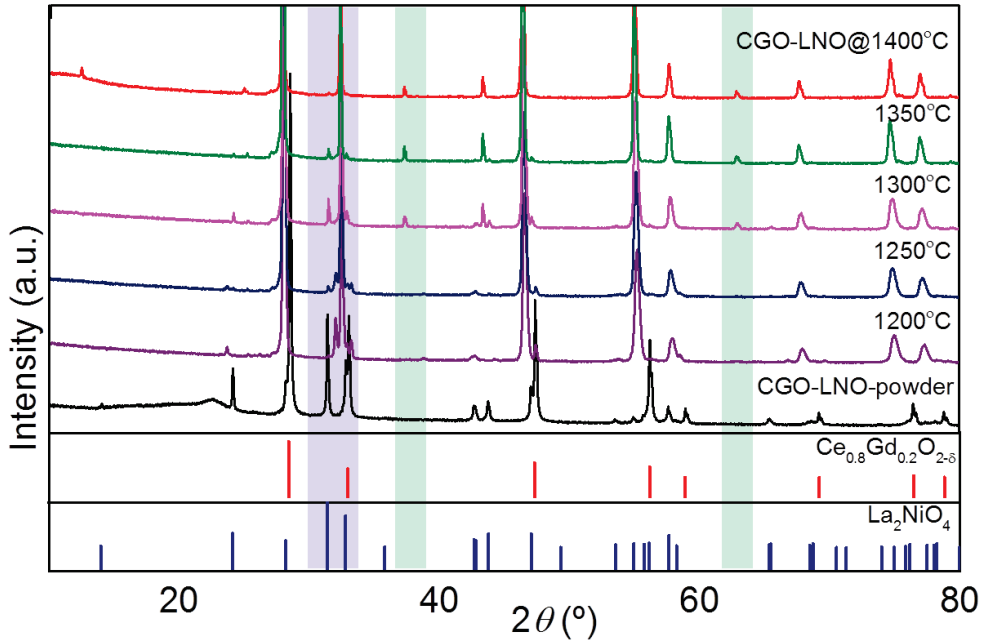
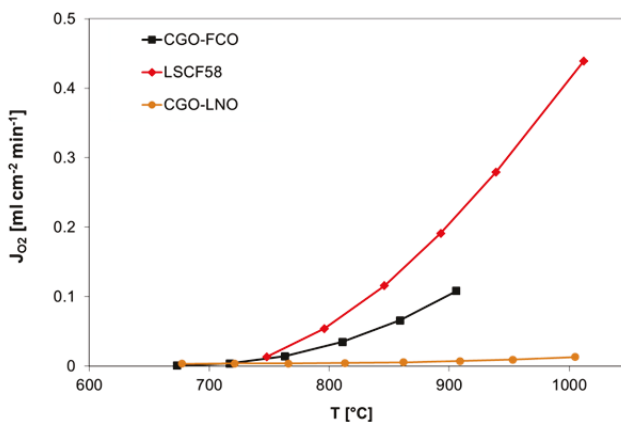


Figure 36 XRD plot of 60 wt% CGO with 40 wt% LNO sintering study. NiO (green shaded region) formed around temperature  $\geq 1300^\circ\text{C}$ , LNO peaks (purple shaded region) only visible in powder, 1250  $^\circ\text{C}$  to 1350  $^\circ\text{C}$

Table 8 Crystallographic phases identified by XRD analysis of 60 wt% CGO with 40 wt% LNO sintering study samples

CGO-LNO sintering Temperature ( $^\circ\text{C}$ )	Phase 1	Phase 2	Phase 3
1200	$\text{Ce}_4\text{O}_7$ - Cubic	$\text{La}_3\text{NiO}_7$ - Orthorhombic	
1250	$\text{Ce}_4\text{O}_7$ - Cubic	$\text{La}_3\text{NiO}_7$ - Orthorhombic	$\text{La}_2\text{NiO}_4$ - Tetragonal
1300	$\text{Ce}_4\text{O}_7$ - Cubic	$\text{La}_2\text{NiO}_4$ - Tetragonal	NiO - Cubic
1350	$\text{Ce}_4\text{O}_7$ - Cubic	NiO - Cubic	$\text{La}_2\text{NiO}_4$ - Tetragonal
1400	$\text{Ce}_4\text{O}_7$ - Cubic	NiO - Cubic	

Permeation test of CGO-LNO sintered at 1400 °C for 5 h showed very low O<sub>2</sub> flux in comparison to CGO-FCO as shown in Figure 37. The poor O<sub>2</sub> flux could be explained based on the unstable phase transformation and secondary phase formation during sintering process, as well as the inhomogeneous distribution of the phases observed in SEM analysis affecting the percolating network of the membrane.



**Figure 37** Permeation test of 60 wt% CGO with 40 wt% LNO sintered at 1400 °C

Thus considering the complications addressed during development of Fluorite - Lanthanum Nickelate based membranes, these combinations will not be investigated further.

#### 4.1.7. Conclusion on Section 4.1

Summarizing the material selection section, several pure electronic conductors and MIEC materials were screened in combination with CGO for selecting the most promising dual phase composite. Pure electronic conductors such as CoO, FeCr<sub>2</sub>O<sub>4</sub> and La<sub>2</sub>Ni<sub>0.5</sub>Co<sub>0.5</sub>O<sub>3</sub> mixed with CGO involved process difficulties in obtaining the desired dense dual phase membranes. In case CGO combination with MIEC, CGO-LNO again showed processing difficulties and poor oxygen permeation performance. However CGO-STF had reasonable oxygen permeation though phase interaction would still be a concern. Nevertheless, with chemical stability as one of the main criteria, avoiding Pr and Sr containing combinations would be more advantageous. Hence CGO-FCO has been chosen as the material of interest for the research objective of this PhD thesis.

## 4.2. $\text{Ce}_{0.8}\text{Gd}_{0.2}\text{O}_{2-\delta}$ - $\text{FeCo}_2\text{O}_4$ Dual Phase Composite

The 60 wt% CGO combined with 40 wt% FCO to form the dual phase composite was chosen as the OTM material of interest. This dual phase membrane was subjected to detailed characterization to identify the phases present, understand the phase interaction and secondary phase formation. The impact of such interactions and additional phase formations on the oxygen permeation of the membrane was further investigated. In this section, optimization of composite microstructure has also been focused by experimenting different powder synthesis routes and alternate pressure induced sintering processes of the chosen dual phase membrane.

### 4.2.1. CGO-FCO Phase Evolution

The XRD plot of the CGO-FCO dual phase pellet after sintering at 1200 °C for 10 h, showed presence of the CGO and two cubic spinel phases, matching Co rich and Fe rich spinels, in addition an orthorhombic perovskite ( $\text{GdFeO}_3$ ), and a Co rich rocksalt phase ( $\text{CoO}$ ) were also present (Figure 38).

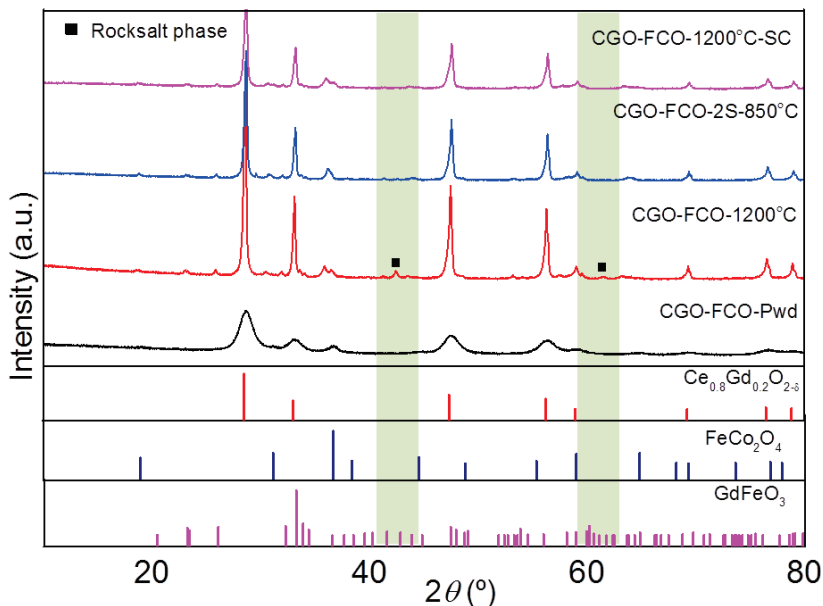
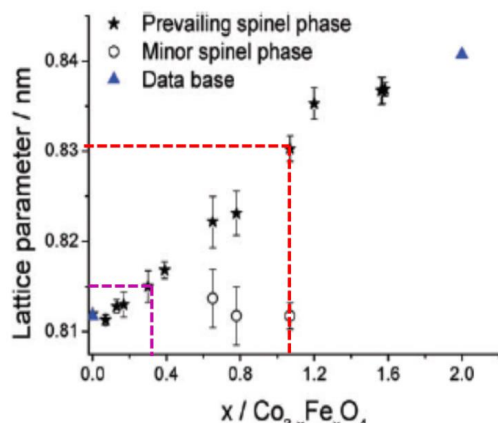


Figure 38 XRD plot of 60 wt% CGO – 40 wt% FCO as powder, sintered at 1200 °C for 10 h, annealing sintered sample at 850 °C for 100 h (marked as 2S-850 °C) and sintering at 1200 °C for 10 h with additional slow cooling from 900 °C to 800 °C (marked as SC)



**Figure 39** Varying lattice parameter of spinel structure as a function of Fe incorporated into  $\text{Co}_3\text{O}_4$  (Bahlawane '09). Lattice parameter 8.3 Å and 8.15 Å are marked to identify Co dopant concentration.

A post annealing test of the sintered sample in air at the targeted operation temperature of 850 °C for 100 h showed disappearance of the rocksalt phase, while the two spinel phases as well as the perovskite remain in accordance with Figure 28. The phases were quantified by Rietveld refinement as shown in Table 9. At 850 °C two spinel phases with different Co-doping concentrations are in equilibrium, differing in the lattice parameter due to the different Co/Fe-ratio. The lattice parameters of both the spinel phases are determined from the Rietveld refinement of the sintered sample. Using the calculated lattice parameters in the Vegard's plot (Figure

39), the doping concentration of Co is estimated as 1.85 and 2.65 for the larger and smaller unit cell, respectively.

**Table 9** Quantification of the phases formed in 60 wt% CGO – 40 wt% FCO composite after sintering using Rietveld analysis.

Crystal system-structure	Sintered at 1200 °C, 10 h		Annealed at 850 °C, 100 h	
	Fraction wt %	Lattice parameter a (Å)	Fraction wt %	Lattice parameter a (Å)
CGO (Cubic – Fluorite)	58	5.417	73	5.418
FCO (Cubic – Spinel)	14	8.309	11	8.300
	18	8.147	7	8.159
(Co, Fe)O (Cubic - Rock salt)	3	4.260	-	-
GdFe (Ce,Co) O <sub>3</sub> Orthorhombic - Perovskite	7	a = 5.337	9	a = 5.336
		b = 5.612		b = 5.613
		c = 7.653		c = 7.656

#### 4 Results and Discussion

However, the phase equilibrium of the CGO phase in the composite is affected because of the formation of the additional perovskite phase,  $GdFeO_3$ . Therefore, the spinel phases show Fe depletion. Moreover, the phases might change during cooling and particularly in the sintered sample do not represent the thermal equilibrium at sintering and annealing temperature, respectively. Figure 40 shows the backscattered electrons SEM image of the sintered (1200 °C, 10 h) composite with the presence of three phases marked. These results confirm the formation of a Gd, Fe rich perovskite phase (medium grey) besides the desired CGO (light grey) and spinel (dark grey).

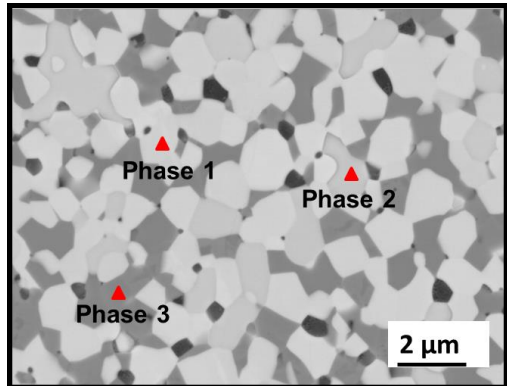


**Figure 40 SEM image of 60 wt% CGO – 40 wt% FCO marked with Phase 1 –Fluorite, Phase 2 – Perovskite and Phase 3 – Spinel.**

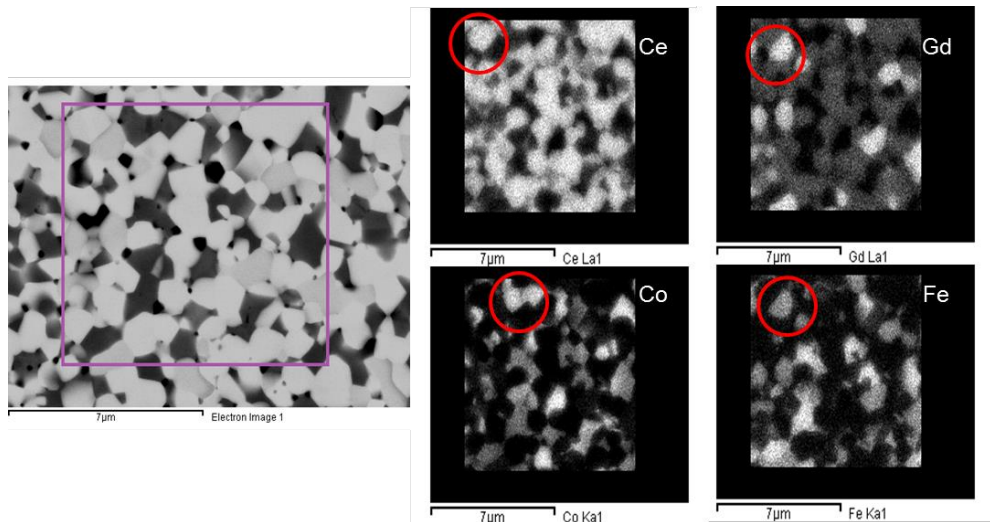


**Figure 41 SEM image with elemental mapping of the compounds present in 60 wt% CGO – 40 wt% FCO composite.**

The SEM elemental mapping of the zone in Figure 41 shows the presence of Gd and Fe in the same medium grey grains, while spinel grains show strong Co with deprived Fe in most places. Nevertheless, the different spinel phases cannot be resolved with SEM/EDS.

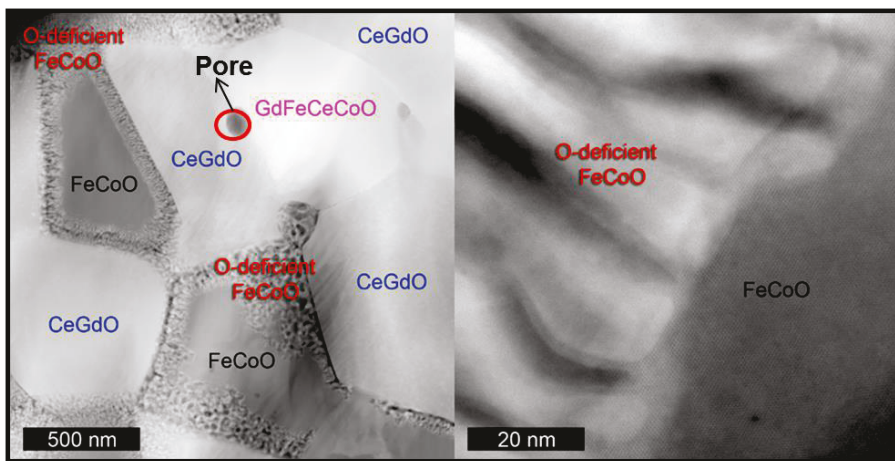


**Figure 42** STEM–HAADF image of the 60 wt% CGO – 40 wt% FCO sample showing the presence of additional phases (left). Higher magnification image of the boundary phase present in FCO grain (right)

For more detailed analysis STEM-HAADF imaging and EELS was performed on as-sintered sample which further confirmed the presence of the orthorhombic perovskite phase ( $\text{GdFeO}_3$  with traces of Ce and Co). Moreover, STEM-HAADF image shows the presence of grain boundary phase located only in the grain boundary between fluorite and spinel or perovskite and spinel, but not between two spinel grains (Figure 42). EELS analysis identified that the grain boundary phase is reduced in oxygen content as shown in Figure 43. Apparently, this is the rocksalt phase identified in XRD. Summarizing the structure investigation revealed that an orthorhombic perovskite phase forms at sintering temperature of 1200 °C that remains stable. Although this phase formation was not intended, it forms single grains that are not blocking any ion or electronic conducting pathways (Shaula '04). This might tend to slightly reduce the effective cross section for permeation. On the other hand, the presence of Ce and Co in the  $\text{GdFeO}_3$  lattice might introduce certain conductivity that is clarified in the following section. Lin

## 4 Results and Discussion

et al have stated the presence of the third phase, orthorhombic perovskite which provided added ionic conductivity to the dual phase composite (Lin '15).

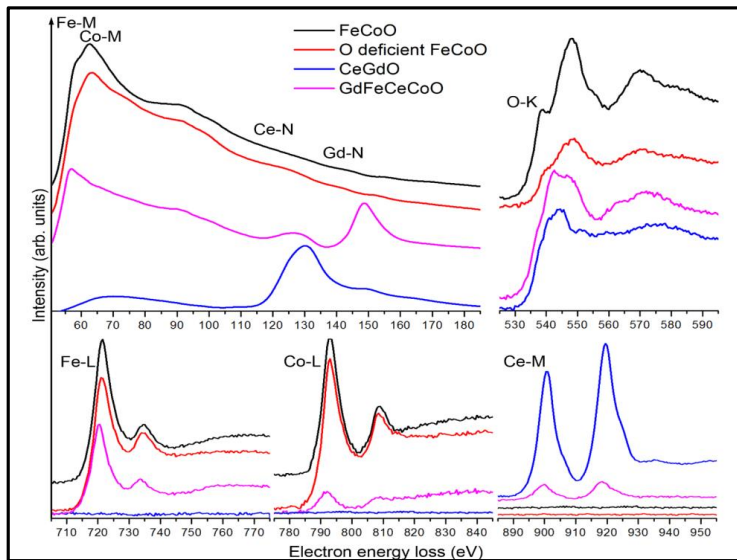


**Figure 43** Characteristic EELS spectra recorded from the grains in 60 wt% CGO – 40 wt% FCO sample

The major conclusion is that the percolating phases exist enabling simultaneous ionic (CGO) and electronic (spinel, rocksalt) conduction. Hence, the composite can still be considered as a MIEC material (Ramasamy '16).

### **Gd<sub>0.85</sub>Ce<sub>0.15</sub>Fe<sub>0.75</sub>Co<sub>0.25</sub>O<sub>3</sub> (GCFCO) perovskite phase**

The STEM-HAADF and EDS element mapping of CGO-FCO sample revealed the presence of GdFeO<sub>3</sub> perovskite phase, in which a minor content of Ce and Co was also dissolved. Hence a semi-quantification of the perovskite phase was determined from the EDS element mapping of a particular region in the composite. This semi quantified values of each element for a particular perovskite grain as shown in Figure 44 were taken into account to frame a stoichiometric composition Gd<sub>0.85</sub>Ce<sub>0.15</sub>Fe<sub>0.75</sub>Co<sub>0.25</sub>O<sub>3</sub>. Since Ce and Gd peaks overlap making the quantification of the elements difficult. The CL factor calculated from Cliff-Lorimer method is used for the quantification of the elements in the EDS mapped image.

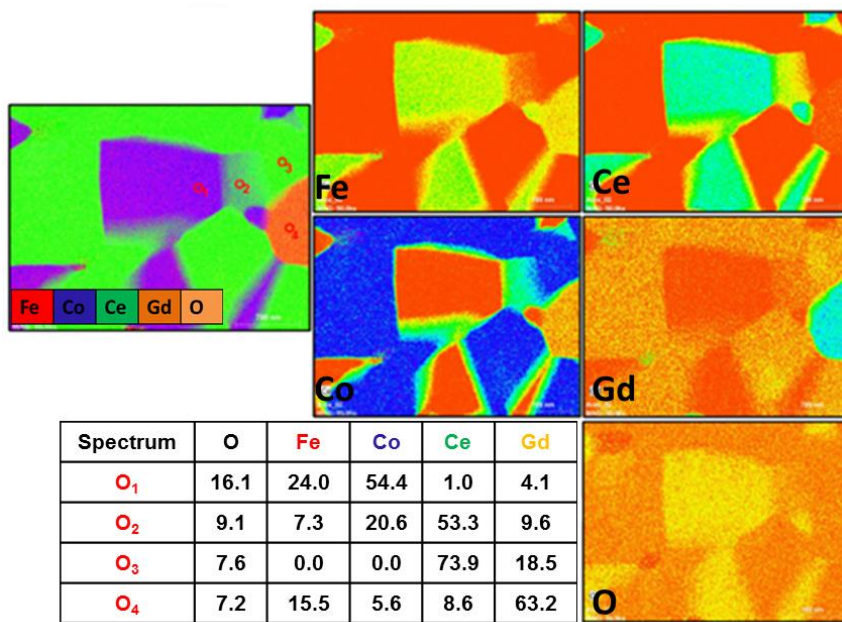


**Figure 44** STEM-HAADF image, EDS element mapping and semi-quantitative results of 60 wt% CGO – 40 wt% FCO sintered sample annealed at 850 °C for 100 h in air.

This  $\text{Gd}_{0.85}\text{Ce}_{0.15}\text{Fe}_{0.75}\text{Co}_{0.25}\text{O}_3$  (GCFCO) individual phase was synthesized by Pechini process, pressed and sintered into dense samples at 1400 °C for 5 h. The performance of the individual phase along with the dual phase membrane is discussed in section 4.2.2.

### Optimized Conventional sintering

DTA/TG analysis (Figure 45) of the CGO-FCO powder showed mass loss associated with endothermic reaction while heating up between 900-1000 °C, this confirms the phase transformation of spinel into rocksalt phase as shown in the phase diagram of the Fe-Co-O system. The reversible phase transformation of rocksalt phase to spinel phase associated with balancing mass gain occurs during cooling down between temperatures 900-800 °C again supporting the phase diagram of the Fe-Co-O system. This mass loss and gain during the heating and cooling process can be attributed to the change of cobalt valence state and resulting oxygen exchange with the gas phase associated with the phase transformation.

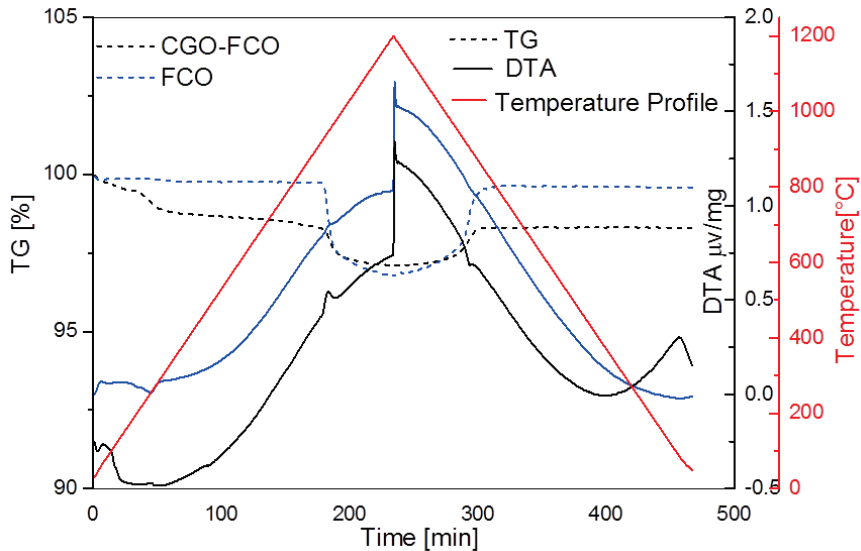


**Figure 45** DTA/TG analysis of 60 wt% CGO – 40 wt% FCO powder subjected to sintering cycle at 3 K/min upto 1200 °C and back in air.

The composites sintered at 1200 °C with standard heating and cooling rate tend to show distributed micro-cracks on both sides observable after polishing. These micro-cracks could be related to the phase changes observed in the DTA/TG analysis. The post annealing experiment in air at the targeted operation temperature of 850 °C for 100 h, revealed the absence of rocksalt phase, while the two spinel phases as well as the perovskite remain. Thus, the sintering cycle was modified to include slow cooling rate (0.5 K/min) between 900-800 °C in order to accommodate the time necessary to reach thermal equilibrium of the phases. Indeed, micro-cracks were no longer observed following this procedure. In addition, the XRD plot of such sintered pellet showed no traces of rocksalt phase resembling the post-annealed sample thus validating the modified sintering procedure.

### Phase interaction study

In order to investigate the phase interaction noticed in the composite with more depth, a systematic study was performed with support from Christian Doppler Laboratory project group. The experiment involves PLD coating FCO thin layers on polycrystalline CGO substrates, performing annealing experiments and analyzing the pre and post annealed samples by X-ray

diffraction. Polished CGO pellets, PLD coated with FCO were subsequently subjected to different annealing temperatures for varying dwell times to investigate the phase interaction and hence the formation of the orthorhombic perovskite phase. In XRD measurements directly after PLD-deposition, the samples show patterns of CGO, as well as two spinels – nominally Co-rich and Co-lean phases.

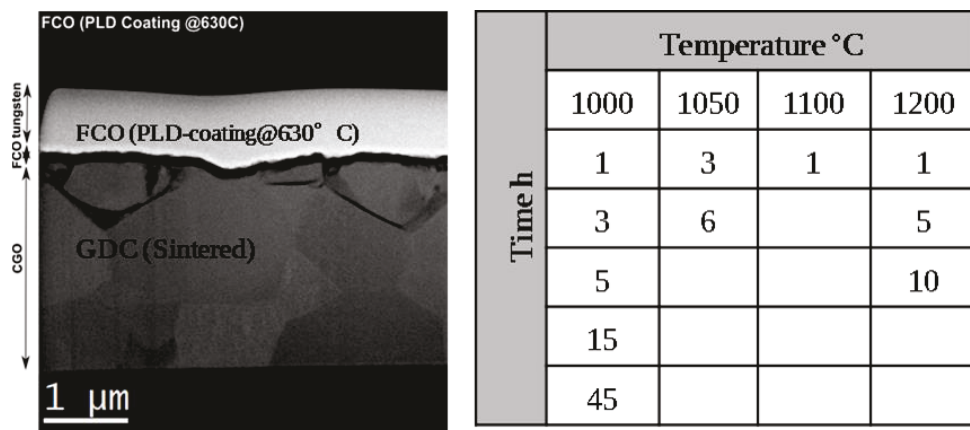


**Figure 46** STEM-HAADF image of a CGO substrate PLD coated with FCO layer (100 nm) as deposited and tungsten coated on top during FIB lamellar sample preparation for STEM analysis (left). Annealing experiments with varying temperature and dwell time (right)

Taking into account the sintering temperature of the composites investigated above, samples were first annealed at 1200 °C for various times as mentioned in the Figure 46. The X-ray diffractograms clearly show that already after 1 h all of the spinel phase disappears and only two main phases – CGO and Gd(Fe,Co)O<sub>3</sub>-perovskite are present. In case of lower annealing temperatures (Figure 47), the onset of Gd(Fe,Co)O<sub>3</sub>-perovskite phase in XRD pattern seems to occur at different dwell times such as a) at 1100 °C after 1 h, b) 1050 °C for 3 h and c) 1000 °C for 15 h. The three main phases – CGO, Co rich spinel, and Gd(Fe,Co)O<sub>3</sub> - perovskite are observed.

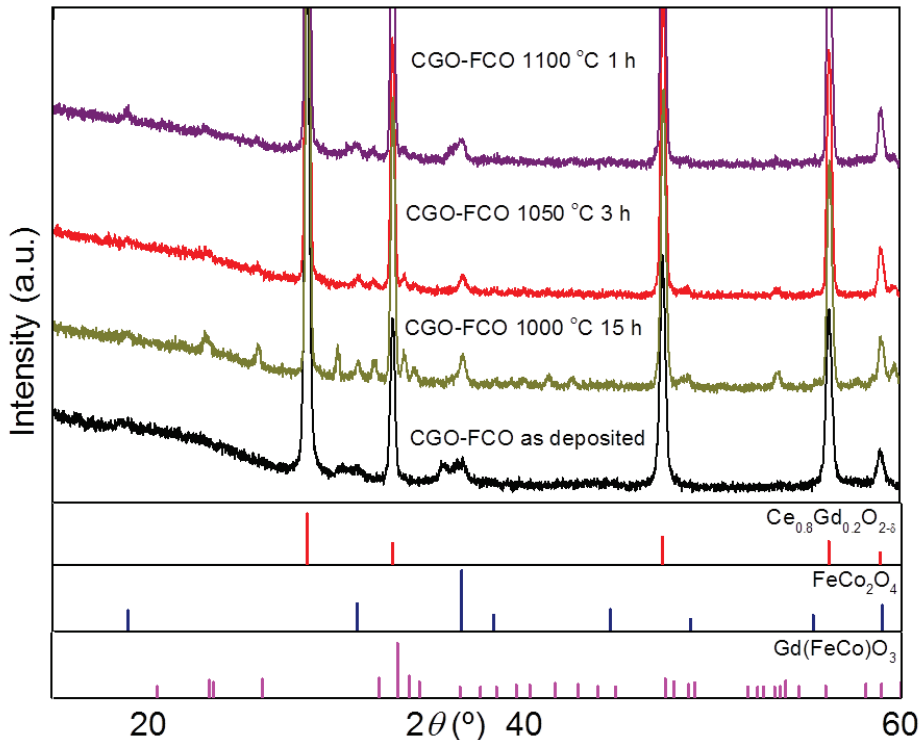


**Figure 47** Diffraction pattern measured on thin film samples after annealing at (a) 1100 °C 1 h (b) 1050 °C 3 h and (c) 1000 °C 15 h. The vertical lines indicate literature pattern from PDF database: CGO (red),  $\text{FeCo}_2\text{O}_4$  (blue),  $\text{Gd}(\text{Fe,Co})\text{O}_3$  (pink)

In case of the EDS mapping in STEM as shown in Figure 48, the onset of phase interaction can already be observed after 3 h of annealing time at 1000 °C. (Please note: Absent perovskite signals in the XRD pattern of samples being annealed shorter than 45 h can most likely be explained by the low incident angle in XRD leading to lower sensitivity for signals from phases at the film-substrate interface.) Figure 48 (a) depicts the broader area of the sample with few grains of spinel and perovskite phase non-homogenously distributed over the CGO substrate. This scarce distribution could attribute to contraction of the spinel layer associated with high reactivity of Fe cations with Gd in comparison to the Co cations at the annealing temperature. While Figure 48 (b) looks into one particular enlarged grain and the corresponding EDS mapping confirms the presence of Gd and Fe rich perovskite with traces of Ce and Co adjacent to

$\text{Fe}_2\text{CoO}_4$  spinel phase. Also due to non-uniformity of the coating thickness, the intensity of interaction may vary from sample to sample as observed by the STEM analysis. At elevated temperature obviously the Fe is preferentially removed from the spinel phase(s) forming the perovskite phase, leaving behind the Co-rich spinel phase.

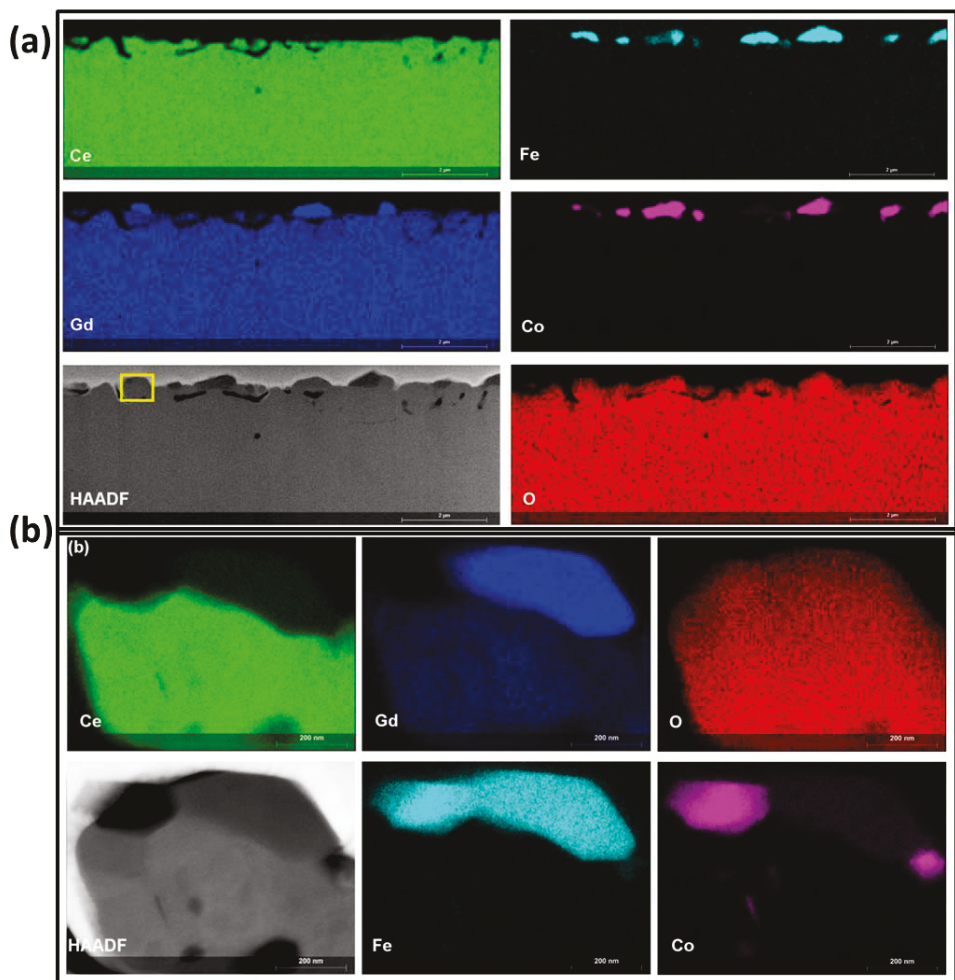
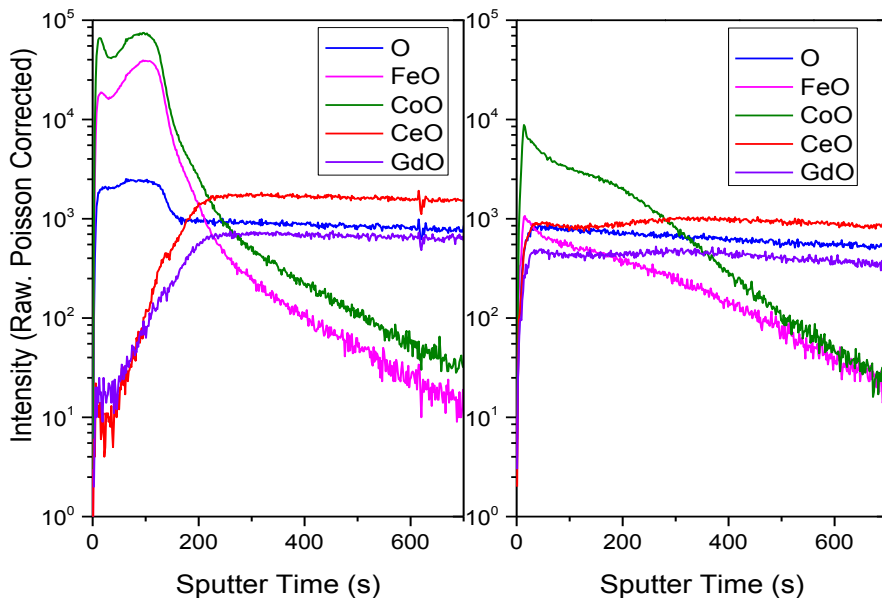


Figure 48 (a) EDS net count mapping of the 1000 °C 3 h (b) EDS mapping of enlarged image of yellow box area marked in HAADF image in (a).

## 4 Results and Discussion

Based on the XRD and STEM results it is evident that the perovskite is formed at 1000 °C and above, while the distribution of phases depends on the dwell time to a certain extent. Hence for investigation by SIMS (Secondary Ion Mass spectrometry) analysis, samples annealed at 1050 °C for 6h and their as deposited counterpart were chosen as shown in Figure 49. The profiling of both the samples to a penetration depth estimate of about 0.5  $\mu\text{m}$  (assuming 30  $\mu\text{m}$  per hour sputter rate) was carried out to observe the phase transition. The as deposited sample clearly separates the spinel phase by the FeO and CoO high intensity profiles dominating for a certain depth followed by CeO and GdO profiles representing the fluorite phase for the remaining depth of the analysis. However the annealed sample shows high intensity CoO profile for a certain depth, whereas the FeO profile is much lesser intensity proving its higher diffusivity in this material system. Moreover, GdO and CeO profiles now are present upto the surface of the sample.



**Figure 49** SIMS plot of as deposited (left) and 1050 °C 6 h annealed (right) samples.

The results support the former results leading to the conclusion that Fe is preferably extracted from the spinel phase forming a new perovskite phase rich in Gd and Fe with traces of Ce and Co. The remaining spinel phase in consequence is rich in Co.

#### 4.2.2. CGO-FCO Performance

##### Electrical Conductivity

Bar shaped samples of the individual phases and dual phase composite were prepared by uniaxial pressing and sintering at 1200 °C for 10 h for DC four point conductivity measurements between 600 and 850 °C. The total or electrical conductivity of the samples measured is plotted as a function of the exposed temperature, shown in Figure 50.

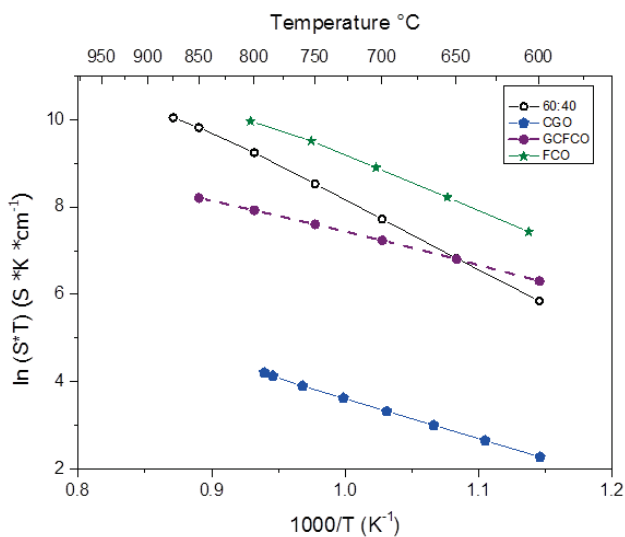


**Figure 50** Electrical conductivity of individual phases and dual phase composite 60 wt% CGO - 40 wt% FCO .

It is evident from the results that pure electronic conductor FCO shows the highest conductivity as electronic conductivity is usually 2 orders of magnitude higher than the ionic conductivity of pure ionic conductors. The total conductivity of CGO-FCO composite falls well below FCO indicating the influence of the two phase mixture proportion. The results also show that the total conductivity of the GCFCO perovskite is close to CGO-FCO composite. Thus, the perovskite phase can be assumed to contribute to the percolating network of the composite as MIEC or pure

## 4 Results and Discussion

ionic or electronic conducting phase. The GCFCO perovskite was subjected to permeation measurement to calculate the ambipolar conductivity of the sample. In this case there was negligible to zero oxygen flux measured. The partial substitution of  $Gd^{3+}$  by  $Ce^{4+}$  act as donor doping leading to a partial reduction of Fe and/or Co from 3+ to 2+ to the same extent. This would lead to low amount of oxygen vacancies and hence permeation, but the presence of  $B^{2+}/B^{3+}$ -couples enabling polaron hopping makes it a good electronic conductor (Maier '94, Ohnishi '08). Hence the measured electrical conductivity of GCFCO can be categorized as pure electronic conduction. Thus in case of CGO-FCO composite, combination of spinel and perovskite phase contributes to the electronic conductivity, while the fluorite phase takes care of the ionic transport through oxygen vacancies providing the oxygen flux.

### **Oxygen permeation measurements**

CGO-FCO permeation result was briefly discussed in section 4.1.1 along with other dual phase combinations and LSCF as a reference membrane. It was observed that the oxygen flux was almost half of LSCF membranes' performance which was attributed to surface exchange limitation. In most cases, only part of the surface of the dual phase membrane might be effective towards oxygen exchange. But on the contrary, the whole surface area of the single phase MIEC LSCF membranes are activated and not restricted only to the triple phase boundaries. Hence surface exchange limitation is countered by porous catalytic layer such as LSCF screen printed over the dense dual phase membrane surface. The screen printed LSCF layer ( $\sim 20 \mu\text{m}$ ) was dried at  $80 \text{ }^\circ\text{C}$  and co-fired with the membrane at  $1080 \text{ }^\circ\text{C}$  for 3 h to obtain a porous LSCF catalytic layer of  $\sim 10 \mu\text{m}$ . The additional porous coating facilitates the surface exchange, which results from an increase of the surface exchange area between gas and the membrane layer. LSCF proves to be an effective catalyst to eliminate the limitation of surface exchange (Balaguer '13) based on its well-known performance as SOFC cathode (Adler '04).

The oxygen permeation behavior of the composite was determined by oxygen permeation measurements using pellets with and without porous activation layers. In the case where the electronic conductivity is dominating as indicated in the electrical conductivity measurements, the ambipolar conductivity can be set equal to the ionic conductivity. Hence permeance is calculated from their  $O_2$  flux measurements, normalizing the impact of pressure gradient. The permeance of the sintered CGO-FCO pellet polished to a thickness of 1 mm is shown in Figure

51 as a function of temperature range 700 - 1000 °C. The change in activation energy between 850 °C and 900 °C indicates a change in the dominating transport process. The activation energy at high temperature (850 - 1000 °C) of  $E_A = 70$  kJ/mol can be attributed to the bulk transport, therefore to the ionic conductivity of CGO, supporting the assumption that this is the major permeation rate limiting process (Samson '14). At lower temperatures (650 - 850 °C), however, the activation energy is much higher, i.e. 140 kJ/mol, indicating rate limitations due to surface exchange kinetics.

In order to confirm the rate limiting processes, the permeance of an identical CGO-FCO pellet with porous LSCF activation layers of approx. 10  $\mu\text{m}$  thicknesses on both sides of the membrane was measured. In this case, the activation energy is 66 kJ/mol over the whole temperature range of 650-1000 °C. Furthermore, the permeance is also higher at high temperatures indicating that even at 1000 °C the permeation is mainly though not completely limited by bulk diffusion, but surface exchange kinetics still plays a certain role although minor in the overall transport process. Compared to a standard LSCF pellet of the same thickness, i.e. 1 mm, the permeance of the activated dual phase membrane is higher at temperatures below 850 °C due to the much lower activation energy. Considering the high permeation rates obtained by using thin supported LSCF membranes (Schulze-Küppers '14, Serra '13), the severe surface exchange limitation is overcome by extending the Triple Phase Boundary (TPB) in the membrane's microstructure.

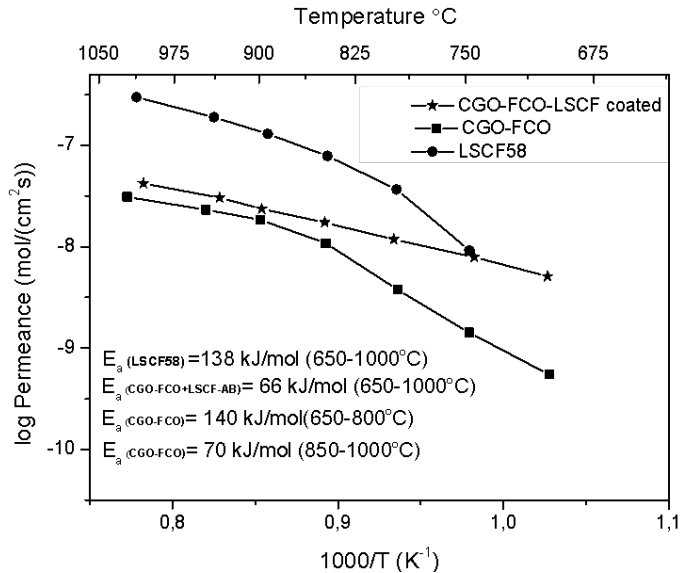


**Figure 51 Arrhenius plot as a function of permeance and temperature of the composite with and without porous LSCF coating**

Hence the surface limitation was minimized after both sides of membranes had been coated with LSCF porous layers. However, considering the reason for developing a stable dual phase membrane is the lack of stability in single phase LSCF membranes, LSCF catalytic layer has been used only to validate the presence of surface exchange limitation in the composite. In the future a suitable catalytic layer material replacing LSCF will be investigated in detail by Green-CC project partners.

### Varying Spinel content

The dual phase membranes investigated so far consisted of 60 wt% CGO and 40 wt% FCO, which is 54 and 46 vol%, respectively. Permeation tests revealed that the ionic conductivity is the limiting step in the bulk transport if surface exchange is facilitated by catalytic active porous coatings. Therefore, an increase in the CGO-content would be beneficial. On the other hand, the proportion of both phases in a dual phase composite must be high enough to form continuous phases in the bulk and surfaces, i.e. both phases need to reach a state of percolation (Sun '13). To reach the percolation threshold, the volume fraction of the minor phase is usually no less than 30% for dual-phase materials (Zhu '08).

**Table 10 CGO-FCO composite ratios investigated, in wt% and vol% for comparison**

CGO-FCO ratios in wt %	CGO-FCO ratios in Vol %
60:40	54:46
65:35	59:41
70:30	64.5:35.5
75:25	70:30
80:20	76:24
85:15	81.5:18.5
90:10	87.5:12.5

Nevertheless, this is not necessarily applicable for composites that tend to have phase interaction and grain boundary phases. The secondary phases formed are conducting, contributing to the overall percolating network of the composite impacting the oxygen transport. Hence, the spinel content is reduced from 40 wt% to as low as 10 wt% in the composite as shown in Table 10 for this investigation and powders were synthesized by the one pot Pechini process.

### **Microstructure analysis**

The XRD plots of the composites with varying spinel content are shown in Figure 52. The decrease in spinel content is evident from the decrease in intensity of the spinel peaks of the composites particularly at  $2\theta = 38^\circ$ .

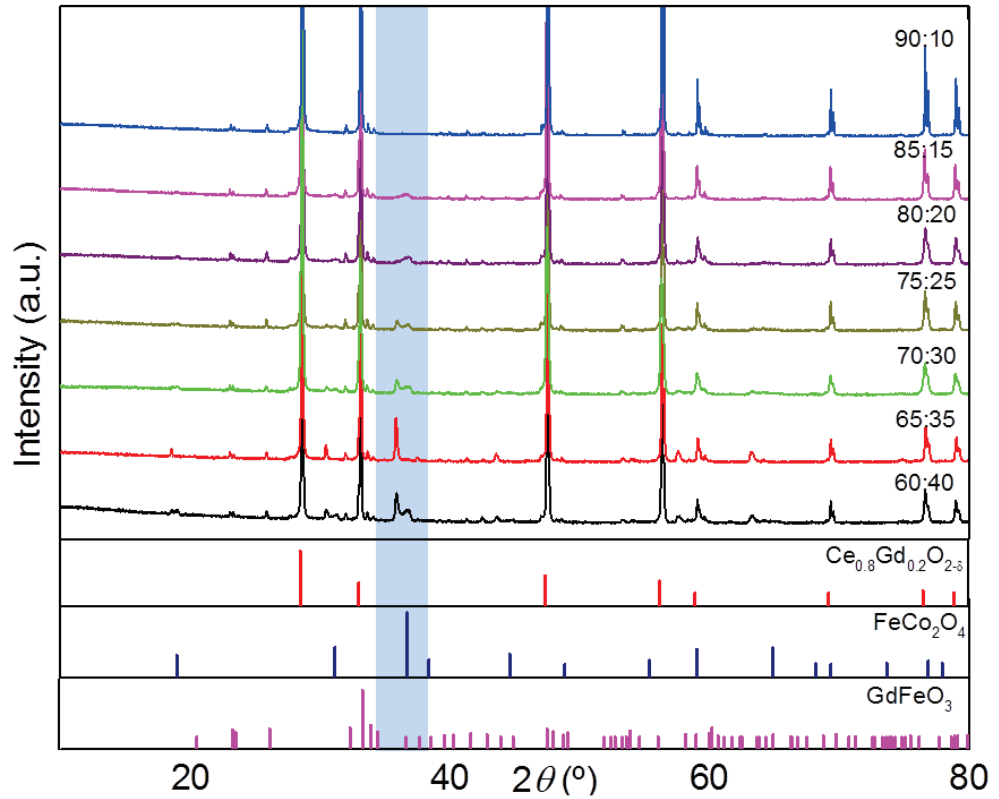


**Figure 52** XRD plot of the composites with varying spinel content from 40 wt% to 10 wt% sintered at 1200 °C for 10 h

In addition, the interesting observation is the presence of orthorhombic perovskite peaks in all the ratios indicating the secondary phase formation with as low as 10 wt% of spinel phase in the composite. These results are further supported by the SEM images as shown in Figure 53.

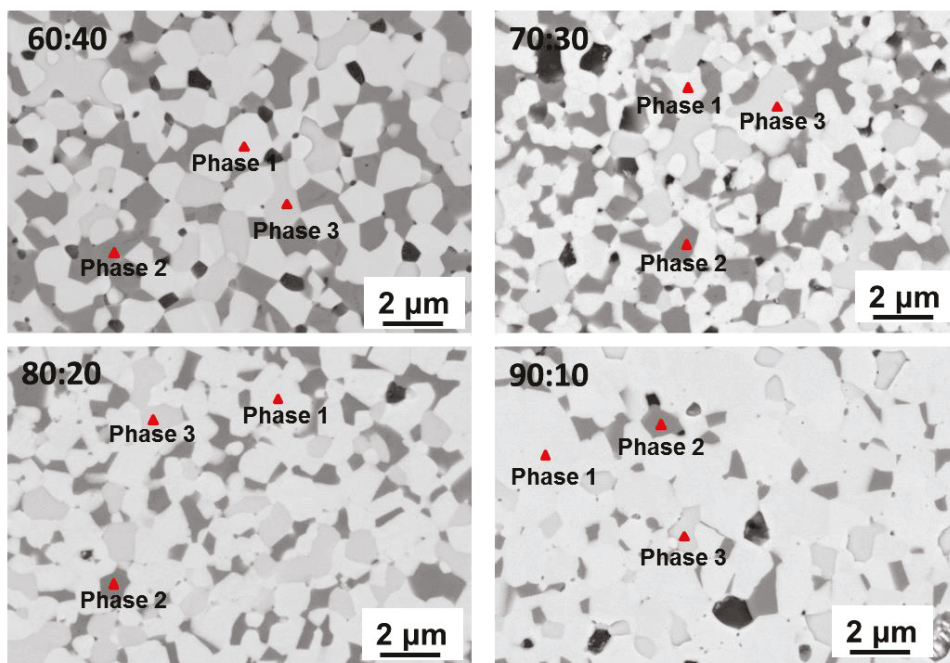


Figure 53 SEM images of CGO-FCO composites with ratios (in wt%) 60:40 (top left), 70:30 (top right), 80:20 (bottom left) and 90:10 (bottom right). Phase 1 – CGO, Phase 2 – FCO, Phase 3 – GCFCO.

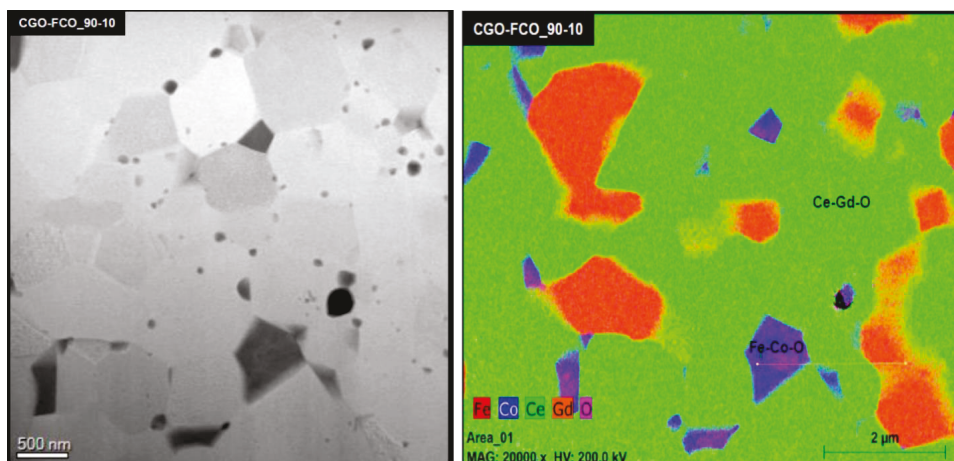


Figure 54 STEM-HAADF and EDS element mapping of CGO-FCO 90:10 ratio (in wt%) composite sintered at 1200 °C for 10 h.

## 4 Results and Discussion

The images show the presence of fluorite phase with decreasing distribution of the spinel phase corresponding to the ratio and the presence of GCFCO perovskite phase in all four cases (Lin '15). The phases were also verified by the EDX mapping of the samples. STEM-HAADF and EDS element mapping of 90:10 ratio composite was carried out with intention to investigate the detailed microstructure in case of spinel content as low as 10 wt%. Figure 54 shows that the grain boundary phase does not form in case of 90:10 ratio which was observed for 60:40 ratio sample and identified to be the rock salt phase. But the presence of GCFCO perovskite phase is clearly seen from the EDS element mapping image which also contributes to the electrical conductivity of the sample as a MIEC material.

### Electrical Conductivity

Bar shaped samples of varying spinel ratio composites were prepared and subjected to electrical conductivity measurement by four point DC method. The electrical conductivity results at 800 °C for the dual phase composite are compiled as a function of its FCO wt% content into one plot as shown in Figure 55 for direct comparison along with the individual phases of the composite as well.

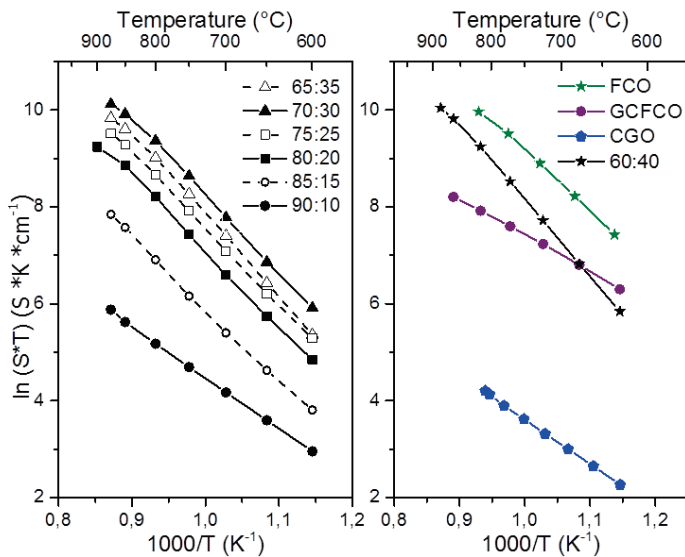
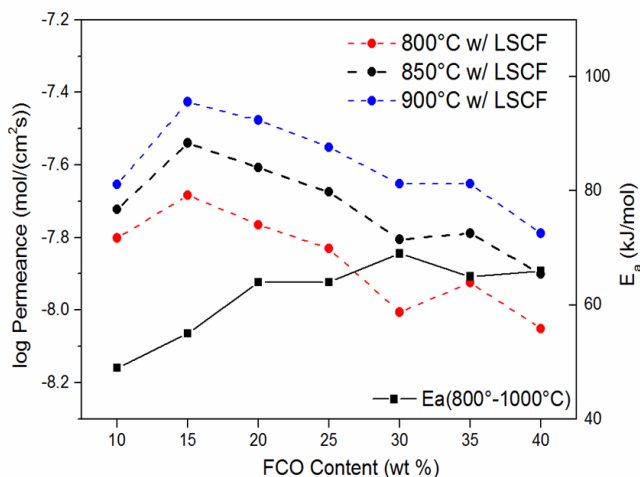


Figure 55 (a) Electrical conductivity of CGO-FCO composite with varying spinel content from 35 wt% to 10 wt%, (b) Electrical conductivity of individual phases and dual phase composite 60 wt% CGO - 40 wt% FCO.

The total conductivity of FCO is dominating as expected, followed by the reference 40 wt% sample and 30 wt% indicating that the electronic conductivity is still dominant in these composites too. The conductivity decreases consistently with decreasing spinel content down to 10 wt%. Interestingly lowest spinel content (90:10) sample still shows a value marginally above the electrical conductivity of pure CGO. This signifies the presence of a percolating network contributed by both electronic and ionic conductors even with as low as 10 wt% of spinel content.

### Oxygen permeation measurements

The composites with the varying spinel content were subjected to permeation measurements. The results showed that 15 wt% spinel content composite had the highest permeation rate compared to the rest of the ratios measured including the standard CGO-FCO 60:40 wt% ratio as shown in Figure 56.



**Figure 56** Plot as a function of Permeance for varying spinel content and their corresponding calculated activation energy between 800-1000 °C

In order to eliminate surface exchange limitation of the membrane, all the composites were screen printed with catalytic LSCF layers on both sides. The screen printed samples were post sintered at 1050 °C for 3 h replicating the same process as for the standard composite in the past. The oxygen permeance gradually increases with decrease in spinel content upto 85:15 which has the highest permeance of all the ratios. Then the permeance drops for 90:10 ratio indicating the

## 4 Results and Discussion

lack of necessary electronic conductivity that is required for efficient oxygen transport in the composite. Figure 56 includes the activation energy  $E_a$  of the varying ratio composites. From 20 to 40 wt% of spinel in the composite, the  $E_a$  is consistently above 60 kJ/mol indicating that the ionic conductivity of CGO is the rate limiting step. Below 20 wt% spinel phase the activation energy decreases, indicating a change in the limiting transport process, potentially electronic conductivity. Thus 15 wt% spinel content can be regarded as the appropriate proportion at which the limiting factor is shifting from ionic conduction to electronic conduction, but sufficient to provide the highest oxygen flux among the varying proportion of CGO-FCO composites. From the microstructure analysis of these composites, it is evident that the presence of GCFCO phase contribute substantially to the oxygen transport.

### 4.2.3. CGO-FCO Stability

#### Phase Segregation

In this section, phase segregation noticed in the dual phase composite after oxygen permeation measurements are investigated. The post-permeation measured samples were noticed to have different color shades on the surface of both sides. SEM Analysis revealed that there are large dark crystals on the surface at the high  $p_{O_2}$  side of the composite. While the argon feed side surface of the membrane showed clustered white grains widely distributed. The large dark crystals attribute to Fe and Co cations drift (spinel phase segregation) towards the high  $p_{O_2}$  side. This behavior is attributed to the segregation of the cations with enrichment of the faster cations (in this case Fe, Co cations are faster compared to Ce and Gd) at the high  $p_{O_2}$  side of the membrane (Belova '03, J. O. Hong '06, Martin '03). In general, transport works via cation diffusion in the FCO (cation deficient) spinel. The cation deficiency accelerates faster diffusion of Fe and Co cations in comparison to Ce and Gd cations. Additionally, Fe Co cation enrichment on higher partial pressure side can also explained by the Gibbs-Duhem relation that the gradient of oxygen chemical potential is not in balance with the chemical potential of the cations (Schlehuber '10). This segregating behavior of the cations might significantly impact long term oxygen permeation of the membrane since the percolating path of both oxygen ions and electrons eventually might be hindered by the enrichment of cations, if this is continued.

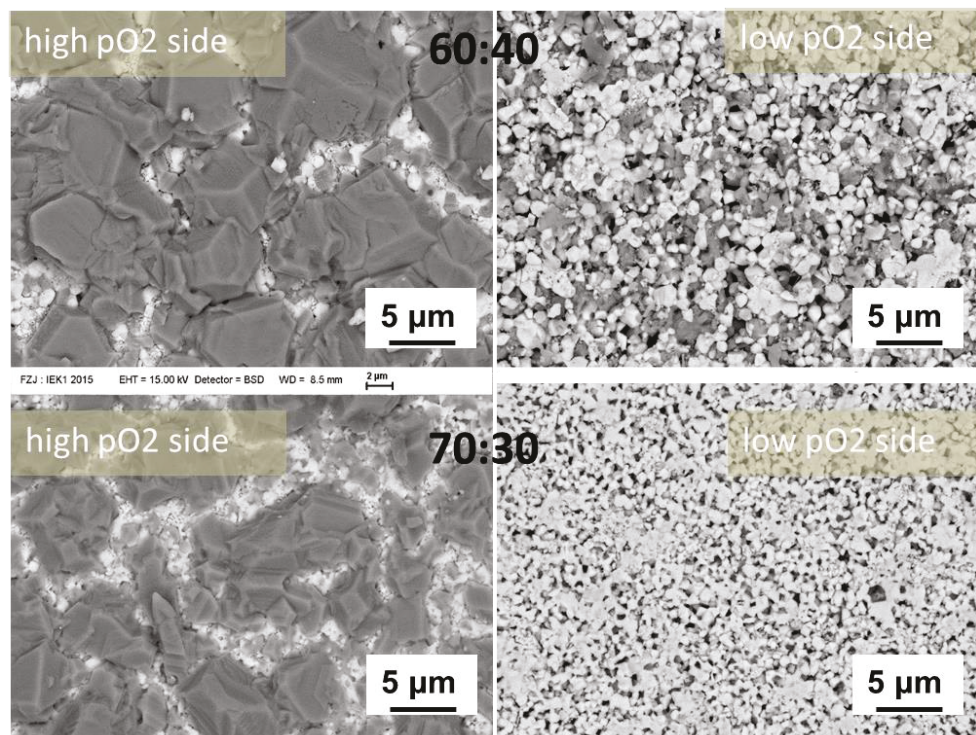


Figure 57 Surface images by SEM investigation of 60:40 and 70:30 ratio (in wt%) CGO-FCO composites post permeation measurement at temperature range 700 - 1000 °C with air/Ar gradient.

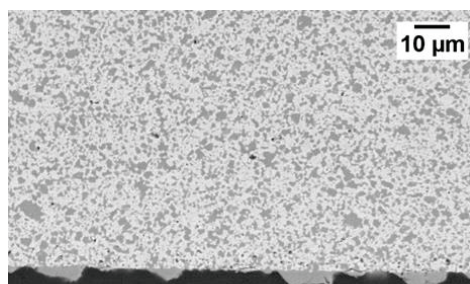
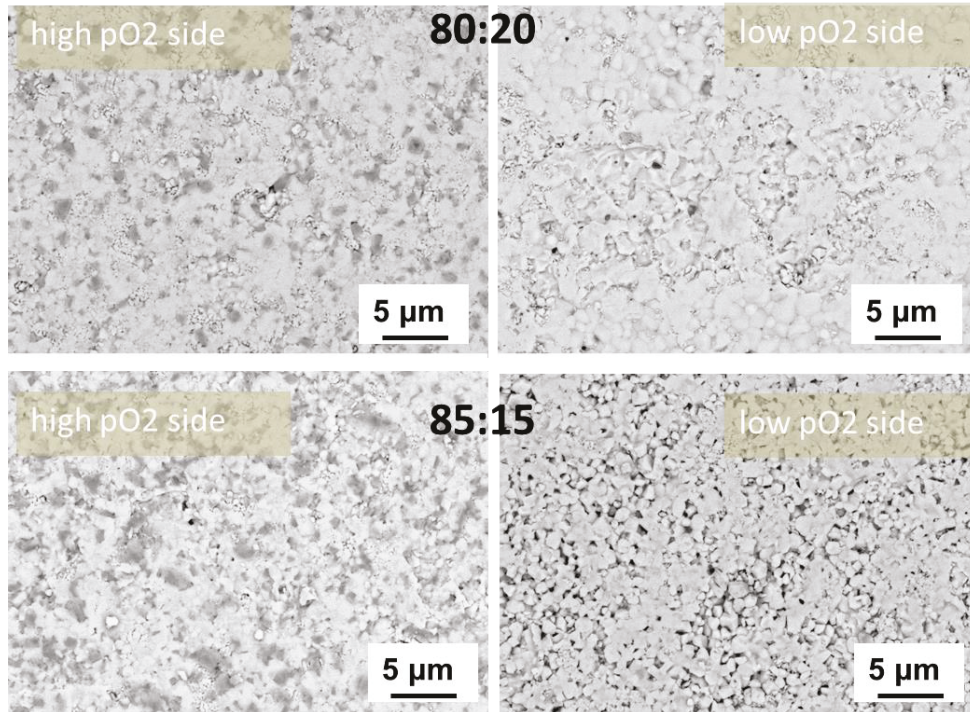


Figure 58 SEM image of the cross section on the feed side of 60 wt% CGO – 40 wt% FCO membrane post permeation measurement at temperature range 700 - 1000 °C with air/Ar gradient.

Thus all the CGO-FCO composites with varying spinel content from 10 wt% to 40 wt% were investigated for this behavior. Figure 57 shows the SEM images of surface on both high  $p_{O_2}$  side and low  $p_{O_2}$  side of the membrane for CGO-FCO 60:40 and 70:30 ratios that showed predominant segregation. Figure 58 shows the cross section of CGO-FCO 60:40 ratio on the feed side of the membrane after permeation measurement. The dark large grains are clearly seen in the image.



**Figure 59** Surface images by SEM investigation of 80:20 and 85:15 ratio CGO-FCO composites post permeation measurement at temperature range 700 - 1000 °C with air/Ar gradient.

Interestingly, CGO-FCO composites with lower spinel content (80:20 and 85:15) showed reduced segregation of cations at the high  $p_{O_2}$  side of the membrane as shown in Figure 59. Absence of enrichment on the surface in lower spinel content composites can be attributed to the phase interaction between CGO and FCO to form GCFCO perovskite phase which might slow down the movement of faster cations to the high  $p_{O_2}$  side. This additional advantage further supports the strategy to focus more on the lower spinel content in the CGO-FCO membrane development moving forward.

### Chemical Stability

Dual phase membranes require long term stability in presence of harsh atmospheres such as flue gas containing  $CO_2$ ,  $SO_2$ ,  $H_2O$ , dust and high pressure at operating temperature on application in

oxyfuel combustion. Thus stability testing in the presence of gases such as combinations of CO<sub>2</sub>, SO<sub>2</sub>, H<sub>2</sub>O and O<sub>2</sub> was investigated for high and low spinel content composites. Samples of the composites tested were:

1. Ce<sub>0.8</sub>Gd<sub>0.2</sub>O<sub>2-δ</sub> - FeCo<sub>2</sub>O<sub>4</sub> (60:40 wt%)
2. Ce<sub>0.8</sub>Gd<sub>0.2</sub>O<sub>2-δ</sub> - FeCo<sub>2</sub>O<sub>4</sub> (85:15 wt%)

Stability testing was strategically planned with varying combinations of gas mixtures as listed below;

1. Pure CO<sub>2</sub>
2. 250 ppm of SO<sub>2</sub> in CO<sub>2</sub>
3. 250 ppm SO<sub>2</sub> + 5 vol% O<sub>2</sub> in CO<sub>2</sub>
4. 250 ppm SO<sub>2</sub> + 5 vol% O<sub>2</sub> + 2.5 vol% H<sub>2</sub>O (saturated at room temperature) in CO<sub>2</sub>

The important reason to choose this concentration level of each gas is based on the information collected from industries who are project partners in Green-CC project partially funding this PhD research work. There are lots of publications available concerning the impact of CO<sub>2</sub> on OTMs, but very little on impact of SO<sub>2</sub> and H<sub>2</sub>O gases though these gases also constitute to recirculated flue gas stream in power plants (Engels '11). The order of mixing these gases and repeating the experiment would help to identify the impact of each gas element on the stability of the membrane.

The samples were annealed in the furnace at 850 °C for 16 h allowing the different gas mixtures to flow through for the dwell time of the furnace. These experiments are considered as preliminary tests that would enable strategic planning of long term tests combined with the permeation measurements. The tested samples were then characterized by SEM along the surface to investigate the stability in these gaseous atmospheres.

The SEM images (Figure 60) show the surface of the CGO-FCO 60:40 sample before and after exposure to the gas mixtures. In case of pure CO<sub>2</sub> and 250 ppm of SO<sub>2</sub> in CO<sub>2</sub>, the samples do not show any variation in comparison to the reference indicating the stability of the composite in the pure SO<sub>2</sub>, CO<sub>2</sub> gas mixture. Upon inclusion of 5 vol% O<sub>2</sub>, the spinel phase (dark grey) grains seem to have segregated to the surface in comparison to the fluorite phase (bright/white) grains in addition to flakes of sulfur as identified by EDS of the sample. Lastly, passing the gas mixture through a water bubbler adds ~ 2.5 vol% H<sub>2</sub>O (Saturated steam at room temperature calculated), worsens the segregation of the cations (Fe, Co Spinel). Sulfur containing flakes due to possible

## 4 Results and Discussion

interaction of condensed  $\text{SO}_2$  with dust and/or galled steel debris inside the setup observed in the SEM image (Figure 60-4). In order to further investigate this scenario, both sides of the membrane surface after exposure to 250 ppm  $\text{SO}_2$  + 5 vol%  $\text{O}_2$  + 2.5 vol%  $\text{H}_2\text{O}$  were analyzed in SEM as shown in Figure 61.

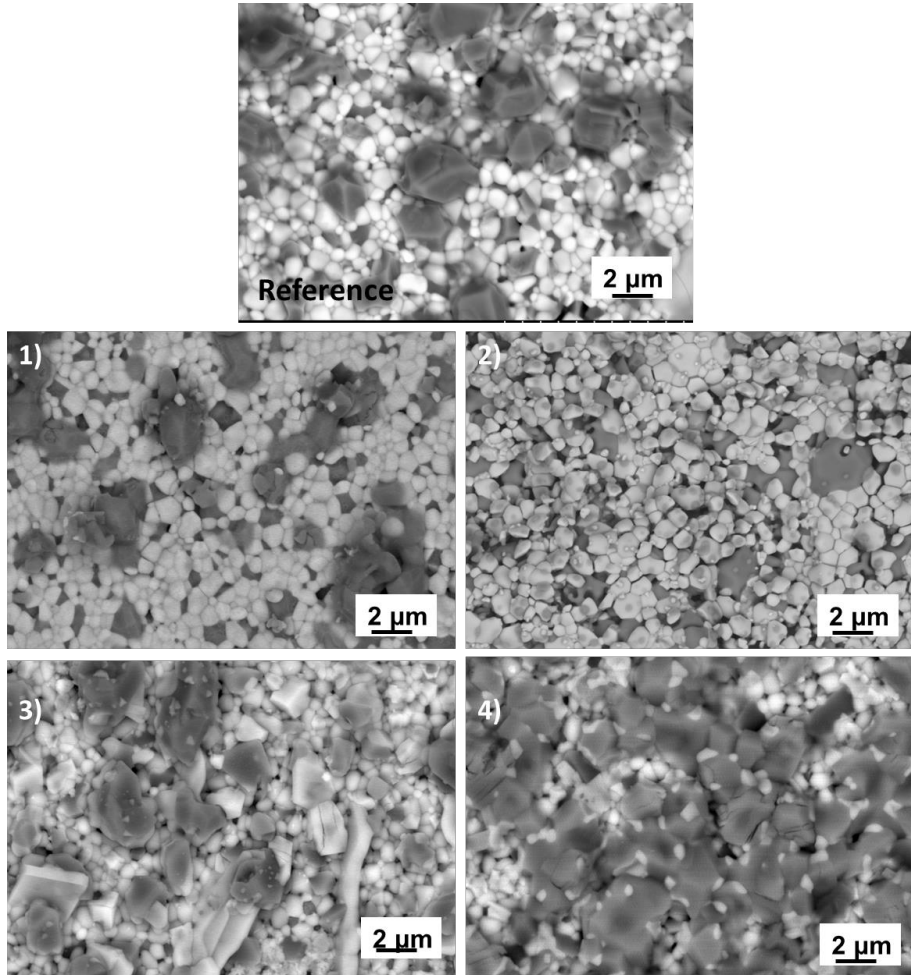


**Figure 60 SEM images of CGO-FCO 60:40 composite before ( reference) and after exposure to 1) Pure  $\text{CO}_2$  2) 250 ppm of  $\text{SO}_2$  in  $\text{CO}_2$  3) 250 ppm  $\text{SO}_2$  + 5 vol%  $\text{O}_2$  in  $\text{CO}_2$  and 4) 250 ppm  $\text{SO}_2$  + 5 vol%  $\text{O}_2$  + 2.5 vol%  $\text{H}_2\text{O}$  (saturated at room temperature) in  $\text{CO}_2$ .**

In these back scattered images, the spinel grain shows the tendency of segregation as observed in the permeation tested sample. The presence of 5% O<sub>2</sub> + 2.5% H<sub>2</sub>O might lead to different oxygen activity at the surface in comparison to the bulk sample possibly causing a gradient similar to the case of permeation measurement causing the phase segregation. EDX mapping of the composite on side a, is shown in Figure 62. From the mapping, it can be noticed that the Co rich spinel grains are predominantly visible and are mapped along with sulfur mapping. The back scattered image portrays the layered distribution of sulfur containing flakes on spinel grains segregated on the fluorite grains. The flakes are visible independent of spinel and fluorite grains eliminating the probability of sulfur interaction with the phases of the composite.

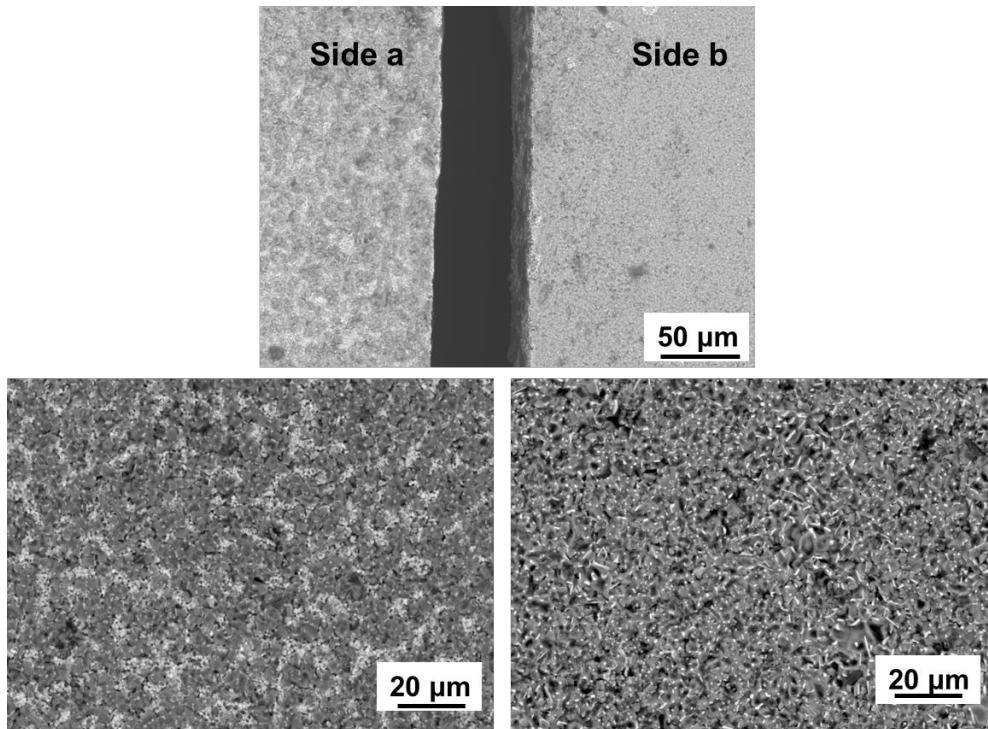
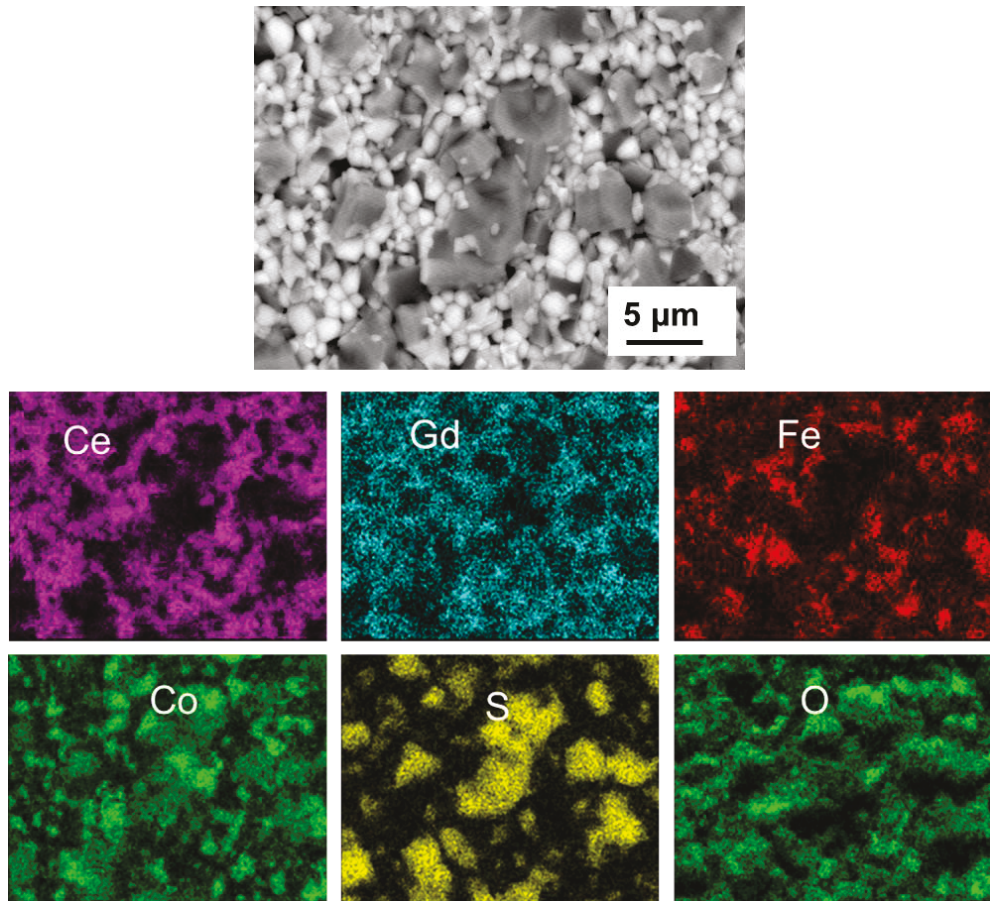
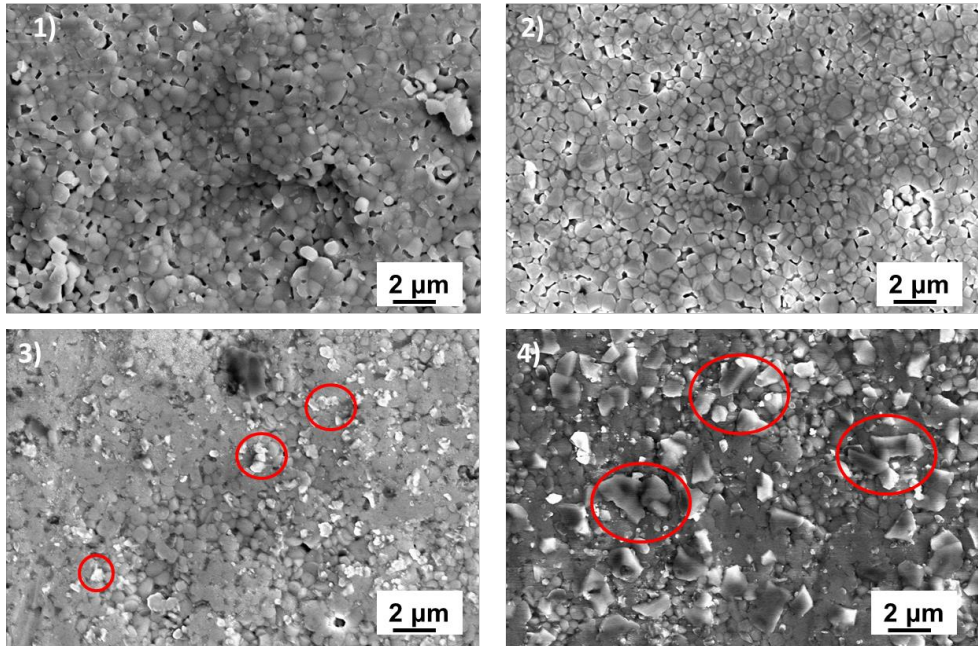


Figure 61 SEM images of 60 wt% CGO – 40 wt% FCO composite both sides of the membrane after exposure 250 ppm of SO<sub>2</sub> in CO<sub>2</sub> + 5% O<sub>2</sub> + 2.5% H<sub>2</sub>O at 850 °C for 16 h



**Figure 62 EDX mapping of 60 wt% CGO – 40 wt% FCO composite after exposure 250 ppm of  $\text{SO}_2$  in  $\text{CO}_2 + 5\% \text{O}_2 + 2.5\% \text{H}_2\text{O}$  at  $850\text{ }^\circ\text{C}$  for 16 h**

The experiments were repeated for 85:15 wt% CGO-FCO samples as well to determine their behavior under the similar conditions. Figure 63 shows the SEM surface images of the 85:15 CGO-FCO samples after exposure to the four gaseous mixtures during the annealing process for 16 h in a tube furnace. The SEM images in this case do not show any obvious cation segregation on the surface as observed in 60:40 ratio post treated samples. Nevertheless, addition of 5 vol%  $\text{O}_2$  marks the presence of sulfate flakes and the condition intensifies with 2.5 vol%  $\text{H}_2\text{O}$  inclusions, similar behavior to that observed on the 60:40 wt % ratio samples.



**Figure 63** SEM image of 85 wt% CGO – 15 wt% FCO composite after exposure at 850 °C for 16 h 1) Pure CO<sub>2</sub> 2) 250 ppm of SO<sub>2</sub> in CO<sub>2</sub> 3) 250 ppm SO<sub>2</sub> + 5 vol% O<sub>2</sub> in CO<sub>2</sub> and 4) 250 ppm SO<sub>2</sub> + 5 vol% O<sub>2</sub> + 2.5 vol% H<sub>2</sub>O (saturated at room temperature) in CO<sub>2</sub>. Flakes marked in red circles

The main observation is the sulfur containing flakes formation on the surface of both compositions of CGO-FCO composite on exposure to SO<sub>2</sub> and CO<sub>2</sub> gases in presence of O<sub>2</sub> and H<sub>2</sub>O. But these flakes are not identified as sulfates by interaction with the phases of the composite. Thus it can be stated that both these dual phase composites are stable in these conditions. However, the surface level sulfur containing flakes accumulation over a long run might contribute to adverse effect on the effectiveness of the oxygen transport, hence long term tests might shed light on such speculations. It is important to consider that these are specific experiments where these flakes may be attributed to interaction of SO<sub>2</sub> with dust or galled steel debris in the presence of O<sub>2</sub> and H<sub>2</sub>O. Therefore these preliminary results will be used to strategically plan long term stability testing experiments in the future. As a matter of fact power plant contains dust (e.g. fly ash) in flue gas (including debris) which has to be included in long term stability test combined with permeation measurements as it has not been reported or investigated yet (planned by Green-CC project partners).

### High pressure permeation measurement

High pressure is another attribution to the harsh ambience when subjected to power plant application; however the pressure is not fixed. Steam power plants are operated at atmospheric pressure. The air pressure for the membrane comes from the necessary driving force since the atmospheric sweep shall be enriched in O<sub>2</sub> up to 30%. Thus the pressures discussed are between 5 and 20 bar and are a free parameter in the overall efficiency/cost optimization.

The samples were subjected to He leak test to ensure they are gas tight for permeation measurements. The gas tight 85:15 samples (dense without leaks at the sealed edges or surface of measurement) were subjected to 2 experimental cycles at the operating temperature of 850 °C. In GREEN-CC project, pressure of 5 bar (max 10 bar) is the preferred testing parameter. Thus preliminary high pressure application up to 5 bar for oxygen permeation measurements were carried out at ORNL.

Unfortunately 60:40 samples with traces of micro-cracks were not gas tight for this high pressure measurement.

1. 85:15 sample coated with LSCF on both sides tested, Operating temperature – 850 °C, Pressure – 5 bar, dwell time – 17 h
2. 85:15 sample coated with LSCF on both sides tested, Operating temperature - 850°C, Pressure - ~2.5 bar ( Weld leak at the feed side hindering the control of high pressure)
  - a. Feed gas: Air, dwell time ~ 12 h
  - b. Feed gas: Air+ 250 ppm SO<sub>2</sub>+CO<sub>2</sub>+5%O<sub>2</sub>, dwell time ~ 5 h
  - c. Feed gas: Air, dwell time ~ 55 h

The weld leak in the experiment 2 made control of pressure at 5 bar not possible. Thus only 2.5 bar of pressure was possible on the feed side. The oxygen permeation of the samples measured is plotted versus the dwell time as shown in Figure 64. The flux values are compared to 85:15 sample measured in IEK-1 (marked as Atm. Pressure in the plot) using quartz setup without pressure influence and 50 ml/min flow rate of Ar on the sweep side. Experiment 1 (5 bar - green) is considered as the perfect run with no complication during the test in comparison to the other experiment. The flux values for experiment 1 (5 bar) is almost 4 folds higher than the measurement conducted with atmospheric pressure (1 bar - purple). In case of experiment 2 (2.5 bar - red), the inclusion of 250 ppm SO<sub>2</sub>+CO<sub>2</sub>+5%O<sub>2</sub> gas mixture on the feed side for 5 h (blue

dotted circle area), consequently causes the drop of flux for the same time. Then the flux value rises back to a slightly lower value for rest of the experiment with air as the only feed gas. This reduction of flux value after change of feed gas and back can be attributed to the competitive adsorption of the  $\text{CO}_2$  and  $\text{O}_2$  on the membrane surface (Serra '13).

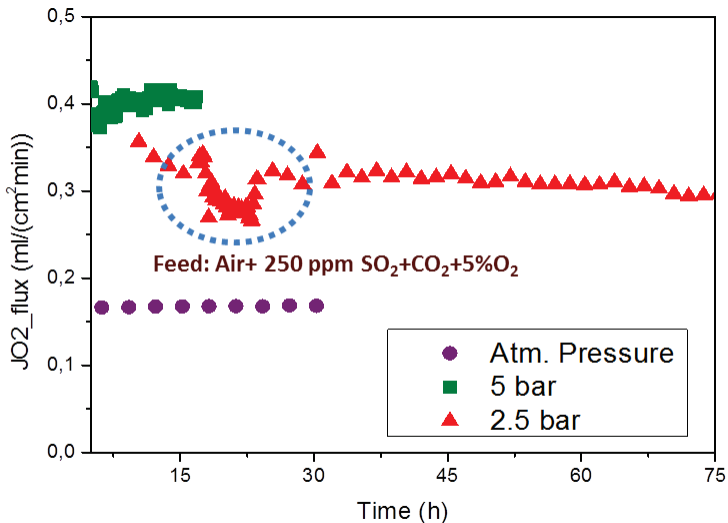


**Figure 64** Oxygen flux of the 85 wt% CGO – 15 wt% FCO with LSCF active layer. Atm. Pressure plot is measurement from IEK-1 setup at 1 bar, 2.5 and 5 bar plots are measured at ORNL. Blue dotted circle denote change of feed gas to air+ 250 ppm  $\text{SO}_2+\text{CO}_2+5\%\text{O}_2$  for 5 h.

The results obtained with 2.5 bar pressure also point to the influence of the partial pressure gradient in agreement with the results of 5 bar pressure experiment that the oxygen flux increases with increasing oxygen pressure gradient. Thus it can be concluded that, the oxygen flux is influenced by the driving force of partial pressure gradient in improving the oxygen permeation. Additionally these experiments also indicate the mechanical stability of the membrane to withstand the air pressure up to 5 bar on a 10 mm diameter free standing membrane area for a certain period of time. Moving forward similar experiments will be set up by Green-CC project partners to facilitate long term high pressure applied oxygen permeation measurements.

### 4.3. Processing and Microstructure Optimization

On model samples it has been proven that, CGO-FCO composite so far are promising oxygen transport membranes with good stability in harsh conditions. The complete investigation of the membrane was carried out using Pechini synthesised powder and conventional sintering process. In order to upscale the membrane fabrication technology, large scale powder synthesis routes have to be explored as pechini method is only feasible for lab scale powder synthesis. On the other hand, conventional sintering process has proven to be efficient in obtaining dense membrane samples, however it is worthwhile to experiment alternate densification techniques such as pressure induced sintering methods that are time efficient as well. These methods are also helpful to understand their influence over microstructure and oxygen flux performance of the membrane. Therefore, in this section large scale powder synthesis routes and pressure driven high temperature sintering processes are investigated. Moreover, an important milestone of upscaling membrane development technology is manufacture of supported asymmetric membranes by sequential tape casting process. Thus tape casting slurry and sintering profile optimization are extensively discussed in asymmetric membrane by tape casting section.

#### 4.3.1. Alternative Powder Synthesis

85:15 wt% CGO-FCO composite has been chosen for up scaling of powder production due its highest oxygen flux compared to other investigated compositions. Pechini powders with their high surface area and small primary particle size are not optimal for scale up (Cousin '90). Hence, to establish a suitable synthesis process, two alternative powder production routes were investigated. Firstly 85:15 wt% CGO-FCO was synthesized by conventional solid state reaction. These mixed powders are referred as CGO-FCO 85:15 SSR as the reactive sintering of the pressed pellets ["solid state reaction (SSR)"] results in the same phases as for Pechini synthesized composite. Secondly, powder synthesis via spray pyrolysis (powders are referred as CGO-FCO 85:15 SP) was also considered to manufacture powders with small primary particles for good percolation in an adequate batch size. Table 11 details the advantages and disadvantages of both upscale powder production routes in comparison to pechini process.

**Table 11 Overview of the different powder processing methods with pros and cons of each method listed.**

	<b>Pechini</b>	<b>SSR</b>	<b>Spray Pyrolysis</b>
<b>Specific surface area</b>	- high	+ low	- very high (needs to be optimized)
<b>Potential for up scaling powder production</b>	- low (small batch size)	+ good (if raw materials are available in needed microstructure and grade)	Medium (all nitrate salts available are expensive)
<b>Availability / batch size</b>	- small batches (~50 g)	+ good (raw material commercially available) + kg batch size possible + low cost	+ good (raw materials commercially available) + process in kg batch size available at IEK-1

**Table 12 PSD and Specific surface area of powders by different synthesis route**

Powder process	Fluorite (wt %)	Spinel (wt %)	PSD in $\mu\text{m}$			Specific surface area ( $\text{m}^2/\text{g}$ )	Calcination temperature $^{\circ}\text{C}$
			D10	D50	D90		
Pechini	85	15	0.52	0.71	0.96	8	700
SSR	85	15	0.47	0.62	0.82	7	-
SP	85	15	11.09	23.46	45.30	9	700

The powders synthesized by the three routes are compared based on their particle size, specific surface area as shown in Table 12. The table indicates high particle size distribution of the SP powders which is not very advantageous for tape casting process. The SEM images of the SP powders also show (Figure 65) the grain morphology and high level of agglomeration. Hence before introducing this powder for tape casting, the particle size distribution and specific surface area need to be optimized. One option would be subjecting the powder to additional milling step to break the agglomerates and reduce the particle size distribution as needed. The other option would be, calcining the powder at a higher temperature to influence the particle size distribution and surface area of the powder.

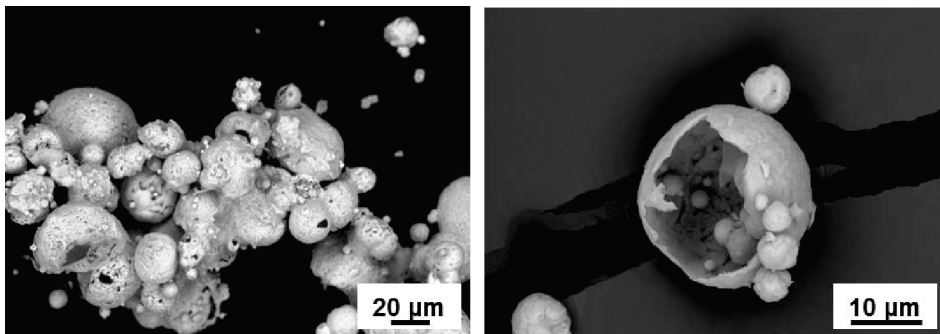


Figure 65 SEM images of SP (spray pyrolysis) synthesized powder.

The sintered dense pellets obtained from powders of different synthesis routes are compared for their microstructure and oxygen flux measurements. The formation of the desired phases takes place only during the final sintering step in case of CGO-FCO 85:15 SSR samples. The XRD plots indicate that in all three cases the desired phases are formed with identical peaks throughout the measurement range (Figure 66).

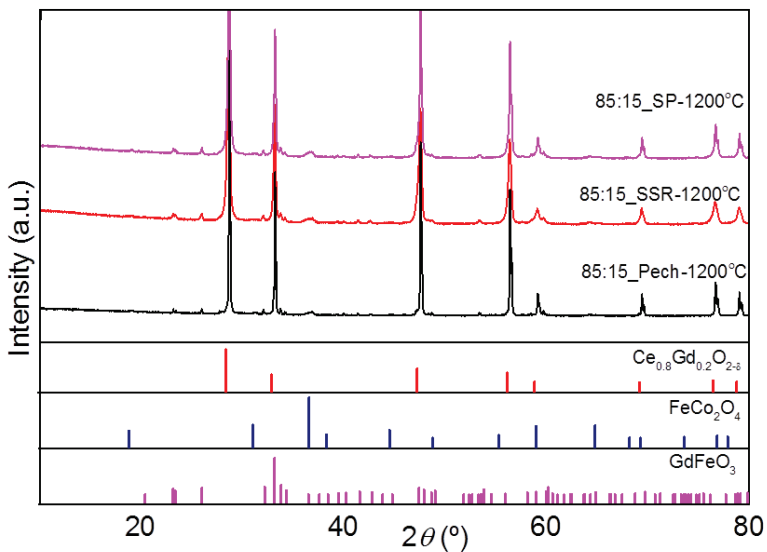
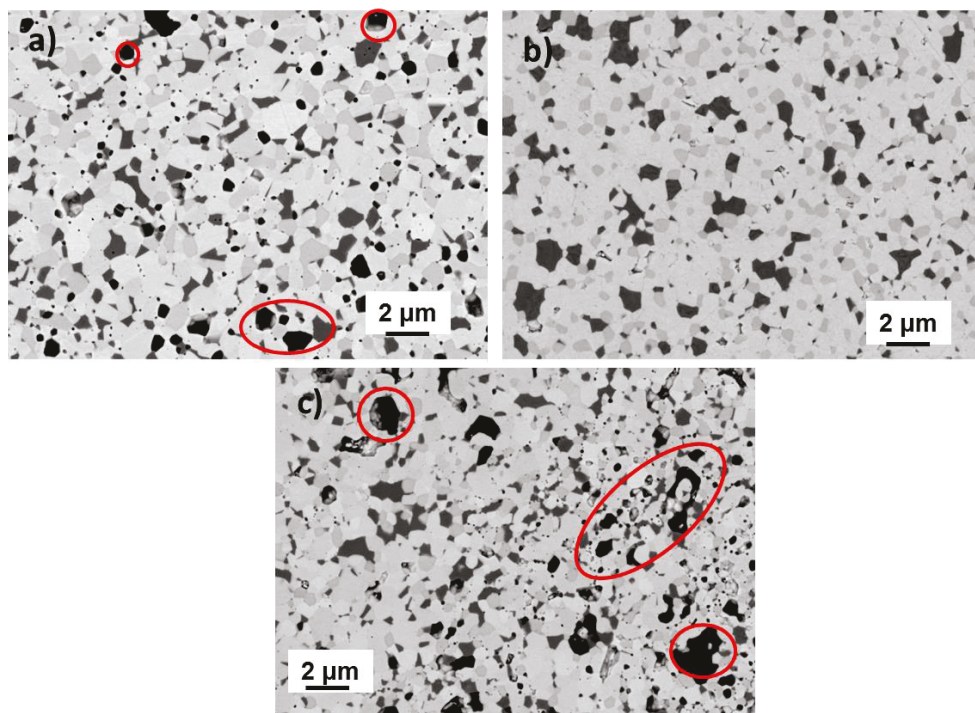


Figure 66 XRD scan of CGO-FCO 85:15 samples sintered at 1200 °C for 10 h. Powders were synthesized by Pechini, SSR and SP route as marked.

Due to the change of the powder synthesis, a change in the membranes' microstructure is observed as shown in Figure 67 by SEM images of sintered (1200 °C, 10 h) membranes in all 3 cases.



**Figure 67** SEM images of the cross sectioned sample, sintered at 1200 °C for 10 h, made from a) Pechini powder, b) “mixed powder (SSR)” and c) Spray pyrolysis (SP). (some pores are marked in red circles to distinguish from spinel phase)

Sintered pellet of Pechini route show a fine distribution of the different phases with minimal closed pores (~98 % relative density). The SSR route sample is completely dense (>99% relative density) with dark (Fe-Co- containing spinel) phase that appear coarser in comparison to Pechini and SP route samples. While the SP route (not milled powder) sintered sample (~93% relative density) shows large closed pores throughout the sample, which can be attributed to the high level of agglomerated particles shown in Figure 65. The sintered pellets of Pechini, SP and SSR

## 4 Results and Discussion

route powders are compared based on their functional property quantified by oxygen permeation measurement. To facilitate surface exchange, both membrane sides were screen printed with a porous layer of a mixed electronic-ionic conductor (LSCF58). The membrane thickness was 1 mm in all three cases and the measurement took place under an air/argon gradient.

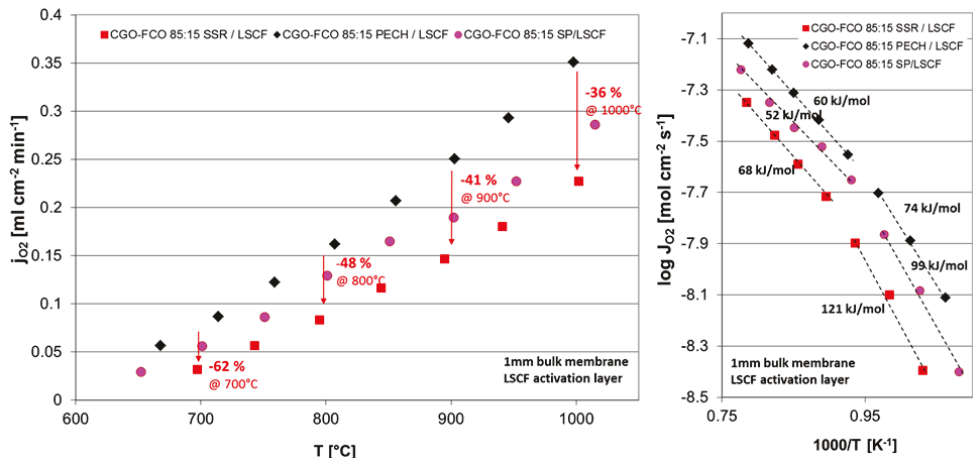


**Figure 68 Oxygen flux (left) and Arrhenius plot of the oxygen permeability (right) through 1 mm CGO-FCO 85:15 membranes activated on both sides by porous LSCF layer, under air/argon gradient.**

The result shows a decrease in oxygen permeation of 36 % at 1000 °C for the SSR route membrane compared to the Pechini route membrane, while SP route membrane performed in the mid range between the other two (Figure 68 left). This percentual decrease in flux becomes larger with decreasing temperature due to the higher apparent activation energy of the SSR membrane below 800 °C (Figure 68 right). Above 800 °C the activation energy is almost similar for all membranes, indicating the ionic conductivity as limiting factor for oxygen transport. At lower temperatures, the higher activation is mainly attributed to the surface exchange limitation albeit active layer on both sides. The lower permeation or relative higher activation energy of both SP and SSR route membranes in comparison to pechini can be reasoned as possibly due to higher tortuosity of the ionic conducting phase. The good distribution of the two phases apparently has a positive effect on oxygen permeation, as seen for the Pechini powder samples. Therefore, the coarser spinel phase and its distribution in SSR route membrane may be

speculated to limit the electronic conductivity for oxygen transport. On the other hand, the large closed pores of SP membrane are believed to impact the tortuosity and hence the efficiency of the oxygen transport.

Summarizing this alternative powder synthesis section, SSR powder provides the dense packing and good oxygen permeation in comparison to SP powder making it the most suitable option for upscaling membrane manufacture technology. Nevertheless, SP powder with suggested optimization options could be an alternative as well which will be focussed in the future research work of this project.

### 4.3.2. Alternative Sintering techniques

Albeit proven success with the conventional sintering of CGO-FCO membranes, the process is time consuming. Additionally, the scientific motivation behind investigation of these alternative sintering techniques is, to alter the microstructure and understand its influence on the oxygen flux of CGO-FCO membrane. Though GCFCO perovskite phase has proven to not hinder the oxygen permeation, an effort to restrict the membrane from undergoing phase interaction and secondary phase formations can prove to be beneficial. Also making sample without GCFCO phase could also help to clarify its influence by comparison with the conventionally sintered sample. Thus alternative densification techniques were explored, considering the possibility and opportunity available at IEK-1 to experiment pressure and electric field assisted sintering techniques. 60 wt% CGO - 40 wt% FCO composition was used for this portion of the investigation to obtain dense dual phase membranes.

#### Hot pressing of $\text{Ce}_{0.8}\text{Gd}_{0.2}\text{O}_{2-\delta}$ - $\text{FeCo}_2\text{O}_4$

##### a) Graphite die

Hot pressing experiments were carried out using a graphite die at 50 MPa, 1200 °C for 1 h under argon atmosphere. Two different approaches of sample preparation were considered. 1) 13 mm diameter pre-pressed sample and 2) 21 mm diameter pre-sintered (950 °C for 20 h) sample. In case of **pre-pressed pellet**, the hot pressed sample melted on to the graphite die, the sample had to be cut from the die using a saw blade. Thus the sample was cross sectioned and the SEM images of dense dual phase membrane with homogeneous distribution of phases are seen in Figure 69.

#### 4 Results and Discussion

The SEM image also shows the presence of micro cracks throughout the sample. EDX analysis indicate the presence of CGO and Fe, Co metallic phase, the reduced metallic phase is the outcome of reducing Ar atmosphere ( $p(\text{O}_2) \sim 10^{-5}$  bar) and the use of graphite die for hot pressing.

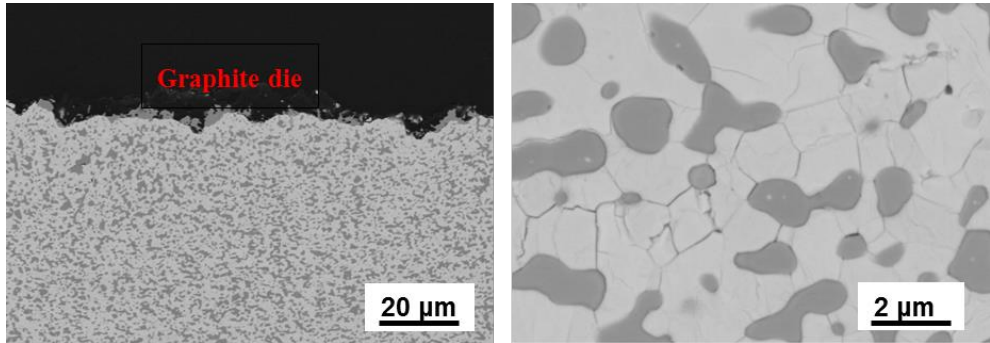


**Figure 69 SEM images of pre-pressed 60 wt% CGO – 40 wt% FCO sample after hot pressing at 50 MPa, 1200 °C for 1 h in argon.**

In case of **pre-sintered pellet**, Figure 70 a) and b) are the images of pre-sintered sample with and without graphite residue at the end of the hot pressing process. This hot pressed sample had reduced in thickness up to 0.5 mm compared to its pre-sintered thickness of ~1.4 mm. The diameter of the pellet had increased from 18 mm to ~ 21 mm after the hot pressing in a graphite die with punches size 20 mm.



**Figure 70 Pre-sintered 60 wt% CGO – 40 wt% FCO pellet hot pressed at 50 MPa, 1200 °C for 1 h in Ar atmosphere a) polished to remove b) the graphite residue that had attached to the pellet.**

The sample had thicker edges surrounding the punch of graphite die as it exceeded the size by 1 mm and looked very similar to pre-pressed sample after hot pressing. This behavior can be

attributed to the creep of the membrane although CGO's creep behavior is very low. Creep properties lower when Co is doped to ceria but CGO-FCO dual phase membrane is not clearly known (Lipińska-Chwałek '15). However, the combination of high pressure and temperature in reducing atmosphere could induce creep behavior earlier than expected. Figure 71 shows the XRD plot of the pre-pressed and pre-sintered samples (polished to remove the graphite residue) after hot pressing. The plot shows the presence of stable fluorite phase (CGO), while the spinel phase decomposed into Fe, Co metallic phase. The results are very much similar for both hot pressed samples. It is also clear that carbon traces are present after polishing the sample, but no hint on interaction with carbon forming any carbonate was observed.

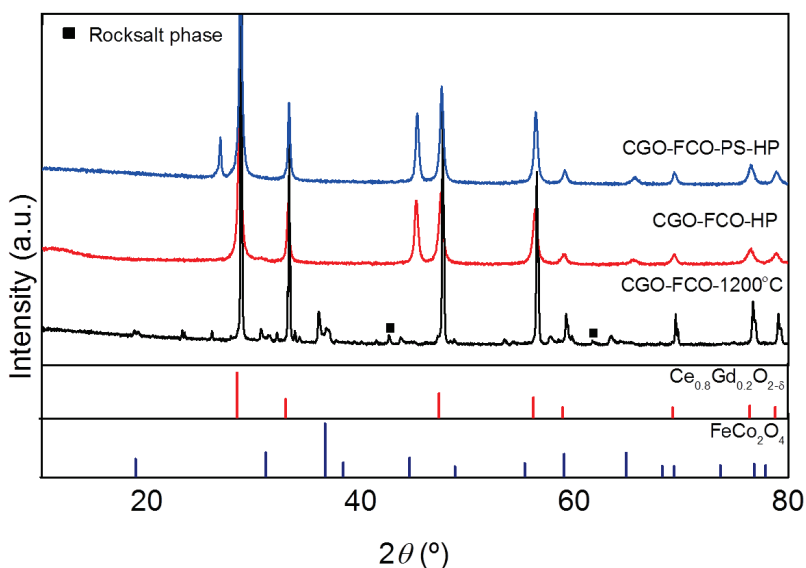


**Figure 71** XRD plot of 60 wt% CGO – 40 wt% FCO pre-pressed and pre-sintered (950  $^{\circ}$ C for 20 h) pellets, subjected to hot pressing at 50 MPa, 1200  $^{\circ}$ C for 1 h in argon atmosphere using graphite die are compared to conventional sintered sample. Samples differentiated by marking PS for pre-sintered and HP for hot pressing

Figure 72 shows the SEM images of pre-sintered pellet after hot pressing. The two phases present confirm the 2 phases identified by XRD analysis. Interesting observation is the dark grain boundary of oxygen deficient spinel phase, though EDX identifies it as oxygen deficient Fe, Co metallic phase as well.

## 4 Results and Discussion

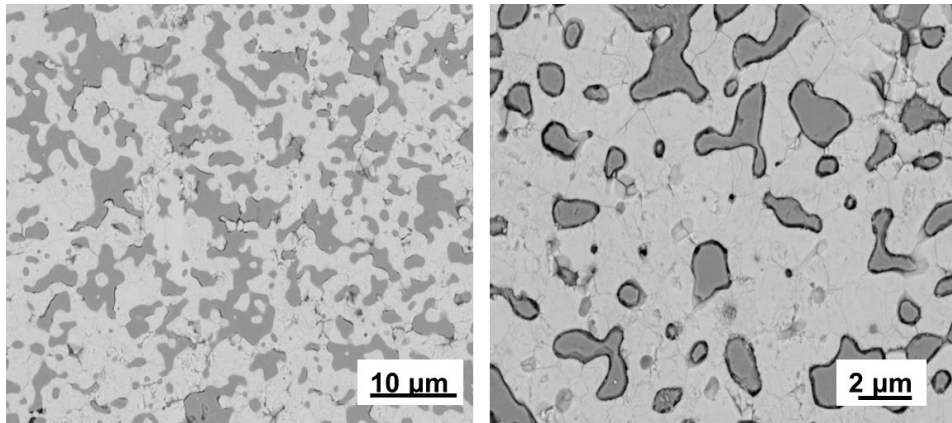


Figure 72 SEM images of 60 wt% CGO – 40 wt% FCO pre-sintered pellet after hot pressing at 50 MPa, 1200 °C for 1 h in Ar atmosphere.

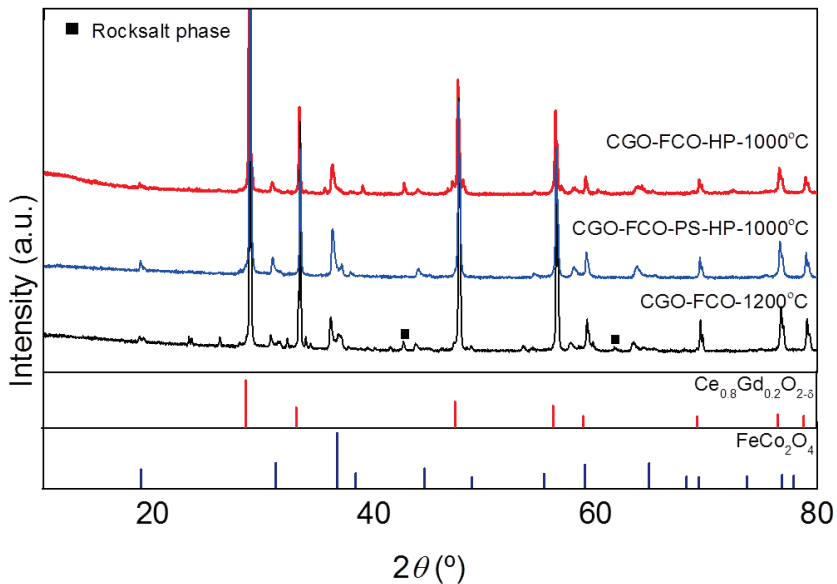


Figure 73 XRD plots of 60 wt% CGO – 40 wt% FCO hot pressed samples post annealed in air at 1000°C for 5 h. Samples differentiated by marking PS for pre-sintered and HP for hot pressing.

Both hot pressed sample were later subjected to annealing in air at 1000°C for 5 h to investigate the phase change and accompanied sample deformation if any, due to presence of oxidizing

conditions. The Fe, Co metallic phases in both the cases were transformed into spinel phases as shown in the XRD plot of the same (Figure 73). In any case flux measurable dense membranes could not be obtained using this approach. Similar to the conventionally sintered sample, pre-pressed sample also has rock salt phase while the pre-sintered sample does not show any rock salt phase peak. Also it can be stated that the third phase (orthorhombic perovskite) peaks are not visible in both the cases.

#### b) $\text{Al}_2\text{O}_3$ Die

Use of  $\text{Al}_2\text{O}_3$  die in place of graphite die was considered as an alternate option to control the reduction of spinel phase to their metallic phase. CGO-FCO powder pre-pressed into 13 mm diameter pellet placed between two cylindrical  $\text{Al}_2\text{O}_3$  dies was subjected to hot pressing with identical process parameters as before. Figure 74 shows the image after the hot pressing process. The pellet was attached to the die on both sides to form a strong sandwich and had to be separated with some mechanical load application.



**Figure 74 60 wt% CGO – 40 wt% FCO hot pressed at 50 MPa, 1200 °C for 1 h using  $\text{Al}_2\text{O}_3$  die in argon atmosphere**

This is due to interaction between the pre-pressed pellet and the die when exposed to reducing atmosphere at relatively high pressure. Figure 75 shows the XRD plot of the pellet along with the  $\text{Al}_2\text{O}_3$  die to possibly see the level of interaction between the die and the pellet. XRD analysis of the sample showed presence of fluorite phase, rock salt phase, spinel phase and perovskite phase as observed in CGO-FCO samples conventionally sintered. In addition, there were  $\text{Al}_2\text{O}_3$ , and traces of  $\text{CeAlO}_3$  clearly depicting the interaction between the composite and die to a certain extent.

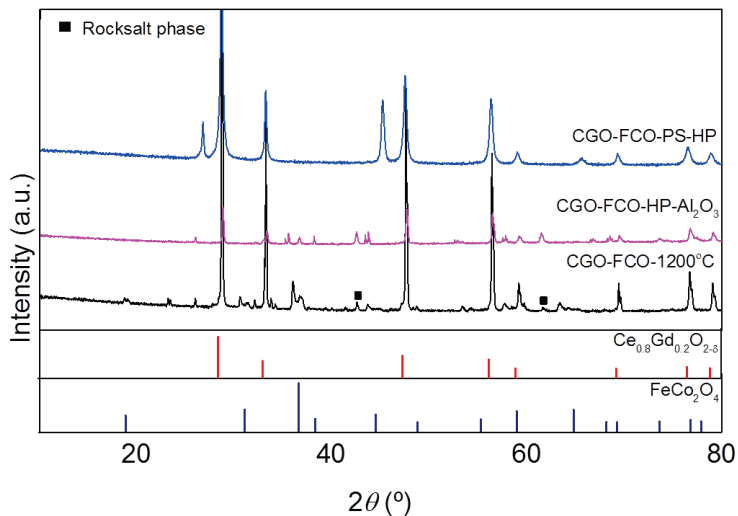


**Figure 75** XRD plot of 60 wt% CGO – 40 wt% FCO pre-pressed pellet hot pressed at 50 MPa, 1200 °C for 1 h using  $\text{Al}_2\text{O}_3$  die in argon atmosphere.

Comparing previous hot pressing experiments using graphite die versus the  $\text{Al}_2\text{O}_3$  die experiment, it is evident that spinel in CGO-FCO composite does not reduce to its metallic form (Figure 75).

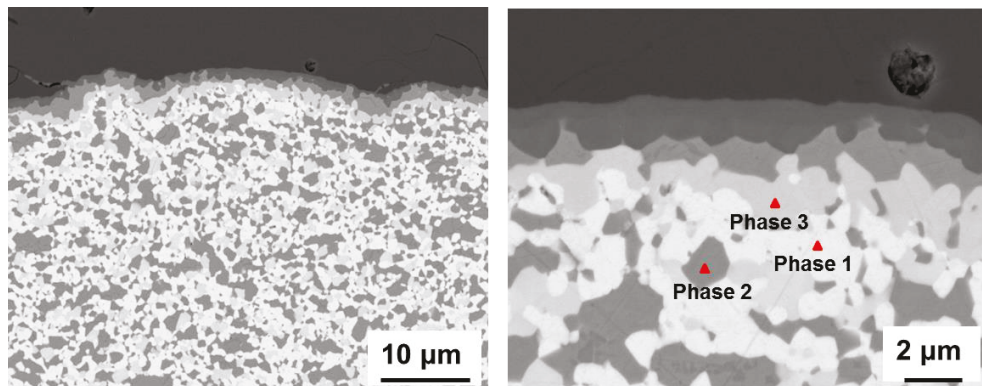


**Figure 76** SEM images of 60 wt% CGO – 40 wt% FCO pre-pressed pellet hot pressed at 50 MPa, 1200 °C for 1 h using  $\text{Al}_2\text{O}_3$  die in argon atmosphere. Phase 1 – CGO, Phase 2 – FCO and Phase 3 – GCFCO.

But, the XRD analysis also shows higher match to rock salt phase peaks compared to the conventional sintering process indicating the lack of oxygen (caused by Ar atmosphere) required to sustain the spinel phases during cooling according to Figure 28. Figure 76 shows the SEM images of the cross sectioned sample. The EDS spectrum of the SEM image clearly indicates that the segregated dark phase is rich in Co and Fe with Al followed by inclusion of traces of Ce and Gd in the dark and lighter gray phases. Further into the surface, all three phases of the composite similar to conventionally sintered sample were observed and confirmed by EDS spectrum as well. Thus the sustained oxygen due to use of  $\text{Al}_2\text{O}_3$  die does not allow complete decomposition of spinel into their metallic phase as in the other two cases of hot pressing experiment with graphite dies.

Summarizing the hot pressing experiment section, it is difficult to produce CGO-FCO oxide membranes in reducing atmosphere as the phases tend to reduce to their metallic phases by the use of Ar atmosphere and graphite die. Graphite, when not in direct contact with the composite helps less reduction of spinel but  $\text{Al}_2\text{O}_3$  interaction with ceria and perovskite formation is still a concern. Thus use of ceramic dies in oxidizing atmosphere would help overcome the issues faced in the above experiments. Also reducing the hot pressing temperature would be an interesting approach for future work since high pressure application might lower the sintering temperature required for densification.

### **SPS/FAST Technique**

Another attempt to obtain dense dual phase CGO-FCO membrane, FAST/SPS method for the fabrication of this composite at lower temperature of e.g. 850-900 °C was investigated. Literature study revealed that attempts have been made to obtain individual phases (CGO and FCO) by SPS method. According to these authors, spinel with higher iron content tend to decompose into spinel and rocksalt phase at as low as 700 °C by SPS method (Imine '11, Millot '07) whereas CGO phase would need at least 1100 °C to densify.

During the SPS process, gas pressure showed slight increase (up to 3.25 mbar) between temperature 830 to 900 °C and then decreased again to standard value (~ 3.08 mbar). This slight increase in gas pressure is related to the spinel decomposition (oxygen release) during the process. The sample showed no traces of interaction with graphite and was retrieved in pieces as it was brittle and broke while attempting to separate it from the graphite foil.

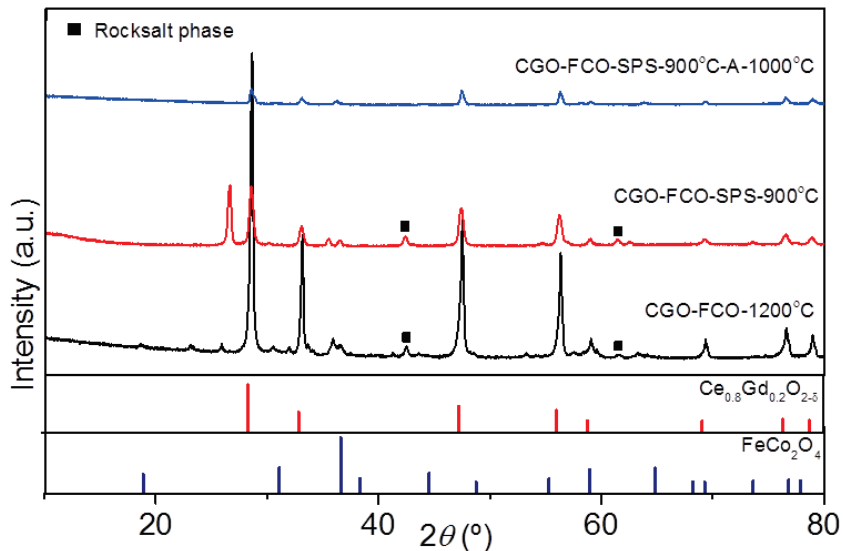


**Figure 77** XRD plot of 60 wt% CGO – 40 wt% FCO conventionally sintered (CS) at 1200 °C, SPS/FAST sintered at 900 °C (SPS) and SPS/FAST sintered sample annealed (A) at 1000 °C.

The XRD analysis of the sample after SPS/FAST showed presence of 3 phases: Fluorite (CGO), spinel ( $\text{FeCo}_2\text{O}_4$ ) and rocksalt (CoO) as shown in Figure 77. The SPS sample was subjected to annealing in presence of air at 1000 °C for 5 h. The sample was shattered into small pieces inside the furnace. The reducing atmosphere by the use of graphite dies during SPS shifts the stability limit of the rocksalt phase to lower temperatures. Thus when re-oxidized during annealing, the rock salt phase transforms to spinel which leads to large stress and volume expansion causing the violent rupture of the sample. However, the XRD plot of the annealed powder does show clear peaks of any phases as shown in Figure 77 due to the less availability of the sample after the destruction inside the furnace during the annealing process. In order to avoid CoO phase, it may be necessary to reduce the temperature, but this might further compromise the dense packing in the composite making it not suitable for application. Another promising option would be to use non-graphite ceramic dies for the SPS/FAST technique.

**Table 13 Alternative sintering techniques and their outcomes**

Hot Pressing			SPS/ FAST
Graphite die	Graphite die + Pre-sintered	Alumina die	
Dense pellet (melted to the die)	Dense pellet (deformed)	Pellet melted to the die	Not dense, brittle and cracked (when annealed in air)
Fluorite + metallic Co, Fe phase	Fluorite + metallic Co, Fe phase	Fluorite + spinel + rock salt phase	Fluorite + spinel + rock salt phase
No third phase	No third phase	No third phase	Orthorhombic perovskite

Summarizing the effort to identify an alternative sintering technique, it can be stated that achieving dense membranes with desired phases have not been successful. There have been several set backs such as deformation of sample, reduction of spinel to its metallic phase, micro-cracks and more as described in Table 13. Thus, optimized conventional sintering with the slow cooling rate between 900 - 800 °C has proven to be the favorable option for producing dense dual phase composites. Reducing the sintering temperature in case of hot pressing and use of non graphite ceramic dies for both hot pressing and SPS/FAST would be interesting options for future investigations.

### 4.3.3. Asymmetric Membrane by Tape Casting

Thin film dense membranes exhibit significantly improved oxygen permeation. But with decreasing thickness, limiting step for permeation change ( $L > L_c$ ) from bulk to surface exchange kinetics. Thus upscaling of membrane fabrication involves manufacture of supported thin film membranes by tape casting process. Further flux improvement is addressed by overcoming surface exchange limitation by introducing additional porous catalytic layer on the membrane and catalyst infiltration in the porous support.

CGO-FCO 85:15 wt% ratio has been chosen as the composition for asymmetric membranes development due its highest permeance of all investigated CGO-FCO ratios. Additionally, by the formation of the electronic conducting GCFCO perovskite phase, the segregation of cations in a  $p_{O_2}$  gradient seems to have reduced. Lastly, the composite also proves to be stable in different gas mixtures and high pressure (extended up to 5 bar on a  $\phi$  10 mm sample proven) application. Thus, next logical step of progress is the development of asymmetric membrane by tape casting to achieve the maximum oxygen flux.

#### Membrane Layer

Based on physical properties such as theoretical density, particle size distribution, shape, surface area, sintering behavior of the composite combined with extended tape casting expertise in house from several other materials, a basic slurry system was adjusted to the powder and cast into thin layers ( $\sim 50 \mu\text{m}$ ) as functional membrane layer. Pechini synthesized powder was used for dense thin membrane layer fabrication, Table 14 details the list of slurry preparation involved for optimization of the process. Each slurry preparation was carried out with 30 g of the composite powder mixed with binder, dispersant and plasticizers as explained in Table 14 in terms of their solid content weight %. Initially, the dense thin membrane layer had pinholes, bubbles and cracks. These defects were attributed to an insufficient dispersion of powder. With modification in the slurry recipe and the mixing procedure, it was overcome and a defect free and flexible thin layer foil was achieved. However, on contact with solvent during the sequential tape casting of the support layer, the membrane layer disintegrates into cracks as shown in Figure 78.

**Table 14 Slurry development for tape casting of a dual phase membrane starting from CGO-FCO 85:15 powders prepared via pechini route.**

Recipe (Wt %)	Slurry 1	Slurry 2	Slurry 3	Slurry 4	Slurry 5	Slurry 6
Mixer	Thinky	Tumbler				
Solid content	22	20	25	22	22	20 (SSR)
Dispersant (Nuospere FX9086)	2	3	3	3	3	3
Binder (PVB98)	10	10	7	7	8	7
Plasticizer 1 (S-2075)	7.5	8	6	5	7	6
Plasticizer 2 (PEG400)	6	6	3	5	5	7
Issues	Cracks, Pinholes, Bubbles after sintering	Crack formation on solvent contact	Crack formation on solvent contact	Wettability issue and shrinkage variation	(drying controlled by a cover) foil good, sintered membrane not dense	(drying controlled by a cover) foil good, dense after sintering

This defect was mainly attributed to the wettability of the particles, in other terms as concerns related to formation of a polymer network which ensures the necessary mechanical stability and flexibility required of the fabricated green membrane layer. This meant optimizing the binder and plasticizer content to obtain dense thin layer, free of visible defects. In parallel CGO-FCO 85:15 SSR route powder was also used for preparing the slurry slight modification to the recipe based on the powder morphology. The resulting membrane layer appeared to be defect free in comparison to the Pechini route thin film.

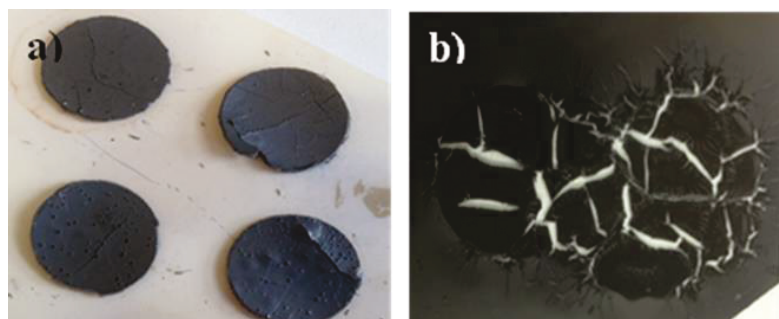


**Figure 78 Defects observed in CGO-FCO 85:15 Membrane layer produced with pechini synthesized powder. a) Pin holes and Cracks after sintering b) Crack propagation of green tape in contact with solvent**

## 4 Results and Discussion

### Support layer

Development of the support layer is very critical as it provides the necessary mechanical stability for the thin dense membrane layer. Its porous structure must enable the efficient feed gas flow to the membrane layer thus 30 to 40% porosity is required in the support layer. Co-precipitation of CoO co-doped CGO was investigated as a potential porous substrate material since CoO has proven to be a good sintering aid that reduces the sintering temperature of CGO (Schmale '11). Thus, it is expected to match with CGO-FCO membrane layer during the co-sintering process of the asymmetric membrane structure. The cobalt addition is done over the dried precursor powder by incipient wetness impregnation. In this method,  $\text{Co}(\text{NO}_3)_2 \cdot 6\text{H}_2\text{O}$  is dissolved in deionized water (volume according with the pore volume) and mixed with the commercially available CGO powder (Guizard).  $\text{NO}_x$  evaporates and CoO in CGO mixture is retained. Finally, the powder is calcined for 15 h in air atmosphere at 700 °C (Similar to Pechini synthesized CGO-FCO composite) to decompose the residual nitrates and carbonates and to favor the retaining of fluorite phase (Fagg '09, Schmale '11). A study to identify the optimal sintering aid content was carried out by adding 2, 5 and 10 mol% of CoO to CGO. Based on the sintering behavior curve of all the three combinations, the addition of 2 mol% CoO was sufficient to lower the sintering temperature of the CGO powder, down to 1200°C. Also an increase in CoO content did not improve the sinter ability of the CGO further (Kleinlogel '00). CoO grains are distributed throughout the support layer as shown in SEM images (Figure 84).

Pore former is an important ingredient in the slurry for support layer as it tailors the microstructure to improve the gas exchange through the pores it introduces in the structure. Starch is a suitable pore former and type of starch depends on pore size and shape suitable in the structure. Based on the % of porosity necessary, starch content is decided in relation with ceramic powder mass (Schulze-Küppers '13). Support slurry development started from a standard slurry system. Table 15 indicates number of slurry preparations to optimize the system as we encountered several difficulties in achieving the desired slurry and defect free support layer. Though the support layer witnessed several defects including crowfoot cracks and boating (Figure 79), some defects were also attributed to consequence of the high binder content in the membrane layer in the sequential casting process. Boating is attributed to the fast evaporation of solvent at the tape-air surface that causes bending of edges during drying.

**Table 15 Slurry development for tape casting of support starting from CGO +CoO powders. Corn starch (CS), graphite (GR) and rice starch (RS)**

Recipe (Wt %)	Slurry 1			Slurry 2	Slurry 3	Slurry 4	Slurry 5	Slurry 6
	2%	5%	10%	2% CoO				
Solid content	28			20	18	20	20	20
Pore Former	20(CS)			20(GR)	30 (RS)	30 (RS)	30 (RS)	30 (RS)
Dispersant (Nuospere FX9086)	3			3	3	3	3	3
Binder (PVB98)	7			7	7	7	7	7
Plasticizer 1 (S-2075)	6			6	6	6	6	6
Plasticizer 2 (PEG400)	3			3	3	5	10	7
Issues	Thick and cracks			Brittle and cracks	Boating	Boating	Crow foot cracks	controlled drying by covering the tape, good results

Here a dry skin forms hindering the homogenous evaporation of solvent through the entire tape thickness. This leads to high lateral shrinkage of top layer compared to the bottom while the adherence of the particles of the complete chemical system is strong enough not to form cracks. Main alterations involved replacement of corn starch to rice starch, solid weight content of CGO-FCO powder and Plasticizer 2 (PEG400). Increasing PEG400 content increases flexibility of the polymer network, this embeds the ceramic particles and avoids high lateral shrinkage. Finding a balance between binder and plasticizer content and initiating slow/controlled drying proved to be successful.

#### 4 Results and Discussion

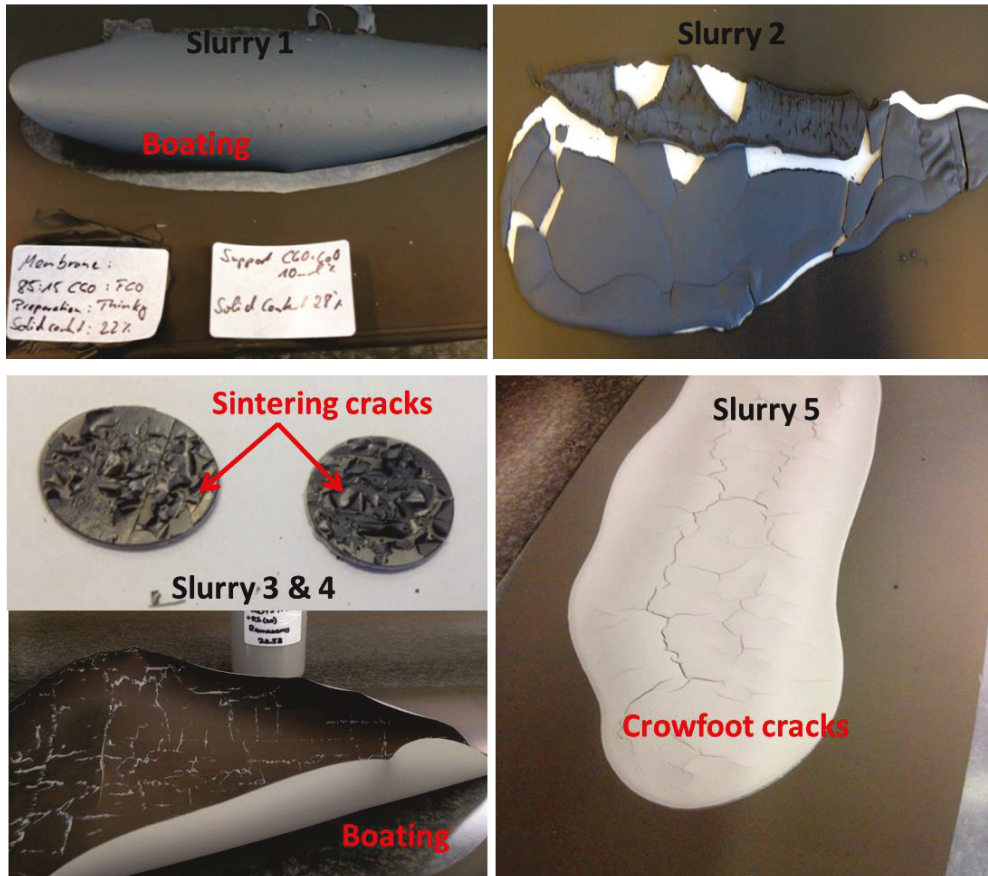


**Figure 79** Defects observed in CGO -2 mol% CoO Support layer such as boating, crowfoot cracks and sintering cracks

CGO-FCO 85:18 (SSR) powder was also made into slurry for support layer casting as an alternate option. The cast showed traces of crowfoot cracks but replacing Nuosperse FX9068 dispersant by TEGO DISPERS 655 (polyetherphosphate) proved to be successful.

**Table 16** slurry prepared for tape casting of support layer from CGO-FCO 85:15 SSR powder.

Recipe (Wt %)	Solid content	Pore Former	Dispersant (TEGO DISPERS 655)	Binder (PVB98)	Plasticizer 1 (S-2075)	Plasticizer 2 (PEG400)
CGO-FCO 85:15 (SSR)	20	30(RS)	3	7	6	7

After sintering at 1200 °C for 5 h, samples showed traces of cracks, bubbles and delamination that could be due to fast debinding and/or sintering process and hence heat treatment optimization is essential. The defect free sintered samples obtained were subjected to microstructure analysis. An overview of the investigated CGO-FCO membrane – support asymmetric membrane system is given in Table 17. The development of dense membrane layers starting from Pechini powder was not successful. The sintered membranes showed severe leakage caused by pinholes and cracks in the membrane layer. Cracks are a result of sintering activity mismatch between the membrane and support attributed to the high surface area of Pechini powder. In addition, the Pechini powder agglomerates exhibit a high inner porosity that does not densify during sintering leaving pinholes in the thin layer. Contrary to the results of the Pechini powder, sintered membranes made from the SSR route powder showed excellent gas tightness on both types of supports.

**Table 17 list of membrane / support tape cast combinations subjected to microstructure investigation.**

<b>Membrane starting powder</b>	Pechini powder		Mixed oxide powder (SSR)	
<b>Support starting powder</b>	Mixed oxide powder (SSR)	2 mol% CoO – CGO	Mixed oxide powder (SSR)	2 mol% CoO – CGO
<b>Microstructure</b>	Figure 80	Figure 81	Figure 82	Figure 83

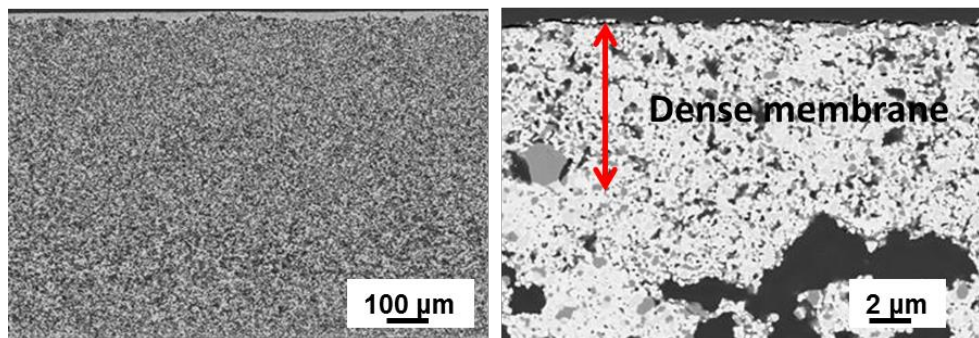


**Figure 80** Tape cast asymmetric CGO-FCO 85:15 (Pechini) membrane with porous CGO-FCO 85:15 (SSR) support sintered at 1200 °C for 5 h.

#### 4 Results and Discussion

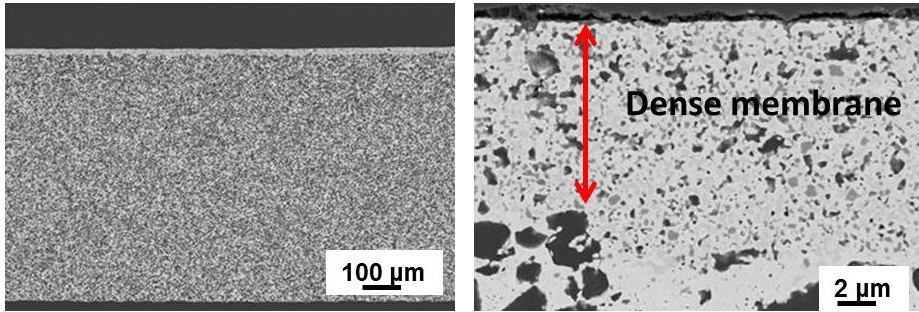


Figure 81 Tape cast asymmetric CGO-FCO 85:15 (Pechini) membrane with porous 2 mol% CoO-CGO support sintered at 1200 °C for 5 h.

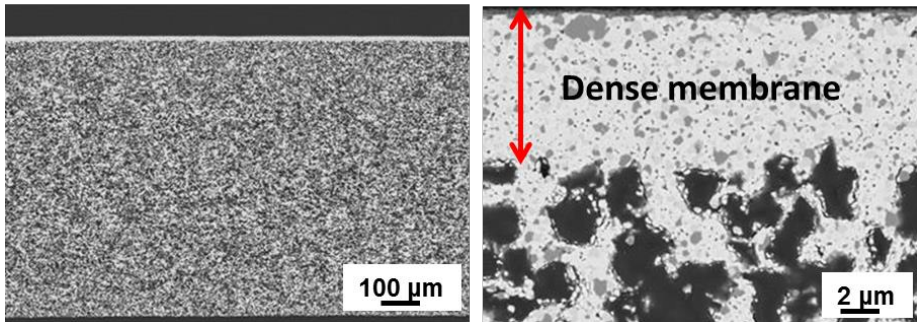


Figure 82 Tape cast asymmetric CGO-FCO 85:15 (SSR) membrane with porous CGO-FCO 85:15 (SSR) support sintered at 1200 °C for 5 h.

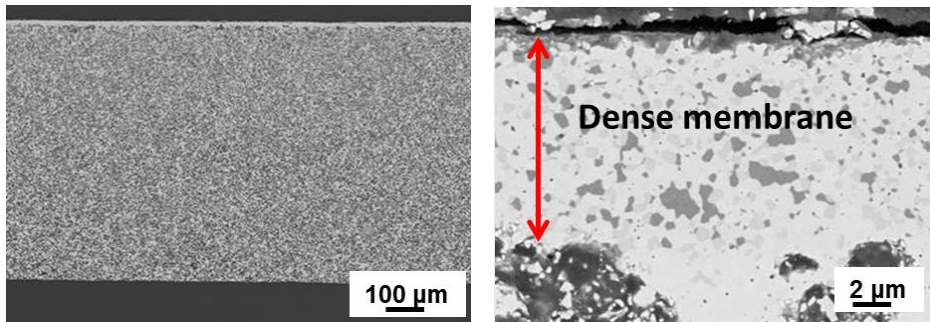


Figure 83 Tape cast asymmetric CGO-FCO 85:15 (SSR) membrane with porous 2 mol% CoO-CGO support sintered at 1200 °C for 5 h.

Due to the homogenous particle size distribution and the dense powder morphology, no pinholes were formed. Sintering activity of support and membrane layer seems to be closely matching to avoid cracks in the membrane layer. Membrane layer thickness and support porosity was determined by quantitative image analysis. The manufacturing of thin layers with thickness below 20  $\mu\text{m}$ , in combination with manufacturing of above 40 vol% porous supports is possible (Table 18).

**Table 18 Microstructural parameters of the asymmetric membranes manufactured by sequential tape casting, determined by quantitative image analysis.**

Membrane	Support	SEM images	Membrane layer thickness [ $\mu\text{m}$ ]	Support porosity [%]	Gas tight
CGO-FCO 85:15 (Pechini)	CGO-FCO 85:15 (SSR)	Figure 80	$14.0 \pm 1.5$	$40.9 \pm 1.5$	no
CGO-FCO 85:15 (Pechini)	2 mol% CoO-CGO	Figure 81	$18.3 \pm 1.4$	$45.5 \pm 2.3$	No
CGO-FCO 85:15 (SSR)	CGO-FCO 85:15 (SSR)	Figure 82	$11.3 \pm 0.3$	$51.8 \pm 1.7$	yes
CGO-FCO 85:15 (SSR)	2 mol% CoO-CGO	Figure 83	$11.1 \pm 0.9$	$48.4 \pm 1.4$	yes

The diffusion of spinel cations into the support layer was investigated on the CGO-FCO membranes with 2 mol% CoO-CGO support. No iron or larger segregations of Co were detected in the support layer, as shown in Figure 84.

## 4 Results and Discussion

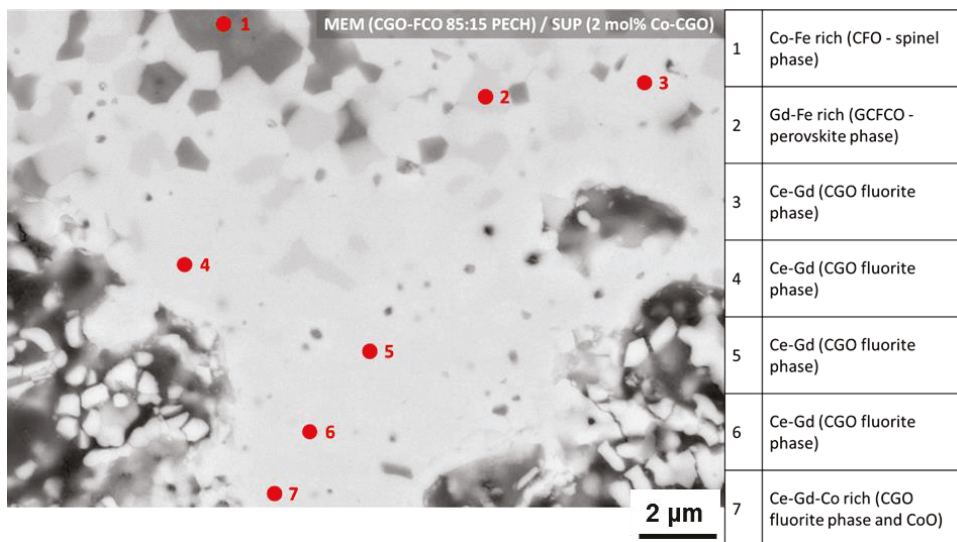


**Figure 84** EDX analysis of CGO-FCO 85:15 (Pechini) membrane / 2 mol% CoO-CGO support interface of the tape cast membrane sintered at 1200 °C for 5 h.

### Permeation measurement

The CGO-FCO SSR membrane with 2 mol% CoO-CGO support layer sample was not tested for oxygen permeation, though the sintered sample was gas tight. The sample showed traces of warping that made sealing for oxygen permeation measurement not possible. CGO-FCO 85:15 SSR membrane + support structure was tested for oxygen permeation measurement in air/Ar gradient using the test setup described in section 3.3. A porous LSCF layer (5 μm thickness) was coated on the membrane side (sweep side) that facilitates surface exchange to the thin membrane film (~11 μm). Limitations of surface exchange on the support side can be expected due to absence of catalytic activation. The comparison of oxygen permeation between a 1 mm bulk membrane with both sides activated and the asymmetric membrane with one side activated is as shown in Figure 85 (left). Permeation measurements of the membrane showed an oxygen flux of  $1 \text{ ml cm}^{-2} \text{ min}^{-1}$  @1000 °C in air/Ar gradient. The oxygen permeation increases by a factor of 3.7 at 1000 °C when using an 11 μm asymmetric membrane compared to the 1 mm bulk membrane. The decrease of this factor with temperature is due to the insufficient activation of the thin membrane at the support side, where surface exchange becomes more limiting with decreasing

temperature. This is supported by the increasing apparent activation energies with decreasing temperature as shown in Figure 85 (right). The apparent activation energy of the thin film membrane at high temperature is above the  $E_A$  of the ionic conductivity for the bulk membrane ( $\sim 60 - 70$  kJ/mol), indicating that the ionic conducting phase is not the only rate limiting factor. At temperatures below  $900^\circ\text{C}$ ,  $E_A$  is  $148$  kJ/mol and below  $800^\circ\text{C}$ ,  $E_A$  is  $215$  kJ/mol, indicating the rate limitation by surface exchange.

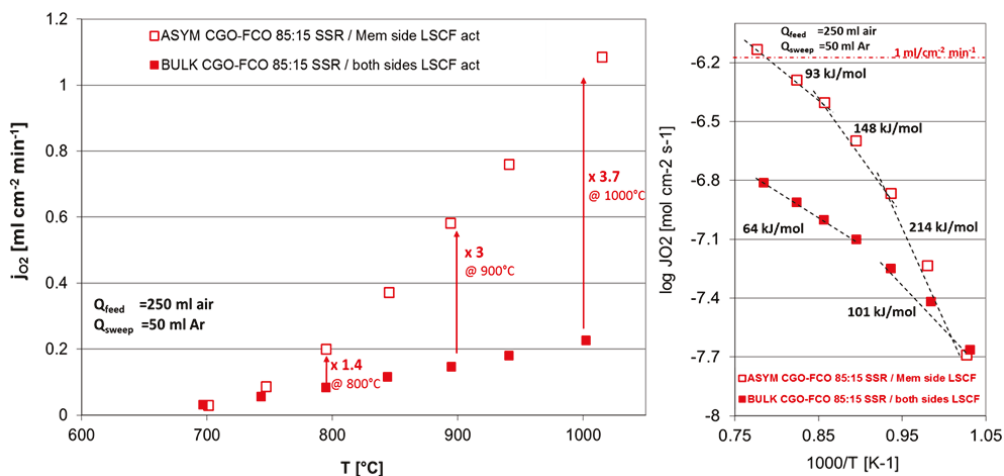


**Figure 85 Comparison of oxygen flux (left) and permeability (right) between 1mm bulk membrane (2 sides activated) and the asymmetric membrane (1 side activated). Both membranes were made from CGO-FCO 85:15 SSR powder sintered at  $1200^\circ\text{C}$  for 5 h.**

### Sintering Profile

As mentioned in the support layer sub section, heat treatment optimization has been carried out since 75% of the sintered samples were cracked with the past sintering profile (Figure 87 red) after obtaining defect free tapes of supported asymmetric membranes with optimized slurry made from CGO-FCO SSR as the starting powder for both membrane and support layers successfully. DTA/TG analysis of membrane, support and membrane + support layers combined (all made from CGO-FCO SSR powders) were carried out. Figure 86 clearly indicates severe mass loss between temperatures  $200 - 500^\circ\text{C}$  corresponding to organics burn out (binder, plasticizer and pore former). Membrane layer (red) alone does not show such severe mass loss when compared

#### 4 Results and Discussion

to support layer (pink) and membrane + support combined layers (black) organics burn off. This means pore former burning is quite rapid which needs to be controlled by having a very slow heating rate between that temperature ranges. Additionally, dwell time of 5 h at 1200 °C was not sufficient to obtain gas tight membranes with the optimized slurry so it has been increased to 10 h consistent with the sintering temperature and dwell time for bulk membranes.

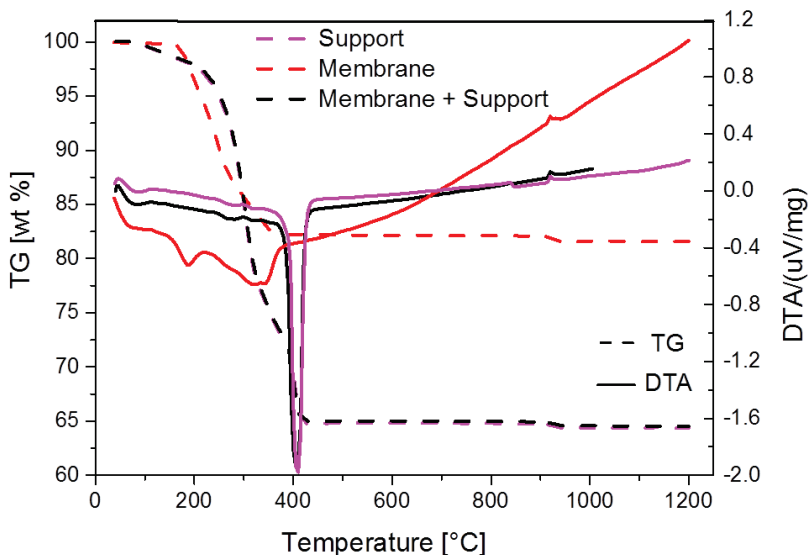


**Figure 86 DTA/TG of membrane, support and membrane+support layers combined subjected to sintering cycle at 3 K/min upto 1200 °C in air. powders made from CGO-FCO 85:15 SSR route for both membrane and support layers**

Therefore optimized sintering profile (Figure 87 blue) has provided defect free dense asymmetric membrane with porous support successfully.

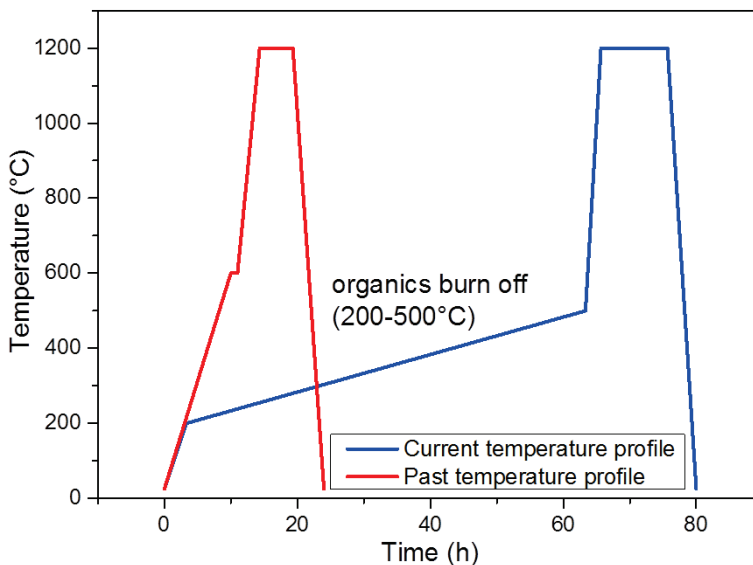


**Figure 87 Heat treatment profile for porous asymmetric membrane by tape casting, sintered at 1200°C. powders made from CGO-FCO 85:15 SSR route for both membrane and support layers.**

Summarizing the asymmetric membrane development section, the result has been very positive and has set the benchmark for development of asymmetric dual phase membranes in the future. Starting with the powder synthesis, SSR route has proven to be the most potential powder production option for up scaling the CGO-FCO membrane manufacture. Secondly, process optimization led to manufacture of defect free tapes of porous asymmetric membrane made from CGO-FCO 85:15 SSR powder successfully. It is also important to investigate SP powders for manufacture of asymmetric membranes by tape casting to compare the microstructure and performance with its counterpart SSR powder. Finally achieving the milestone of  $1 \text{ ml cm}^{-2} \text{ min}^{-1}$  oxygen flux @1000 °C using porous asymmetric membrane in air/Ar gradient benchmarks the performance of a dual phase membrane amidst very few literatures reporting the possibility of up scaling such dual phase membrane development. There is high potential for obtaining  $1 \text{ ml cm}^{-2} \text{ min}^{-1}$  at a lower temperature (850 °C – operating temperature in power plants) by addressing the surface limitations at the interface between membrane and support layer in the near future.

## 5. Summary and Outlook

This PhD thesis work involves development of dual phase oxygen transport membrane for oxyfuel combustion. The dual phase membrane is expected to have good thermal expansion match between the phases, provide high oxygen transport and enhanced chemical stability compared to more established single phase OTMs like LSCF and BSCF in flue gas streams of power plants. Combination of Phase A - ionic conducting phase ( $\text{Ce}_{0.8}\text{Gd}_{0.2}\text{O}_{2-\delta}$  - CGO) with Phase B - a promising pure electronic or MIEC phase defines the intended dual phase membrane. Material screening is followed by identifying the suitable proportion of the phases and proof of concept powder synthesis route. Phase interactions are investigated in detail to evaluate their influence on the membrane performance. Thermochemical and mechanical stability are tested by state of the art preliminary experiments at ORNL. Process optimization involving lab scale conventional densification and pressure enhanced sintering of membranes are explored. Finally, potential for up scaling of the membrane development by tape casting process is investigated.

CGO-FCO ( $\text{Ce}_{0.8}\text{Gd}_{0.2}\text{O}_{2-\delta}$  -  $\text{FeCo}_2\text{O}_4$ ) identified as the most promising dual phase membrane in which, FCO a pure electronic conductor was screened among several pure electronic and MIEC materials. Dense bulk membranes of 60 wt% CGO - 40 wt% FCO were achieved by conventional sintering at 1200 °C for 10 h in air. Formation of a third phase,  $\text{GdFeO}_3$  perovskite with traces of Ce and Co (abbreviated as GCFCO) has been proved by XRD, SEM and TEM investigations. Additionally, Co rich spinel phase decomposes to form a rock salt phase CoO causing micro-cracks in the membrane. This decomposition is reversible and can be avoided by including a slow cooling step between the temperatures 900-800 °C thus eliminating crack formation

Detailed investigation of the perovskite phase formation was conducted by PLD coating a thin film of FCO layer (~100 nm) on CGO substrates and performing annealing experiments between 1000 - 1200 °C. This phase interaction and GCFCO phase formation in the annealed samples were identified by electron microscopic analysis that was further validated by the ToF-SIMS depth profiling analysis to conclude the same. The GCFCO perovskite phase is formed around 1000°C and is unavoidable in CGO-FCO dual phase combination. This GCFCO phase is identified as a pure electronic conductor by its electrical conductivity and oxygen permeation

measurements as an individual phase. Therefore, the GCFCO phase formed as individual grains provides additional electronic conductivity to the dual phase composite.

Oxygen flux of CGO-FCO 60:40 wt% measured was lower than single phase OTM based on LSCF due to surface exchange limitation. The high activation energy at lower temperatures (850 °C - 700 °C)  $\sim$ 140 kJ/mol was attributed to the surface exchange limitation even for a 1mm thick dual phase membrane. Therefore, CGO-FCO membranes were surface activated by porous LSCF coating to improving the oxygen flux. Porous LSCF layers were coated on both side of the membrane improving the oxygen flux and reducing the activation energy throughout the measurement temperature range 700 °C - 1000 °C. Consequently, ionic conductivity became the rate limiting factor for permeation at high temperatures. Thus optimization of CGO-FCO ratio was schematically experimented by lowering the spinel content between 40 wt% and 10 wt%. CGO-FCO 85:15 wt% identified as the optimum dual phase composition with the highest oxygen permeation. A surface activated CGO-FCO 85:15 wt% bulk membrane (1 mm thick) exhibit an oxygen flux of  $0.16 \text{ ml cm}^{-2} \text{ min}^{-1}$  at 850 °C in air/Ar gradient.

Thermo-chemical stability of CGO-FCO membranes were evaluated by state of the art annealing experiments at 850 °C in the presence of varying gas mixtures comprising of CO<sub>2</sub>, SO<sub>2</sub> and H<sub>2</sub>O, carried out at ORNL. These preliminary short term tests proved CGO-FCO membranes as very stable materials. Additionally, harsh ambience in power plants also includes high pressure; hence the membranes were subjected to high pressure (up to 5 bars) permeation measurements. The measurements clarified the influence of increased partial pressure gradient as a driving force in improving the flux and its mechanical stability. The high flux combined with superior thermochemical stability proven in specialized flue gas mixtures replicating power plant ambience (a novel testing condition) fulfills the objective of this PhD work. Thus CGO-FCO 85:15 wt% membrane can be categorized as the most promising dual phase material compared to most dual phase membranes reported in the literature (Table 1).

Identifying a suitable powder synthesis route for future up scaling of the membrane technology was investigated with Pechini, Solid State Reaction (SSR) and Spray Pyrolysis (SP) route powders. SSR powder was promising in comparison to SP and Pechini route powders. The process optimization section looked into pressure enhanced sintering techniques such as Hot Pressing (HP) and SPS/FAST methods for producing dense CGO-FCO membranes with

## 5 Summary and Outlook

modified microstructure. Use of graphite dies and argon atmosphere reduce the oxide phases and destructs the sample. Asymmetric membrane by tape casting was another approach for process optimization. CGO-FCO supported dense asymmetric membranes were successfully manufactured from 85:15 wt% SSR route powders by optimizing the slurry, casting process and sintering profile. An oxygen flux of  $1.08 \text{ ml cm}^{-2} \text{ min}^{-1}$  at  $1015 \text{ }^\circ\text{C}$  in air/Ar gradient has been achieved from the surface activated CGO-FCO dual phase supported asymmetric membrane successfully.

Achieving oxygen flux of  $1 \text{ ml cm}^{-2} \text{ min}^{-1}$  in an asymmetric membrane is considered as the milestone of Green-CC project proposal. It also benchmarks the performance of a dual phase membrane amidst less reported literatures on up scaling of such membranes so far. Nevertheless, there is high potential for improving the flux even at lower temperature ( $850 \text{ }^\circ\text{C}$  – operating temperature in power plants) by addressing the surface limitations at the interface between membrane and support layer.

### **OUTLOOK**

Following the development of dual phase membrane with significant oxygen permeation successfully, there is a lot of process improvement planned to enhance oxygen flux within the scope of Green-CC project. One of the key factors would be addressing surface limitations of the supported asymmetric membrane. Open membrane side has already been surface activated with porous LSCF layer, hence catalytic infiltration at the interface between the membrane and the porous support would be the next approach to manage surface limitations. This process will impregnate catalyst grains in the pores of the support that extend the triple phase boundary (TPB) along the length of the membrane surface at the interface overcoming surface limitations. Parallel efforts for the catalytic infiltration process are on-going among two Green-CC project partners (Dr. Jose Serra's research group at ITQ, Valencia and Dr. Peter Vang Hendriksen's research group at DTU). First level experimentation of infiltration process will be carried out at IEK-1 as well in the near future. Surface activation by porous LSCF layer over dense dual phase membranes has only been considered as a preliminary test to identify the presence of surface limitations. However considering LSCF OTMs instability in exhaust flue gas streams of power plants, an alternative stable material will be investigated as porous catalytic layer in the near future.

## 6. References

- Adler, S. B. (2004). "Factors Governing Oxygen Reduction in Solid Oxide Fuel Cell Cathodes†." Chemical Reviews **104**(10): 4791-4844.
- Al Daroukh, M., V. V. Vashook, H. Ullmann, F. Tietz and I. Arual Raj (2003). "Oxides of the AMO<sub>3</sub> and A<sub>2</sub>MO<sub>4</sub>-type: structural stability, electrical conductivity and thermal expansion." Solid State Ionics **158**(1-2): 141-150.
- Bahlawane, N., P. H. T. Ngamou, V. Vannier, T. Kottke, J. Heberle and K. Kohse-Hoinghaus (2009). "Tailoring the properties and the reactivity of the spinel cobalt oxide." Physical Chemistry Chemical Physics **11**(40): 9224-9232.
- Balaguer, M., J. García-Fayos, C. Solís and J. M. Serra (2013). "Fast Oxygen Separation Through SO<sub>2</sub>- and CO<sub>2</sub>-Stable Dual-Phase Membrane Based on NiFe<sub>2</sub>O<sub>4</sub>-Ce<sub>0.8</sub>Tb<sub>0.2</sub>O<sub>2-δ</sub>." Chemistry of Materials **25**(24): 4986-4993.
- Balaguer, M., V. B. Vert, L. Navarrete and J. M. Serra (2013). "SOFC composite cathodes based on LSM and co-doped cerias (Ce<sub>0.8</sub>Gd<sub>0.1</sub>X<sub>0.1</sub>O<sub>2-δ</sub>, X = Gd, Cr, Mg, Bi, Ce)." Journal of Power Sources **223**(0): 214-220.
- Bannikov, D. O. and V. A. Cherepanov (2006). "Thermodynamic properties of complex oxides in the La-Ni-O system." Journal of Solid State Chemistry **179**(8): 2721-2727.
- Baumann, S., W. A. Meulenbergh and H. P. Buchkremer (2013). "Manufacturing strategies for asymmetric ceramic membranes for efficient separation of oxygen from air." Journal of the European Ceramic Society **33**(7): 1251-1261.
- Baumann, S., P. Niehoff, F. Schulze-Küppers, M. Ramasamy, W. A. Meulenbergh and O. Guillon (2015). The role of solid-gas electrochemical interfaces for mixed ionic electronic conducting oxygen transport membranes. ECS Transactions.
- Baumann, S., F. Schulze-Küppers, S. Roitsch, M. Betz, M. Zwick, E. M. Pfaff, W. A. Meulenbergh, J. Mayer and D. Stöver (2010). "Influence of sintering conditions on microstructure and oxygen permeation of Ba<sub>0.5</sub>Sr<sub>0.5</sub>Co<sub>0.8</sub>Fe<sub>0.2</sub>O<sub>3-δ</sub> (BSCF) oxygen transport membranes." Journal of Membrane Science **359**(1-2): 102-109.
- Baumann, S., J. M. Serra, M. P. Lobera, S. Escolástico, F. Schulze-Küppers and W. A. Meulenbergh (2011). "Ultrahigh oxygen permeation flux through supported Ba<sub>0.5</sub>Sr<sub>0.5</sub>Co<sub>0.8</sub>Fe<sub>0.2</sub>O<sub>3-δ</sub> membranes." Journal of Membrane Science **377**(1-2): 198-205.
- Belova, I. V., M. J. Brown and G. E. Murch (2003). "Analysis of kinetic demixing in a mixed oxide (A,B)O in an oxygen potential gradient." Acta Materialia **51**(6): 1821-1826.
- Benninghoven, A. (1994). "Chemical Analysis of Inorganic and Organic Surfaces and Thin Films by Static Time-of-Flight Secondary Ion Mass Spectrometry (TOF-SIMS)." Angewandte Chemie International Edition in English **33**(10): 1023-1043.

## 6 References

Betz, M. B., S.; Schulze-Küppers, F.; Meulenber, W.A. ; Stöver, D. (2010). "Supported oxygen transport membranes for oxyfuel power plants." Advances in Science and Technology **72**: 93-98.

Bevan, D. J. M., J. P. Shelton and J. S. Anderson (1948). "351. Properties of some simple oxides and spinels at high temperatures." Journal of the Chemical Society (Resumed)(0): 1729-1741.

Bouwmeester, H. J. M. and A. J. Burggraaf (1996). Chapter 10 Dense ceramic membranes for oxygen separation. Membrane Science and Technology. A. J. Burggraaf and L. Cot, Elsevier. **Volume 4**: 435-528.

Bragg, W. H. (1912). "LIV. On the direct or indirect nature of the ionization by X-rays." Philosophical Magazine Series 6 **23**(136): 647-650.

Brunauer, S., P. H. Emmett and E. Teller (1938). "Adsorption of Gases in Multimolecular Layers." Journal of the American Chemical Society **60**(2): 309-319.

Burggraaf, A. J. (1996). Chapter 2 Important characteristics of inorganic membranes. Membrane Science and Technology. A. J. Burggraaf and L. Cot, Elsevier. **Volume 4**: 21-34.

Burggraaf, A. J. (1996). Chapter 9 Transport and separation properties of membranes with gases and vapours. Membrane Science and Technology. A. J. Burggraaf and L. Cot, Elsevier. **Volume 4**: 331-433.

Burggraaf, A. J. and L. Cot (1996). Fundamentals of inorganic membrane science and technology. Membrane Science and Technology. A. J. Burggraaf and L. Cot, Elsevier. **Volume 4**: iii.

Cao, Z., H. Jiang, H. Luo, S. Baumann, W. A. Meulenber, J. Assmann, L. Mleczko, Y. Liu and J. Caro (2013). "Natural gas to fuels and chemicals: Improved methane aromatization in an oxygen-permeable membrane reactor." Angewandte Chemie - International Edition **52**(51): 13794-13797.

Cao, Z., H. Jiang, H. Luo, S. Baumann, W. A. Meulenber, H. Voss and J. Caro (2014). "An Efficient Oxygen Activation Route for Improved Ammonia Oxidation through an Oxygen-Permeable Catalytic Membrane." ChemCatChem **6**(5): 1190-1194.

Cartaxo, M. A. M., T. A. S. Ferreira, M. R. Nunes, M. H. Mendonça, M. I. da Silva Pereira and F. M. Costa (2007). "Studies on Fe-Co spinel electrodes." Solid State Sciences **9**(8): 744-749.

ChemUCDavisWeblink, W.  
"[http://chemwiki.ucdavis.edu/Core/Analytical\\_Chemistry/Instrumental\\_Analysis/Diffraction/Powder\\_X-ray\\_Diffraction](http://chemwiki.ucdavis.edu/Core/Analytical_Chemistry/Instrumental_Analysis/Diffraction/Powder_X-ray_Diffraction)."

Chen, M., B. Hallstedt and L. J. Gauckler (2003). "Thermodynamic assessment of the Co-O system." Journal of Phase Equilibria **24**(3): 212-227.

Chrisey, D. B. H., Graham K. (1994). Pulsed Laser Deposition of Thin Films, Wiley-Interscience.

Compton, A. H. (1923). "A Quantum Theory of the Scattering of X-rays by Light Elements." Physical Review **21**(5): 483-502.

Cousin, P. and R. A. Ross (1990). "Preparation of mixed oxides: a review." Materials Science and Engineering: A **130**(1): 119-125.

Czyperek, M., P. Zapp, H. J. M. Bouwmeester, M. Modigell, K. V. Peinemann, I. Voigt, W. A. Meulenber, L. Singheiser and D. Stöver (2009). "MEM-BRAIN gas separation membranes for zero-emission fossil power plants." Energy Procedia **1**(1): 303-310.

Dali, S. E., M. Jayachandran and M. J. Chockalingam (1999). "New transparent electronic conductor, MgIn<sub>2</sub>O<sub>4</sub> spinel." Journal of Materials Science Letters **18**(11): 915-917.

Dalslet, B., P. Blennow, P. V. Hendriksen, N. Bonanos, D. Lybye and M. Mogensen (2006). "Assessment of doped ceria as electrolyte." Journal of Solid State Electrochemistry **10**(8): 547-561.

Data\_Sheet\_VDM\_Crofer\_22\_APU. from [http://www.vdm-metals.com/fileadmin/user\\_upload/Downloads/Data\\_Sheets/Data\\_Sheet\\_VDM\\_Crofer\\_22\\_APU.pdf](http://www.vdm-metals.com/fileadmin/user_upload/Downloads/Data_Sheets/Data_Sheet_VDM_Crofer_22_APU.pdf).

DensityDeterminationManual\_Sartorius, W. ["http://www.dcu.ie/sites/default/files/mechanical\\_engineering/pdfs/manuals/DensityDeterminationManual.pdf."](http://www.dcu.ie/sites/default/files/mechanical_engineering/pdfs/manuals/DensityDeterminationManual.pdf)

Dong, X., W. Jin, N. Xu and K. Li (2011). "Dense ceramic catalytic membranes and membrane reactors for energy and environmental applications." Chemical Communications **47**(39): 10886-10902.

Edenhofer, O., R. Pichs-Madruga, Y. Sokona, E. Farahani, S. Kadner, K. Seyboth, A. Adler, I. Baum, S. Brunner, P. Eickemeier, B. Kriemann, J. Savolainen, S. Schlömer, C. von Stechow, T. Zwickel and J.C. Minx (eds). (2014). Contribution of Working Group III to the Fifth Assessment Report of the Intergovernmental Panel on Climate Change. IPCC. Climate Change 2014: Mitigation of Climate Change.

Engels, S., T. Markus, M. Modigell and L. Singheiser (2011). "Oxygen permeation and stability investigations on MIEC membrane materials under operating conditions for power plant processes." Journal of Membrane Science **370**(1–2): 58-69.

Fagg, D. P., D. Pérez-Coll, P. Núñez, J. R. Frade, A. L. Shaula, A. A. Yaremchenko and V. V. Kharton (2009). "Ceria based mixed conductors with adjusted electronic conductivity in the bulk and/or along grain boundaries." Solid State Ionics **180**(11–13): 896-899.

Fang, W., J. Gao and C. Chen (2013). "La<sub>0.8</sub>Sr<sub>0.2</sub>Cr<sub>0.5</sub>Fe<sub>0.5</sub>O<sub>3-δ</sub> (LSCF)–Zr<sub>0.8</sub>Y<sub>0.2</sub>O<sub>2-δ</sub> (YSZ) based multilayer membrane for CO<sub>2</sub> decomposition." Ceramics International **39**(6): 7269-7272.

## 6 References

- Feltz, A. (1991). "Investigations on electronically conducting oxide systems XX.  $\text{MgNiMnO}_{4-z}$  and properties of  $\text{Mg}_z\text{NiMn}_{2-z}\text{O}_4$  spinels." Journal of alloys and compounds **177**(1): 149-158.
- Ferguson, J. D., G. Arikan, D. S. Dale, A. R. Woll and J. D. Brock (2009). "Measurements of Surface Diffusivity and Coarsening during Pulsed Laser Deposition." Physical Review Letters **103**(25): 256103.
- Ferreira, T. A. S., J. C. Waerenborgh, M. H. R. M. Mendonça, M. R. Nunes and F. M. Costa (2003). "Structural and morphological characterization of  $\text{FeCo}_2\text{O}_4$  and  $\text{CoFe}_2\text{O}_4$  spinels prepared by a coprecipitation method." Solid State Sciences **5**(2): 383-392.
- Gauquelin, N., T. E. Weirich, M. Ceretti, W. Paulus and M. Schroeder (2009). "Long-term structural surface modifications of mixed conducting  $\text{La}_2\text{NiO}_{4+\delta}$  at high temperatures." Monatshefte Fur Chemie **140**(9): 1095-1102.
- German, R. M. (2005). Elsevier.
- Guillon, O., J. Gonzalez-Julian, B. Dargatz, T. Kessel, G. Schierning, J. Räthel and M. Herrmann (2014). "Field-Assisted Sintering Technology/Spark Plasma Sintering: Mechanisms, Materials, and Technology Developments." Advanced Engineering Materials **16**(7): 830-849.
- Guizard, C. (1996). Chapter 7 Sol-gel chemistry and its application to porous membrane processing. Membrane Science and Technology. A. J. Burggraaf and L. Cot, Elsevier. **Volume 4**: 227-258.
- Haines, P. J., M. Reading and F. W. Wilburn (1998). Chapter 5 - Differential Thermal Analysis and Differential Scanning Calorimetry. Handbook of Thermal Analysis and Calorimetry. E. B. Michael, Elsevier Science B.V. **Volume 1**: 279-361.
- Hansson, A. N., S. Linderoth, M. Mogensen and M. A. J. Somers (2005). "X-ray diffraction investigation of phase stability in the Co-Cr-O and the Fe-Co-Cr-O systems in air at 1323K." Journal of Alloys and Compounds **402**(1-2): 194-200.
- Howatt, G. N., R. G. Breckenridge and J. M. Brownlow (1947). "FABRICATION OF THIN CERAMIC SHEETS FOR CAPACITORS\*." Journal of the American Ceramic Society **30**(8): 237-242.
- Huixia, L., E. Konstantin, J. Heqing, F. Armin, W. Haihui and C. Jürgen (2011). "CO<sub>2</sub>-Stable and Cobalt-Free Dual-Phase Membrane for Oxygen Separation." Angewandte Chemie International Edition **50**(3): 759-763.
- Imine, S., F. Schoenstein, S. Mercone, M. Zaghrioui, N. Bettahar and N. Jouini (2011). "Bottom-up and new compaction processes: A way to tunable properties of nanostructured cobalt ferrite ceramics." Journal of the European Ceramic Society **31**(15): 2943-2955.
- J. O. Hong, H. I. Y. (2006). "Electric Field-Induced Unmixing in Mixed Ferrite Spinel  $(\text{Co,Fe})_3\text{O}_4$ ." Advances in Science and Technology **46**: 11-20.

- Joo, J. H., G. S. Park, C.-Y. Yoo and J. H. Yu (2013). "Contribution of the surface exchange kinetics to the oxygen transport properties in  $Gd_{0.1}Ce_{0.9}O_{2-\delta}$ - $La_{0.6}Sr_{0.4}Co_{0.2}Fe_{0.8}O_{3-\delta}$  dual-phase membrane." Solid State Ionics **253**(0): 64-69.
- Joo, J. H., K. S. Yun, Y. Lee, J. Jung, C.-Y. Yoo and J. H. Yu (2014). "Dramatically Enhanced Oxygen Fluxes in Fluorite-Rich Dual-Phase Membrane by Surface Modification." Chemistry of Materials **26**(15): 4387-4394.
- Kabekkodu, S. (2010). ICDD PDF-4+ Database, In: International Centre for Diffraction Data. Newtown Square, PA, USA, Editor.
- Kawazoe, H. and K. Ueda (1999). "Transparent Conducting Oxides Based on the Spinel Structure." Journal of the American Ceramic Society **82**(12): 3330-3336.
- Kharton, V. V., A. V. Kovalevsky, A. P. Viskup, F. M. Figueiredo, A. A. Yaremchenko, E. N. Naumovich and F. M. B. Marques (2001). "Oxygen permeability and Faradaic efficiency of  $Ce_{0.8}Gd_{0.2}O_{2-\delta}$ - $La_{0.7}Sr_{0.3}MnO_{3-\delta}$  composites." Journal of the European Ceramic Society **21**(10-11): 1763-1767.
- Kharton, V. V., F. M. B. Marques and A. Atkinson (2004). "Transport properties of solid oxide electrolyte ceramics: A brief review." Solid State Ionics **174**(1-4): 135-149.
- Kiefer, T. (2008). Entwicklung neuer Schutz- und Kontaktierungsschichten für Hochtemperatur-Brennstoffzellen. PhD Dissertation, Ruhr-Universität Bochum, Germany.
- Kleinlogel, C. M. and L. J. Gauckler\* (2000). "Mixed Electronic-Ionic Conductivity of Cobalt Doped Cerium Gadolinium Oxide." Journal of Electroceramics **5**(3): 231-243.
- Kountouros, P., R. Förthmann, A. Naoumidis, G. Stochniol and E. Syskakis (1995). "Synthesis, forming and characterization of ceramic materials for the planar solid oxide fuel cell (SOFC)." Ionics **1**(1): 40-50.
- Kringe, M. (2010). Bachelor degree Thesis.
- Kröger, F. A. and H. J. Vink (1956). Relations between the Concentrations of Imperfections in Crystalline Solids. Solid State Physics. S. Frederick and T. David, Academic Press. **Volume 3**: 307-435.
- Li, H., Y. Liu, X. Zhu, Y. Cong, S. Xu, W. Xu and W. Yang (2013). "Oxygen permeation through Ca-contained dual-phase membranes for oxyfuel CO<sub>2</sub> capture." Separation and Purification Technology **114**: 31-37.
- Li, Q. and F. Li (2013). "Preparation of self-supported dual-phase oxygen permeation membranes via chemical etching method." Materials Research Bulletin **48**(3): 1160-1165.

## 6 References

- Li, Q., X. Zhu, Y. He, Y. Cong and W. Yang (2011). "Effects of sintering temperature on properties of dual-phase oxygen permeable membranes." Journal of Membrane Science **367**(1-2): 134-140.
- Li, W., T.-F. Tian, F.-Y. Shi, Y.-S. Wang and C.-S. Chen (2009). "Ce<sub>0.8</sub>Sm<sub>0.2</sub>O<sub>2-δ</sub>-La<sub>0.8</sub>Sr<sub>0.2</sub>MnO<sub>3-δ</sub> Dual-Phase Composite Hollow Fiber Membrane for Oxygen Separation." Industrial & Engineering Chemistry Research **48**(12): 5789-5793.
- Lin, Y., S. Fang, D. Su, K. S. Brinkman and F. Chen (2015). "Enhancing grain boundary ionic conductivity in mixed ionic-electronic conductors." Nat Commun **6**.
- Lipińska-Chwałek, M., L. Kiesel and J. Malzbender (2014). "Mechanical properties of porous MgO substrates for membrane applications." Journal of the European Ceramic Society **34**(10): 2519-2524.
- Lipińska-Chwałek, M., F. Schulze-Küppers and J. Malzbender (2015). "Mechanical properties of pure and doped cerium oxide." Journal of the European Ceramic Society **35**(5): 1539-1547.
- Liu, Y., X. Tan and K. Li (2006). "Mixed conducting ceramics for catalytic membrane processing." Catalysis Reviews - Science and Engineering **48**(2): 145-198.
- Lobera, M. P., J. M. Serra, S. P. Foghmoes, M. Søggaard and A. Kaiser (2011). "On the use of supported ceria membranes for oxyfuel process/syngas production." Journal of Membrane Science **385-386**(1): 154-161.
- Luo, H., H. Jiang, K. Efimov, F. Liang, H. Wang and J. Caro (2011). "CO<sub>2</sub>-Tolerant Oxygen-Permeable Fe<sub>2</sub>O<sub>3</sub>-Ce<sub>0.9</sub>Gd<sub>0.1</sub>O<sub>2-δ</sub> Dual Phase Membranes." Industrial & Engineering Chemistry Research **50**(23): 13508-13517.
- Luo, H., H. Jiang, T. Klande, Z. Cao, F. Liang, H. Wang and J. Caro (2012). "Novel cobalt-free, noble metal-free oxygen-permeable 40Pr 0.6Sr 0.4FeO 3-δ-60Ce 0.9Pr 0.1O 2-δ dual-phase membrane." Chemistry of Materials **24**(11): 2148-2154.
- Luo, H., H. Jiang, T. Klande, F. Liang, Z. Cao, H. Wang and J. Caro (2012). "Rapid glycine-nitrate combustion synthesis of the CO<sub>2</sub>-stable dual phase membrane 40Mn1.5Co1.5O<sub>4-δ</sub>-60Ce0.9Pr0.1O<sub>2-δ</sub> for CO<sub>2</sub> capture via an oxy-fuel process." Journal of Membrane Science **423-424**(0): 450-458.
- Maca, K., V. Pouchly and A. R. Boccaccini (2008). "Sintering densification curve: A practical approach for its construction from dilatometric shrinkage data." Science of Sintering.
- Maier, J. (1994). "Defect chemistry at interfaces." Solid State Ionics **70**: 43-51.
- Martin, M. (2003). "Materials in thermodynamic potential gradients." The Journal of Chemical Thermodynamics **35**(8): 1291-1308.
- McGrath, K. M. (2001). "Ceramic membrane technologies for oxygen separation." Advanced Materials **13**(12-13): 993-996.

- McMullan, D. (1995). "Scanning electron microscopy 1928–1965." Scanning **17**(3): 175-185.
- Miao, J., P. Charalambous, J. Kirz and D. Sayre (1999). "Extending the methodology of X-ray crystallography to allow imaging of micrometre-sized non-crystalline specimens." Nature **400**(6742): 342-344.
- Millot, N., S. Le Gallet, D. Aymes, F. Bernard and Y. Grin (2007). "Spark plasma sintering of cobalt ferrite nanopowders prepared by coprecipitation and hydrothermal synthesis." Journal of the European Ceramic Society **27**(2–3): 921-926.
- Mogensen, M., N. M. Sammes and G. A. Tompsett (2000). "Physical, chemical and electrochemical properties of pure and doped ceria." Solid State Ionics **129**(1–4): 63-94.
- Molin, S., W. Lewandowska-Iwaniak, B. Kusz, M. Gazda and P. Jasinski (2012). "Structural and electrical properties of Sr(Ti, Fe)O<sub>3-δ</sub> materials for SOFC cathodes." Journal of Electroceramics **28**(1): 80-87.
- Mooney, J. B. and S. B. Radding (1982). "Spray Pyrolysis Processing." Annual Review of Materials Science **12**(1): 81-101.
- N F Mott , A. S. A. (1995). "Sir Nevill Mott – 65 Years in Physics."
- Niehoff, P., S. Baumann, F. Schulze-Küppers, R. S. Bradley, I. Shapiro, W. A. Meulenber, P. J. Withers and R. Vaßen (2014). "Oxygen transport through supported Ba<sub>0.5</sub>Sr<sub>0.5</sub>Co<sub>0.8</sub>Fe<sub>0.2</sub>O<sub>3-δ</sub> membranes." Separation and Purification Technology **121**: 60-67.
- Ohnishi, T., K. Shibuya, T. Yamamoto and M. Lippmaa (2008). "Defects and transport in complex oxide thin films." Journal of Applied Physics **103**(10): 103703.
- P. J. Gellings, H. J. B. (1997). The CRC Handbook of Solid State Electrochemistry. New York, CRC press.
- Pechini, M. P. (1967). Method of preparing lead and alkaline earth titanates and niobates and coating method using the same to form a capacitor, Google Patents.
- Pelton, A. D., H. Schmalzried and J. Sticher (1979). "Thermodynamics of Mn<sub>3</sub>O<sub>4</sub> — Co<sub>3</sub>O<sub>4</sub>, Fe<sub>3</sub>O<sub>4</sub> — Mn<sub>3</sub>O<sub>4</sub>, and Fe<sub>3</sub>O<sub>4</sub> — Co<sub>3</sub>O<sub>4</sub> Spinel by Phase Diagram Analysis." Berichte der Bunsengesellschaft für physikalische Chemie **83**(3): 241-252.
- Pirou, S., J. Gorauskis, V. Gil, M. Sjøgaard, P. V. Hendriksen, A. Kaiser, S. Ovtar and R. Kiebach (2016). "Oxygen permeation flux through 10Sc1YSZ-MnCo<sub>2</sub>O<sub>4</sub> asymmetric membranes prepared by two-step sintering." Fuel Processing Technology **152**: 192-199.
- R. E. Mistler, E. R. T. (2000). Tape Casting: Theory and Practice. Ohio, American ceramic Society.
- Ramasamy, M., S. Baumann, J. Palisaitis, F. Schulze-Küppers, M. Balaguer, D. Kim, W. A. Meulenber, J. Mayer, R. Bhave, O. Guillon and M. Bram (2016). "Influence of Microstructure

## 6 References

- and Surface Activation of Dual-Phase Membrane  $\text{Ce}_{0.8}\text{Gd}_{0.2}\text{O}_{2-\delta}\text{-FeCo}_2\text{O}_4$  on Oxygen Permeation." Journal of the American Ceramic Society **99**(1): 349-355.
- Ramírez, M. B. (2013). New solid state oxygen and hydrogen conducting materials. Towards their applications as high temperature electrochemical devices and gas separation membranes. Doctorate, Universitat Politècnica de València.
- Rice, D. E. and D. J. Buttrey (1993). "An X-Ray Diffraction Study of the Oxygen Content Phase Diagram of  $\text{La}_2\text{NiO}_{4+\delta}$ ." Journal of Solid State Chemistry **105**(1): 197-210.
- Rietveld, H. (1969). "A profile refinement method for nuclear and magnetic structures." Journal of Applied Crystallography **2**(2): 65-71.
- Ruska, E. (1987). "The Development of the Electron Microscope and of Electron Microscopy (Nobel Lecture)." Angewandte Chemie International Edition in English **26**(7): 595-605.
- Sadykov, V., V. Zarubina, S. Pavlova, T. Krieger, G. Alikina, A. Lukashevich, V. Muzykantov, E. Sadvovskaya, N. Mezentseva, E. Zevak, V. Belyaev and O. Smorygo (2010). "Design of asymmetric multilayer membranes based on mixed ionic–electronic conducting composites supported on Ni–Al foam substrate." Catalysis Today **156**(3–4): 173-180.
- Samson, A. J., M. Søggaard and P. Vang Hendriksen (2014). " $(\text{Ce,Gd})\text{O}_{2-\delta}$ -based dual phase membranes for oxygen separation." Journal of Membrane Science **470**(0): 178-188.
- Sanchez, J. and T. T. Tsotsis (1996). Chapter 11 Current developments and future research in catalytic membrane reactors. Membrane Science and Technology. A. J. Burggraaf and L. Cot, Elsevier. **Volume 4**: 529-568.
- Schafbauer, W., F. Schulze-Küppers, S. Baumann, W. A. Meulenber, N. H. Menzler, H. P. Buchkremer and D. Stöver (2012). Tape casting as a multi purpose shaping technology for different applications in energy issues. Materials Science Forum. **706-709**: 1035-1040.
- Schlehuber, D., E. Wessel, L. Singheiser and T. Markus (2010). "Long-term operation of a  $\text{La}_{0.58}\text{Sr}_{0.4}\text{Co}_{0.2}\text{Fe}_{0.8}\text{O}_{3-\delta}$ -membrane for oxygen separation." Journal of Membrane Science **351**(1-2): 16-20.
- Schmale, K., M. Grünebaum, M. Janssen, S. Baumann, F. Schulze-Küppers and H.-D. Wiemhöfer (2011). "Electronic conductivity of  $\text{Ce}_{0.8}\text{Gd}_{0.2-x}\text{Pr}_x\text{O}_{2-\delta}$  and influence of added  $\text{CoO}$ ." physica status solidi (b) **248**(2): 314-322.
- Schröder, M. (2008). "MEM-BRAIN Summer School 2008, modifiziert."
- Schulze-Küppers, F., S. Baumann, W. A. Meulenber, D. Stöver and H. P. Buchkremer (2013). "Manufacturing and performance of advanced supported  $\text{Ba}_{0.5}\text{Sr}_{0.5}\text{Co}_{0.8}\text{Fe}_{0.2}\text{O}_{3-\delta}$  (BSCF) oxygen transport membranes." Journal of Membrane Science **433**: 121-125.

- Schulze-Küppers, F., S. Baumann, W. A. Meulenberg, D. Stöver and H. P. Buchkremer (2013). "Manufacturing and performance of advanced supported Ba<sub>0.5</sub>Sr<sub>0.5</sub>Co<sub>0.8</sub>Fe<sub>0.2</sub>O<sub>3-δ</sub> (BSCF) oxygen transport membranes." Journal of Membrane Science **433**: 121-125.
- Schulze-Küppers, F., S. Baumann, F. Tietz, H. J. M. Bouwmeester and W. A. Meulenberg (2014). "Towards the fabrication of La<sub>0.98-x</sub>Sr<sub>x</sub>Co<sub>0.2</sub>Fe<sub>0.8</sub>O<sub>3-δ</sub> perovskite-type oxygen transport membranes." Journal of the European Ceramic Society **34**(15): 3741-3748.
- Schulze-Küppers, F., S. F. P. Ten Donkelaar, S. Baumann, P. Prigorodov, Y. J. Sohn, H. J. M. Bouwmeester, W. A. Meulenberg and O. Guillon (2015). "Structural and functional properties of SrTi<sub>1-x</sub>Fe<sub>x</sub>O<sub>3-δ</sub> (0 ≤ x ≤ 1) for the use as oxygen transport membrane." Separation and Purification Technology **147**: 414-421.
- Schwarz, S. and O. Guillon (2013). "Two step sintering of cubic yttria stabilized zirconia using Field Assisted Sintering Technique/Spark Plasma Sintering." Journal of the European Ceramic Society **33**(4): 637-641.
- Serra, J. M., J. Garcia-Fayos, S. Baumann, F. Schulze-Küppers and W. A. Meulenberg (2013). "Oxygen permeation through tape-cast asymmetric all-La<sub>0.6</sub>Sr<sub>0.4</sub>Co<sub>0.2</sub>Fe<sub>0.8</sub>O<sub>3-δ</sub> membranes." Journal of Membrane Science **447**: 297-305.
- Serra, J. M., J. Garcia-Fayos, S. Baumann, F. Schulze-Küppers and W. A. Meulenberg (2013). "Oxygen permeation through tape-cast asymmetric all-La<sub>0.6</sub>Sr<sub>0.4</sub>Co<sub>0.2</sub>Fe<sub>0.8</sub>O<sub>3-δ</sub> membranes." Journal of Membrane Science **447**(0): 297-305.
- Sharma, Y., N. Sharma, G. V. Subba Rao and B. V. R. Chowdari (2008). "Studies on spinel cobaltites, FeCo<sub>2</sub>O<sub>4</sub> and MgCo<sub>2</sub>O<sub>4</sub> as anodes for Li-ion batteries." Solid State Ionics **179**(15-16): 587-597.
- Shaula, A. L., V. V. Kharton and F. M. B. Marques (2004). "Phase interaction and oxygen transport in La<sub>0.8</sub>Sr<sub>0.2</sub>Fe<sub>0.8</sub>Co<sub>0.2</sub>O<sub>3-(La<sub>0.9</sub>Sr<sub>0.1</sub>)<sub>0.98</sub>Ga<sub>0.8</sub>Mg<sub>0.2</sub>O<sub>3</sub></sub> composites." Journal of the European Ceramic Society **24**(9): 2631-2639.
- Shaula, A. L., V. A. Kolotygin, E. N. Naumovich, Y. V. Pivak and V. V. Kharton (2013). Oxygen ionic transport in brownmillerite-type Ca<sub>2</sub>Fe<sub>2</sub>O<sub>5-δ</sub> and calcium ferrite-based composite membranes. Solid State Phenomena. **200**: 286-292.
- Sir, W. H. B. (1921). "The Structure of Organic Crystals." Proceedings of the Physical Society of London **34**(1): 33.
- Skinner, S. J. K., John A. (2003). "Oxygen ion conductors." Materials Today **6**(3): 30-37.
- Solis, C., L. Navarrete, M. Balaguer and J. M. Serra (2014). "Development and understanding of La<sub>0.85</sub>Sr<sub>0.15</sub>Cr<sub>1-x</sub>Ni<sub>x</sub>O<sub>3-δ</sub> anodes for La<sub>5.6</sub>WO<sub>11.4-δ</sub>-based Proton Conducting Solid Oxide Fuel Cells." Journal of Power Sources **258**: 98-107.
- Steele, B. C. H. (2000). "Appraisal of Ce<sub>1-y</sub>Gd<sub>y</sub>O<sub>2-y/2</sub> electrolytes for IT-SOFC operation at 500°C." Solid State Ionics **129**(1-4): 95-110.

## 6 References

Sun, M., X. Chen and L. Hong (2013). "Influence of the interfacial phase on the structural integrity and oxygen permeability of a dual-phase membrane." ACS Applied Materials and Interfaces **5**(18): 9067-9074.

Sunarso, J., S. Baumann, J. M. Serra, W. A. Meulenber, S. Liu, Y. S. Lin and J. C. Diniz da Costa (2008). "Mixed ionic–electronic conducting (MIEC) ceramic-based membranes for oxygen separation." Journal of Membrane Science **320**(1–2): 13-41.

Taylor, G. F. (1933). Apparatus for making hard metal compositions, Google Patents.

tf.uni-kiel.de ["http://images.google.de/imgres?imgurl=http://www.tf.uni-kiel.de/matwis/amat/def\\_en/kap\\_2/illustr/spinel.gif&imgrefurl=http://www.tf.uni-kiel.de/matwis/amat/def\\_en/kap\\_2/basics/b2\\_1\\_6.html&h=420&w=640&tbnid=yAa8K4mqSXY1-M:&tbnh=90&tbnw=137&docid=9XsXMr\\_DDRIRkM&usq=-sllLqVd3IyTtNxLZNTDkPrM910=&sa=X&ved=0ahUKEWjgqd678MrOAhUEuBQKHRphAQoQ9QEILjAD."](http://images.google.de/imgres?imgurl=http://www.tf.uni-kiel.de/matwis/amat/def_en/kap_2/illustr/spinel.gif&imgrefurl=http://www.tf.uni-kiel.de/matwis/amat/def_en/kap_2/basics/b2_1_6.html&h=420&w=640&tbnid=yAa8K4mqSXY1-M:&tbnh=90&tbnw=137&docid=9XsXMr_DDRIRkM&usq=-sllLqVd3IyTtNxLZNTDkPrM910=&sa=X&ved=0ahUKEWjgqd678MrOAhUEuBQKHRphAQoQ9QEILjAD.)

Tietz, F., I. Arul Raj, W. Jungen and D. Stöver (2001). "High-temperature superconductor materials for contact layers in solid oxide fuel cells: I. Sintering behavior and physical properties at operating temperatures." Acta Materialia **49**(5): 803-810.

Tietz, F., I. Arul Raj, Q. Ma, S. Baumann, A. Mahmoud and R. P. Hermann (2016). "Material properties of perovskites in the quasi-ternary system LaFeO<sub>3</sub>–LaCoO<sub>3</sub>–LaNiO<sub>3</sub>." Journal of Solid State Chemistry **237**: 183-191.

Uni\_GoettingenPhysikWeblink, W. ["http://physik2.uni-goettingen.de/research/2\\_hofs/methods/XRD."](http://physik2.uni-goettingen.de/research/2_hofs/methods/XRD.)

van Hassel, B. A. (2004). "Oxygen transfer across composite oxygen transport membranes." Solid State Ionics **174**(1–4): 253-260.

Vernoux, P., L. Lizarraga, M. N. Tsampas, F. M. Sapountzi, A. De Lucas-Consuegra, J.-L. Valverde, S. Souentie, C. G. Vayenas, D. Tsiplakides, S. Balomenou and E. A. Baranova (2013). "Ionically Conducting Ceramics as Active Catalyst Supports." Chemical Reviews **113**(10): 8192-8260.

Verwey, E. J., P. W. Haayman and F. C. Romeijn (1947). "Physical Properties and Cation Arrangement of Oxides with Spinel Structures II. Electronic Conductivity." The Journal of Chemical Physics **15**(4): 181-187.

Wang, S., T. Kobayashi, M. Dokiya and T. Hashimoto (2000). "Electrical and Ionic Conductivity of Gd-Doped Ceria." Journal of The Electrochemical Society **147**(10): 3606-3609.

Wang, Z., W. Sun, Z. Zhu, T. Liu and W. Liu (2013). "A Novel Cobalt-Free, CO<sub>2</sub>-Stable, and Reduction-Tolerant Dual-Phase Oxygen-Permeable Membrane." ACS Applied Materials & Interfaces **5**(21): 11038-11043.

- Williams, P. (1985). "Secondary Ion Mass Spectrometry." Annual Review of Materials Science **15**(1): 517-548.
- Williams, T. J. (2005). "Scanning electron microscopy and x-ray microanalysis, 3rd edition. By Joseph Goldstein, Dale Newbury, David Joy, Charles Lyman, Patrick Echlin, Eric Lifshin, Linda Sawyer, Joseph Michael Kluwer Academic Publishers, New York (2003) ISBN 0306472929; hardback; 688; \$75.00." Scanning **27**(4): 215-216.
- Xing, Y. (2012). Development of Thin Film Oxygen Transport Membranes on Metallic Supports. PhD, Ruhr University Bochum.
- Xue, J., Q. Liao, Y. Wei, Z. Li and H. Wang (2013). "A CO<sub>2</sub>-tolerance oxygen permeable 60Ce<sub>0.9</sub>Gd<sub>0.1</sub>O<sub>2-δ</sub>-40Ba<sub>0.5</sub>Sr<sub>0.5</sub>Co<sub>0.8</sub>Fe<sub>0.2</sub>O<sub>3-δ</sub> dual phase membrane." Journal of Membrane Science **443**(0): 124-130.
- Yin, X., L. Hong and Z.-L. Liu (2006). "Oxygen permeation through the LSCO-80/CeO<sub>2</sub> asymmetric tubular membrane reactor." Journal of Membrane Science **268**(1): 2-12.
- Zhu, X., M. Li, H. Liu, T. Zhang, Y. Cong and W. Yang (2012). "Design and experimental investigation of oxide ceramic dual-phase membranes." Journal of Membrane Science **394-395**(0): 120-130.
- Zhu, X., H. Liu, Y. Cong and W. Yang (2012). "Novel dual-phase membranes for CO<sub>2</sub> capture via an oxyfuel route." Chemical Communications **48**(2): 251-253.
- Zhu, X., H. Liu, Q. Li, Y. Cong and W. Yang (2011). "Unsteady-state permeation and surface exchange of dual-phase membranes." Solid State Ionics **185**(1): 27-31.
- Zhu, X., H. Wang and W. Yang (2008). "Relationship between homogeneity and oxygen permeability of composite membranes." Journal of Membrane Science **309**(1-2): 120-127.

## 7. Figures & Tables

Figure 1 Schematic diagram of the oxyfuel combustion process in a power plant. ....	1
Figure 2 Oxygen ion transport through a dense ion-electronic conducting membrane. ....	5
Figure 3 Resistance model of asymmetric membrane and its distributed concentration profile(Niehoff '14).....	6
Figure 4 Thickness dependence of the permeance of BSCF membranes is plotted along with fitted line of the calculated flux using Wagner's equation for the corresponding membrane thicknesses. The calculated value of $L_c$ using the modified Wagner's equation is marked to indicate the predicted transition of oxygen transport limitation (Baumann '15). ....	8
Figure 5 Schematic diagram of ions and electrons transport via Triple Phase Boundary (TPB) ...	9
Figure 6 Cross section of a membrane assembly comprising of porous support, dense membrane layer, and porous surface activation layer.....	10
Figure 7 Perovskite crystal structure where red sphere represent the A-cation, green spheres represent the B-cations and small blue spheres are oxygen ions. Reprinted from (Skinner '03) with permission of Elseviers.....	12
Figure 8 Schematic picture of oxygen ionic/pure electronic conductor dual-phase membrane (left) and oxygen ionic/mixed conductor dual-phase membrane (right). Reproduced from (Dong '11) with permission of The Royal Society of Chemistry.....	13
Figure 9 Fluorite type Crystal Structure. Reprinted from (Skinner '03) with permission of Elseviers.....	14
Figure 10 Ionic conductivity of several anionic conductors as a function of inverse temperature. Reprinted from (Vernoux '13) with permission of American Chemical Society.....	15
Figure 11 Spinel crystal structure ( $AB_2O_4$ ) (Reprinted from Defects in Crystals © Prof. Dr. Helmut Föll, University of Kiel, (tf.uni-kiel.de)) .....	16
$K_2NiF_4$ Materials .....	17
Figure 12 Representation of $A_2BO_{4+\delta}$ structure, where the red spheres represent B-cations, the blue spheres represent oxygen ions, and the yellow spheres represent A-cations. An interstitial oxygen ion is also shown. Reprinted from (Skinner '03) with permission of Elseviers. ....	18
Figure 13 Ionic and electronic conductivity of several materials for the temperature range of 900-1000 °C are plotted (Schróder '08). ....	19

Table 1 Literature summary of the dual phase membranes and their oxygen permeation values corresponding to limiting process parameters .....	20
Table 2 Nitrates of individual compounds mixed with citric acid and ethylene glycol to obtain 50 g of $Ce_{0.8}Gd_{0.2}O_{2-\delta}$ - $FeCo_2O_4$ (CGO-FCO) composite in 60:40 wt% proportion by Pechini process.....	21
Figure 14 Flow chart of powder synthesis by Pechini process.....	22
Figure 15 Flow chart of spray drying process (Kountouros '95). .....	23
Figure 16 The schematic of a typical tape casting process.....	26
Table 3 Optimized recipe for 100 g of CGO-FCO powder into tape casting slurry for both membrane and support layers. ....	27
Figure 17 Flow chart of step by step procedure to make the tape casting slurry for CGO-FCO membrane and porous support. ....	28
Figure 18 Scheme of the diffraction geometry on a crystalline material (ChemUCDavisWeblink , Uni_GottingenPhysikWeblink).....	31
Figure 19 Four point configuration for DC conductivity measurements (Ramírez '13).....	35
Figure 20 A schematic of a 4-End mode permeation set up .....	37
Figure 21 Quartz experimental setup and its schematic 4-end mode permeation measurement. .	38
Figure 22 The 4-End mode steel permeation setup (left), CGO-FCO sintered pellet soldered to Crofer 22 APU gasket using AgTiCu based alloy, heat treated at 900°C, SEM image of the cross section (right).....	38
Figure 23 A sketch of the permeation measurement set up. PG – Pressure gauge, MFC – Mass flow controllers, OA – Oxygen analyzer .....	39
Table 4 Dual Phase membranes with 60 wt % ionic conducting phase and 40 wt % electronic conducting phase were pechini synthesized and investigated. ....	41
Figure 24 XRD plots of the sintered dual phase pellets CGO-FCO, CGO-MCO, CGPO-FCO and CGPO-MCO (the compounds are mixed in 60 wt% fluorite to 40 wt% spinel proportion). .....	42
Table 5 Crystallographic phases identified by XRD analysis of the sintered dual phase pellets (mixed in 60 wt% fluorite to 40 wt% spinel proportion). Green and purple box indicate presence of peaks matching additional phases.....	43
Figure 25 XRD plots of CGO-FCO and CGO-MCO sintered pellets. Green box – orthorhombic perovskite peaks and purple box – rock salt phase observed in CGO-FCO.....	43

## 7 Figures & Tables

Figure 26 SEM images of the four dual phase composites mixed in 60 wt% fluorite to 40 wt% spinel proportion after sintering at 1200°C for 10 h. Phase 1 – CGO, Phase 2 – (Fe, Mn) Co, Phase 3 – Perovskite. ....	44
Figure 27 Permeation test of CGO-FCO, CGO-MCO, CGPO-FCO and CGPO-MCO dual phase pellets (mixed in 60 wt% CGO to 40 wt% spinel proportion) compared to LSCF for reference. ....	45
Figure 28 The Fe–Co oxide phase diagram in air at 1000–2100 K. $x$ is 2 in $\text{Co}_x\text{Fe}_{3-x}\text{O}_{4\pm\delta}$ for the dual phase compound of our interest (Hansson '05). ....	46
Figure 29 60 wt% CGO - 40 wt% CoO sample a) Sintered @1200 °C with cooling rate 3 K/min, b) Sintered @1200 °C with cooling rate 0.5 K/min, c) Powder calcined @1000 °C in Ar and sintered @1200 °C 1h in Ar.....	46
Figure 30 XRD plot of 60 wt% CGO-40 wt% FCrO composite as powder, sintered in air and argon at 1200 °C. Green region – unintended perovskite phase peaks and purple region – spinel peaks disappear. ....	48
Figure 31 XRD plot of 60 wt% CGO – 40 wt% STF as powder and sintered (1400 °C for 5 h) pellet with the intended phases. ....	49
Figure 32 SEM image of 60 wt% CGO – 40 wt% STF pressed pellet sintered at 1400 °C for 5 h. Left – Varying grain size of phases, Right – inhomogenous distribution of phases. ....	49
Figure 33 oxygen flux of 60 wt% CGO – 40 wt% STF compared to 60 wt% CGO – 40 wt% FCO, single phase STF and LSCF.....	50
Figure 34 Permeability plot of STF and 60 wt% CGO – 40 wt% STF along with their enhancement factor.....	51
Table 6 XRD analysis of Pechini processed 60 wt% CGO with 40 wt% LNC dual phase compound as powder .....	52
Table 7 XRD analysis of Pechini processed 60 wt% CGO with 40 wt% LNO dual phase compound as powder .....	52
Figure 35 SEM images of 60 wt% CGO with 40 wt% LNO sample sintered at 1400 °C. Side a – Leached 2 <sup>nd</sup> phase (grey), side b – 2 <sup>nd</sup> phase (grey) visible.....	53
Figure 36 XRD plot of 60 wt% CGO with 40 wt% LNO sintering study. NiO (green shaded region) formed around temperature $\geq 1300$ °C, LNO peaks (purple shaded region) only visible in powder, 1250 °C to 1350 °C.....	54

Table 8 Crystallographic phases identified by XRD analysis of 60 wt% CGO with 40 wt% LNO sintering study samples .....	54
Figure 37 Permeation test of 60 wt% CGO with 40 wt% LNO sintered at 1400 °C.....	55
Figure 38 XRD plot of 60 wt% CGO – 40 wt% FCO as powder, sintered at 1200 °C for 10 h, annealing sintered sample at 850 °C for 100 h (marked as 2S-850 °C) and sintering at 1200 °C for 10 h with additional slow cooling from 900 °C to 800 °C (marked as SC).....	56
Figure 39 Varying lattice parameter of spinel structure as a function of Fe incorporated into Co <sub>3</sub> O <sub>4</sub> (Bahlawane '09). Lattice parameter 8.3 Å and 8.15 Å are marked to identify Co dopant concentration.....	57
Table 9 Quantification of the phases formed in 60 wt% CGO – 40 wt% FCO composite after sintering using Rietveld analysis. ....	57
Figure 40 SEM image of 60 wt% CGO – 40 wt% FCO marked with Phase 1 –Fluorite, Phase 2 – Perovskite and Phase 3 – Spinel. ....	58
Figure 41 SEM image with elemental mapping of the compounds present in 60 wt% CGO – 40 wt% FCO composite.....	58
Figure 42 STEM–HAADF image of the 60 wt% CGO – 40 wt% FCO sample showing the presence of additional phases (left). Higher magnification image of the boundary phase present in FCO grain (right) .....	59
Figure 43 Characteristic EELS spectra recorded from the grains in 60 wt% CGO – 40 wt% FCO sample .....	60
Figure 44 STEM-HAADF image, EDS element mapping and semi-quantitative results of 60 wt% CGO – 40 wt% FCO sintered sample annealed at 850 °C for 100 h in air. ....	61
Figure 45 DTA/TG analysis of 60 wt% CGO – 40 wt% FCO powder subjected to sintering cycle at 3 K/min upto 1200 °C and back in air. ....	62
Figure 46 STEM-HAADF image of a CGO substrate PLD coated with FCO layer (100 nm) as deposited and tungsten coated on top during FIB lamellar sample preparation for STEM analysis (left). Annealing experiments with varying temperature and dwell time (right) .....	63
Figure 47 Diffraction pattern measured on thin film samples after annealing at (a) 1100 °C 1 h (b) 1050 °C 3 h and (c) 1000 °C 15 h. The vertical lines indicate literature pattern from PDF database: CGO (red), FeCo <sub>2</sub> O <sub>4</sub> (blue), Gd(Fe,Co)O <sub>3</sub> (pink) .....	64

## 7 Figures & Tables

Figure 48 (a) EDS net count mapping of the 1000 °C 3 h (b) EDS mapping of enlarged image of yellow box area marked in HAADF image in (a).....	65
Figure 49 SIMS plot of as deposited (left) and 1050 °C 6 h annealed (right) samples. ....	66
Figure 50 Electrical conductivity of individual phases and dual phase composite 60 wt% CGO - 40 wt% FCO . ....	67
Figure 51 Arrhenius plot as a function of permeance and temperature of the composite with and without porous LSCF coating.....	70
Table 10 CGO-FCO composite ratios investigated, in wt% and vol% for comparison .....	71
Figure 52 XRD plot of the composites with varying spinel content from 40 wt% to 10 wt% sintered at 1200 °C for 10 h.....	72
Figure 53 SEM images of CGO-FCO composites with ratios (in wt%) 60:40 (top left), 70:30 (top right), 80:20 (bottom left) and 90:10 (bottom right). Phase 1 – CGO, Phase 2 – FCO, Phase 3 – GCFCO. ....	73
Figure 54 STEM-HAADF and EDS element mapping of CGO-FCO 90:10 ratio (in wt%) composite sintered at 1200 °C for 10 h.....	73
Figure 55 (a) Electrical conductivity of CGO-FCO composite with varying spinel content from 35 wt% to 10 wt%, (b) Electrical conductivity of individual phases and dual phase composite 60 wt% CGO - 40 wt% FCO. ....	74
Figure 56 Plot as a function of Permeance for varying spinel content and their corresponding calculated activation energy between 800-1000 °C.....	75
Figure 57 Surface images by SEM investigation of 60:40 and 70:30 ratio (in wt%) CGO-FCO composites post permeation measurement at temperature range 700 - 1000 °C with air/Ar gradient. ....	77
Figure 58 SEM image of the cross section on the feed side of 60 wt% CGO – 40 wt% FCO membrane post permeation measurement at temperature range 700 - 1000 °C with air/Ar gradient. ....	77
Figure 59 Surface images by SEM investigation of 80:20 and 85:15 ratio CGO-FCO composites post permeation measurement at temperature range 700 - 1000 °C with air/Ar gradient. ....	78
Figure 60 SEM images of CGO-FCO 60:40 composite before ( reference) and after exposure to 1) Pure CO <sub>2</sub> 2) 250 ppm of SO <sub>2</sub> in CO <sub>2</sub> 3) 250 ppm SO <sub>2</sub> + 5 vol% O <sub>2</sub> in CO <sub>2</sub> and 4) 250 ppm SO <sub>2</sub> + 5 vol% O <sub>2</sub> + 2.5 vol% H <sub>2</sub> O (saturated at room temperature) in CO <sub>2</sub> .....	80

Figure 61 SEM images of 60 wt% CGO – 40 wt% FCO composite both sides of the membrane after exposure 250 ppm of SO <sub>2</sub> in CO <sub>2</sub> + 5% O <sub>2</sub> + 2.5% H <sub>2</sub> O at 850 °C for 16 h .....	81
Figure 62 EDX mapping of 60 wt% CGO – 40 wt% FCO composite after exposure 250 ppm of SO <sub>2</sub> in CO <sub>2</sub> + 5% O <sub>2</sub> + 2.5% H <sub>2</sub> O at 850 °C for 16 h.....	82
Figure 63 SEM image of 85 wt% CGO – 15 wt% FCO composite after exposure at 850 °C for 16 h 1) Pure CO <sub>2</sub> 2) 250 ppm of SO <sub>2</sub> in CO <sub>2</sub> 3) 250 ppm SO <sub>2</sub> + 5 vol% O <sub>2</sub> in CO <sub>2</sub> and 4) 250 ppm SO <sub>2</sub> + 5 vol% O <sub>2</sub> + 2.5 vol% H <sub>2</sub> O (saturated at room temperature) in CO <sub>2</sub> . Flakes marked in red circles .....	83
Figure 64 Oxygen flux of the 85 wt% CGO – 15 wt% FCO with LSCF active layer. Atm. Pressure plot is measurement from IEK-1 setup at 1 bar, 2.5 and 5 bar plots are measured at ORNL. Blue dotted circle denote change of feed gas to air+ 250 ppm SO <sub>2</sub> +CO <sub>2</sub> +5%O <sub>2</sub> for 5 h.85	
Table 11 Overview of the different powder processing methods with pros and cons of each method listed .....	87
Table 12 PSD and Specific surface area of powders by different synthesis route .....	87
Figure 65 SEM images of SP (spray pyrolysis) synthesized powder. ....	88
Figure 66 XRD scan of CGO-FCO 85:15 samples sintered at 1200 °C for 10 h. powders were synthesized by Pechini, SSR and SP route as marked. ....	88
Figure 67 SEM images of the cross sectioned sample, sintered at 1200 °C for 10 h, made from a)Pechini powder, b) “mixed powder (SSR)” and c) Spray pyrolysis (SP). (some pores are marked in red circles to distinguish from spinel phase) .....	89
Figure 68 Oxygen flux (left) and Arrhenius plot of the oxygen permeability (right) through 1 mm CGO-FCO 85:15 membranes activated on both sides by porous LSCF layer, under air/argon gradient. ....	90
Figure 69 SEM images of pre-pressed 60 wt% CGO – 40 wt% FCO sample after hot pressing at 50 MPa, 1200 °C for 1 h in argon. ....	92
Figure 70 Pre-sintered 60 wt% CGO – 40 wt% FCO pellet hot pressed at 50 MPa, 1200 °C for 1 h in Ar atmosphere a) polished to remove b) the graphite residue that had attached to the pellet. ....	92
Figure 71 XRD plot of 60 wt% CGO – 40 wt% FCO pre-pressed and pre-sintered (950 °C for 20 h) pellets, subjected to hot pressing at 50 MPa, 1200 °C for 1 h in argon atmosphere using	

## 7 Figures & Tables

graphite die are compared to conventional sintered sample. Samples differentiated by marking PS for pre-sintered and HP for hot pressing.....	93
Figure 72 SEM images of 60 wt% CGO – 40 wt% FCO pre-sintered pellet after hot pressing at 50 MPa, 1200 °C for 1 h in Ar atmosphere. ....	94
Figure 73 XRD plots of 60 wt% CGO – 40 wt% FCO hot pressed samples post annealed in air at 1000°C for 5 h. Samples differentiated by marking PS for pre-sintered and HP for hot pressing. ....	94
Figure 74 60 wt% CGO – 40 wt% FCO hot pressed at 50 MPa, 1200 °C for 1 h using Al <sub>2</sub> O <sub>3</sub> die in argon atmosphere .....	95
Figure 75 XRD plot of 60 wt% CGO – 40 wt% FCO pre-pressed pellet hot pressed at 50 MPa, 1200 °C for 1 h using Al <sub>2</sub> O <sub>3</sub> die in argon atmosphere. ....	96
Figure 76 SEM images of 60 wt% CGO – 40 wt% FCO pre-pressed pellet hot pressed at 50 MPa, 1200 °C for 1 h using Al <sub>2</sub> O <sub>3</sub> die in argon atmosphere. Phase 1 – CGO, Phase 2 – FCO and Phase 3 – GCFCO.....	96
Figure 77 XRD plot of 60 wt% CGO – 40 wt% FCO conventionally sintered (CS) at 1200 °C, SPS/FAST sintered at 900 °C (SPS) and SPS/FAST sintered sample annealed (A) at 1000 °C..	98
Table 13 Alternative sintering techniques and their outcomes.....	99
Table 14 Slurry development for tape casting of a dual phase membrane starting from CGO-FCO 85:15 powders prepared via pechini route. ....	101
Figure 78 Defects observed in CGO-FCO 85:15 Membrane layer produced with pechini synthesized powder. a) Pin holes and Cracks after sintering b) Crack propagation of green tape in contact with solvent .....	101
Table 15 Slurry development for tape casting of support starting from CGO +CoO powders. Corn starch (CS), graphite (GR) and rice starch (RS) .....	103
Figure 79 Defects observed in CGO -2 mol% CoO Support layer such as boating, crowfoot cracks and sintering cracks .....	104
Table 16 slurry prepared for tape casting of support layer from CGO-FCO 85:15 SSR powder. ....	104
Table 17 list of membrane / support tape cast combinations subjected to microstructure investigation.....	105
Figure 80 Tape cast asymmetric CGO-FCO 85:15 (Pechini) membrane with porous CGO-FCO 85:15 (SSR) support sintered at 1200 °C for 5 h. ....	105

Figure 81 Tape cast asymmetric CGO-FCO 85:15 (Pechini) membrane with porous 2 mol% CoO-CGO support sintered at 1200 °C for 5 h.....	106
Figure 82 Tape cast asymmetric CGO-FCO 85:15 (SSR) membrane with porous CGO-FCO 85:15 (SSR) support sintered at 1200 °C for 5 h. ....	106
Figure 83 Tape cast asymmetric CGO-FCO 85:15 (SSR) membrane with porous 2 mol% CoO-CGO support sintered at 1200 °C for 5 h.....	106
Table 18 Microstructural parameters of the asymmetric membranes manufactured by sequential tape casting, determined by quantitative image analysis. ....	107
Figure 84 EDX analysis of CGO-FCO 85:15 (Pechini) membrane / 2 mol% CoO-CGO support interface of the tape cast membrane sintered at 1200 °C for 5 h. ....	108
Figure 85 Comparison of oxygen flux (left) and permeability (right) between 1mm bulk membrane (2 sides activated) and the asymmetric membrane (1 side activated). Both membranes were made from CGO-FCO 85:15 SSR powder sintered at 1200 °C for 5 h. ....	109
Figure 86 DTA/TG of membrane, support and membrane+support layers combined subjected to sintering cycle at 3 K/min upto 1200 °C in air. powders made from CGO-FCO 85:15 SSR route for both membrane and support layers.....	110
Figure 87 Heat treatment profile for porous asymmetric membrane by tape casting, sintered at 1200°C. powders made from CGO-FCO 85:15 SSR route for both membrane and support layers. ....	111

## 8. Acknowledgements

I take immense pleasure in acknowledging all the people who made this PhD thesis possible and have been very supportive in the last three years.

I would like to start with thanking Dr. Buchkremer for providing me with the opportunity to pursue my PhD research in IEK-1 and current head of the Institute Prof. Olivier Guillon for continuing the support and motivation during the course of my research work.

My PhD would not have been possible without Willi Meulenberg, for believing in my credentials and giving me the opportunity to pursue my doctoral studies at Forschungszentrum Jülich GmbH. He has been my go to person in the last three years for any guidance and help needed for a comfortable work place.

I am very thankful to Stefan Baumann for being the best advisor and mentor throughout my PhD research work. He made himself available regardless of the time for many useful discussions both professional and outside of work. His deep understanding of the subject was a great motivation for me.

I have to thank Robert Vaßen, head of ORNL collaborative project. His inquisitiveness during project meetings has been very helpful for fundamental understanding of relative concepts.

My acknowledgements would be incomplete without thanking my colleagues in the Membrane group: Maria Balaguer, Falk Schulze-Koppers, Patrick Niehoff, Mariya Ivanova, Wendelin Deibert. Each and every one of them were more than willing to help when needed and their friendliness made me feel at ease from the very beginning.

I would like to express my gratitude to Ramesh Bhawe, Daejin Kim and Larry Powell of ORNL for their invitation, research facility and continuous support to carry out part of my PhD work. It was a great experience to perform research work at a another reputed research organization in USA.

During the course of the PhD, some valuable characterizations by Doris Sebold (SEM), Yoo Jung Sohn (XRD), Volker Nischwitz (ICP-OES) and Uwe Breuer (ToF-SIMS) of ZEA-3, Riza

Iskandar and Justinas Palisaitis (STEM) of ER-C were very helpful for deeper understanding of the materials researched.

I also would like to thank Stefan Heinz for the lab assistance and permeation measurements, Michaela Andreas for raw materials access and Volker Bader, for all the thermal treatments, Marie-Theres Gerhards and Sylke Pristat for the thermal analysis, Qianli Ma for electrical conductivity measurements, Mark Kappertz for sample preparation assistance, Sigrid Schwartz-Lückge and Andrea Hilgers for particle morphology measurements.

I am very glad to have made some great friends Maria, Vanessa, Anna, Marie, Georg, Jan, Jesus and many more at IEK-1 during this PhD journey who made me feel welcomed and at home for the past three years.

None of this would have been possible without the love and encouragement of my family and friends who stand by me no matter what i choose to pursue in life both professionally and personally.

Finally, I would like to acknowledge the funding for this PhD thesis by German Federal Ministry of Education and Research (BMBF) for a bilateral collaborative research project with ORNL and the European Commission via the FP7 project GREEN-CC (Grant Agreement no. 608524).

# Curriculum Vitae

## Personal Information

Name: Madhumidha Ramasamy

Date of Birth: 01-01-1986

Place of Birth: Tiruppur

Nationality: Indian

**Education**            **PhD Candidate**, Mechanical Engineering, **Ruhr University Bochum**,  
Dissertation: "Dual Phase Oxygen Transport Membrane for Efficient  
Oxyfuel Combustion"  
**IEK-1, Forschungszentrum Jülich GmbH**  
*September 2013 - present*

**M. Sc.** Materials Engineering, **Auburn University USA**,  
*May 2008 - Dec 2010*

**B. Tech.** Ceramic Technology, **Anna University India**,  
*July 2003 - May 2007*

**Industrial**            **Firing process Engineer, Corning Inc.**,  
**Experience**            Corning, NY, USA, *2011-2013*

**Development Engineer, Atumin Energy Inc.**,  
Sunnyvale, CA, USA, *2011*

Band / Volume 338

**Influence of Thermomechanical Treatment on High Temperature Properties of Laves Phase Strengthened Ferritic Steels**

M. Talík (2016), xxiii, 130 pp

ISBN: 978-3-95806-175-0

Band / Volume 339

**Groundwater recharge in Slovenia**

**Results of a bilateral German-Slovenian Research project**

Mišo Andjelov, Zlatko Mikulič, Björn Tetzlaff, Jože Uhan & Frank Wendland (2016)

ISBN: 978-3-95806-177-4

Band / Volume 340

**Atomic oxygen derived from SCIAMACHY O(<sup>1</sup>S) and OH airglow measurements in the Mesopause region**

Y. Zhu (2016), 206 pp

ISBN: 978-3-95806-178-1

Band / Volume 341

**Diagnostic Mirror Concept Development for Use in the Complex Environment of a Fusion Reactor**

A. Krimmer (2016), x, 123 pp

ISBN: 978-3-95806-180-4

Band / Volume 342

**Long-Term Measurements of the Radiation Exposure of the Inhabitants of Radioactively Contaminated Regions of Belarus – The Korma Report II (1998 – 2015)**

P. Zoriy, H. Dederichs, J. Pillath, B. Heuel-Fabianek, P. Hill, R. Lennartz (2016), ca 105 pp

ISBN: 978-3-95806-181-1

Band / Volume 343

**Entwicklung und Charakterisierung von Nickel/Gadolinium-Ceroxid-basierten Anoden für die metallgestützte Festoxid-Brennstoffzelle**

V. Rojek-Wöckner (2016), XVI, 136 pp

ISBN: 978-3-95806-182-8

Band / Volume 344

**Reaction-diffusion modelling of hydrogen retention and release mechanisms in beryllium**

M. Wensing (2016), 100 pp

ISBN: 978-3-95806-184-2

Band / Volume 345

**Light Management by Intermediate Reflectors  
in Silicon-based Tandem Solar Cells**

A. Hoffmann (2016), 199 pp

ISBN: 978-3-95806-186-6

Band / Volume 346

**Design eines hocheffizienten Festoxid-Brennstoffzellensystems  
mit integrierter Schutzgaserzeugung**

M. Engelbracht (2016), 190 pp

ISBN: 978-3-95806-189-7

Band / Volume 347

**On model and measurement uncertainty in  
predicting land surface carbon fluxes**

H. Post (2016), xviii, 135 pp

ISBN: 978-3-95806-190-3

Band / Volume 348

**Bipolarplattenmaterialien für Polymer-Elektrolyt-Membran Elektrolyse**

M. Langemann (2016), I-III, 189, IV-XVIII pp

ISBN: 978-3-95806-192-7

Band / Volume 349

**Modellbasierte Ansteuerung räumlich ausgedehnter Aktuator-  
und Sensornetzwerke in der Strömungsregelung**

M. Dück (2016), XIII, 153 pp

ISBN: 978-3-95806-193-4

Band / Volume 350

**TRENDS 2015 – Transition to Renewable Energy Devices and Systems**

ed. by D. Stolten and R. Peters (2016), 200 pp

ISBN: 978-3-95806-195-8

Band / Volume 351

**Dual Phase Oxygen Transport Membrane  
for Efficient Oxyfuel Combustion**

M. Ramasamy (2016), VIII, 136 pp

ISBN: 978-3-95806-196-5

Weitere **Schriften des Verlags im Forschungszentrum Jülich** unter  
<http://www.zb1.fz-juelich.de/verlagextern1/index.asp>



